NAIST-IS-DD1361022

Doctoral Dissertation

Channel Estimation and Detection Schemes for ESPAR Antenna-Based OFDM Receivers

Diego Javier Reinoso Chisaguano

March 3, 2016

Department of Information Science
Graduate School of Information Science
Nara Institute of Science and Technology

A Doctoral Dissertation
submitted to Graduate School of Information Science,
Nara Institute of Science and Technology
in partial fulfillment of the requirements for the degree of
Doctor of ENGINEERING

Diego Javier Reinoso Chisaguano

Thesis Committee:

Professor Minoru Okada	(Supervisor)
Professor Kenji Sugimoto	(Co-supervisor)
Associate Professor Takeshi Higashino	(Co-supervisor)
Assistant Professor Yafei Hou	(Co-supervisor)

Channel Estimation and Detection Schemes for ESPAR Antenna-Based OFDM Receivers*

Diego Javier Reinoso Chisaguano

Abstract

Nowadays, wireless communications have become an essential part of our lives. Billions of electronic devices such as smartphones, cell phones, televisions, laptops, tablets, and even cars use wireless communication standards to access Internet, connect to other devices, or receive information. Most of the latest standards of wireless communications use orthogonal frequency-division multiplexing (OFDM) due to its high spectral efficiency and robustness to frequency-selective fading channels. In wireless links, the multipath fading of the transmitted signal can severely degrade the bit error rate (BER) in the receiver. Antenna diversity is a technique commonly utilized to counteract the effect of multipath fading; however, it has several limitations due to the additional radio frequency (RF) chains that it requires. To overcome this problem, an OFDM receiver using an electronically steerable passive array radiator (ESPAR) antenna was previously proposed to improve the BER without requiring additional RF chains. The ESPAR antenna-based receiver improves the BER but it requires special channel estimation and detection schemes. This dissertation presents low-complexity channel estimation and detection schemes for ESPAR antenna-based receivers that are designed for the Wireless Local Area Network (WLAN) IEEE 802.11n and digital television (DTV) Integrated Services Digital Broadcasting-Terrestrial (ISDB-T) standards.

In the first part of this study, the channel estimation and detection schemes for a multiple input multiple output - orthogonal frequency-division multiplexing

*Doctoral Dissertation, Department of Information Science, Graduate School of Information Science, Nara Institute of Science and Technology, NAIST-IS-DD1361022, March 3, 2016.

(MIMO-OFDM) receiver using a 3-element ESPAR antenna are proposed. This diversity receiver, which has only two RF chains in the receiver side, obtains a BER close to a conventional 2×4 MIMO-OFDM system that has four RF chains. For channel estimation, minimum mean square error (MMSE) and compressed sensing (CS)-based estimators are derived. The CS-based channel estimation obtains the best BER performance and requires less computational complexity than the MMSE channel estimation. Additionally, a submatrix detection scheme is proposed to reduce the computational cost required by the detection. This detection scheme reduced the required computational cost by about 92% compared to the block detection approach.

In on-vehicle ISDB-T receivers, the received signal can be severely affected by multipath fading and the movement of the car. The usual solution to overcome these problems is to use an ISDB-T receiver with antenna diversity but the additional antennas and cabling are important drawbacks in terms of installation time and complexity. The second part of this study proposes ESPAR antenna-based ISDB-T receivers that require only one antenna; thus, its installation in a car can be simplified. For channel estimation, a CS-based estimator is used and it can obtain a good accuracy. Additionally, a submatrix scheme is proposed to reduce the computational cost of the detection. This scheme reduced the required computational cost by around 90% compared to block detection.

Keywords:

ESPAR antenna, OFDM, MIMO-OFDM, ISDB-T, Diversity, Compressed sensing

Contents

List of Figures

List of Tables

Chapter 1

Introduction

This chapter firstly presents the importance of orthogonal frequency-division multiplexing (OFDM) receivers, which is the motivation of this dissertation. Next, the two problems that this dissertation addresses are presented. Then, the contributions and required tasks are included. Finally, the dissertation layout of the rest of the chapters is presented.

1.1 Research Motivation

According to estimations of the International Telecommunication Union (ITU) [1], by the end of 2015 there are 3.2 billion Internet users around the world. At the same time, there are more than 7 billion mobile cellular subscriptions, which is a tenfold increase compared to the 738 million of subscriptions in 2000. The mobile broadband penetration is 47% in 2015, a value that increased 12 times in the last eight years. This rapid increase in the mobile broadband subscriptions has been in part due to the popularity of smartphones. Only in 2014, an estimate of more than 1 billion smartphones were sold. These devices have not only the capability to connect to a cellular network but also to a Wireless Local Area Network (WLAN). Several other devices such as laptops, tablets, book readers, game consoles, and even cars can also connect to a WLAN. It is very clear that the development of digital wireless communications is one of the basis of the new era of information and communications technologies.

The invention of the television (TV) in the first half of the 20th century revolutionized the entertainment, news, and advertising industries. In 2012, an estimate of more than 1.4 billion households, which represented around 80% of the total in the world, had a TV [2]. The evolution of the TV would not have been possible without the wireless broadcasting standards, which were the platform for transmitting the TV signals to every household. There have been several innovations in the TV sets, like going from monochromatic to color. The technology of the TV display also improved from the bulky cathode ray tube to the small and compact liquid crystal display (LCD). The broadcasting technology also evolved from analog to digital. In the last decade, several digital TV (DTV) broadcasting standards were developed and started operating around the world. The most important of these standards are: Digital Video Broadcasting-Terrestrial (DVB-T) [3], Advanced Television System Committee (ATSC) [4], Integrated Services Digital Broadcasting-Terrestrial (ISDB-T) [5], and Digital Terrestrial Multimedia Broadcasting (DTMB) [6]. Some of the advantages of these standards include less required bandwidth, support of high-definition TV channels, and electronic program guides. The ISDB-T standard was developed in Japan and has been used since 2003. While the analog TV broadcasting in Japan was stopped in 2011, other countries are just starting to switch from analog to digital TV.

Some recent standards of WLAN, cellular, and DTV communications have something in common - they use OFDM technology. This digital multicarrier modulation divides the channel into subchannels by using orthogonal subcarriers, which improves the spectral efficiency because it does not require guard bands between the subcarriers. It is robust against intersymbol interference (ISI) and multipath fading due to the guard interval that is inserted in front of the OFDM symbol. OFDM is used in the WLAN standards IEEE 802.11a [7], 802.11g [8], 802.11n [9], and 802.11ac [10]. It is also used in the 4G standard for cellular communications LTE [11], and in the DTV standards DVB-T, ISDB-T, and DTMB. Consequently, OFDM is a very important technology that is very widespread nowadays and most likely will be part of the future standards of wireless communications.

1.2 Overview of the Problem

In wireless communication systems, multipath fading is the result of the multipath propagation of the transmitted signal, and it can severely affect the quality and reliability of a wireless link. Antenna diversity is one of the most common technologies used to overcome the effects of multipath fading. An OFDM receiver with this diversity scheme is composed of multiple antennas which are spatially separated and each one is connected to a radio frequency (RF) chain. This RF chain is usually composed of an RF front-end, analog to digital converter, fast Fourier transform (FFT) block, and other electronic circuits. Therefore, antenna diversity has the limitations of increased hardware complexity, energy consumption, and receiver size.

An OFDM receiver using an electronically steerable passive array radiator (ESPAR) antenna was proposed in [12]. This receiver was able to obtain diversity and improved the bit error rate (BER) of the system using only one RF chain. An RF signal processing-based diversity scheme for multiple-input multiple-output - OFDM (MIMO-OFDM) was proposed in [13]. This scheme used a similar idea to the receiver proposed in [12], although a 2-element phased array was utilized instead of an ESPAR antenna. This scheme was able to obtain diversity gain and improved the BER in a MIMO-OFDM system, however the computational cost of the channel estimation and detection schemes was too high. Consequently, it was not suitable for practical implementation and this is the first problem that this dissertation will address.

On-vehicle ISDB-T receivers are commonly used in Japan to watch TV in a car. The received signal is affected by the multipath fading and the movement of the vehicle, thus the receiver performance can be severely degraded. The usual solution is to use an ISDB-T receiver with antenna diversity, but the additional antennas and cabling are important drawbacks in terms of installation time and complexity. Figure 1.1 explain this problem using a receiver with two antennas. They are installed on the roof of the car and each one is connected to the receiver using coaxial cable. Compared to a receiver that only uses one antenna, the additional antenna and cable increases the installation cost. This is a problem that can also be solved with an ESPAR antenna-based receiver. It is important

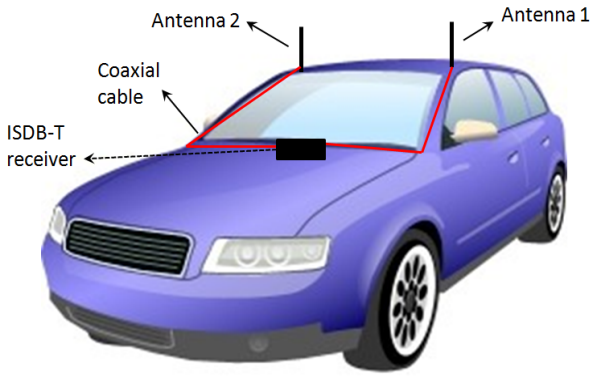

Figure 1.1: On-vehicle ISDB-T receiver with antenna diversity.

to note that special channel estimation and detection schemes are also required as part of this receiver to obtain an improvement in the BER.

1.3 Research Contribution

The first main contribution of this dissertation is the design of channel estimation and detection schemes for a MIMO-OFDM receiver with 3-element ESPAR antenna. This receiver obtains diversity gain and improves the BER of the system without increasing the number of RF chains, but requires a special channel estimator. In this dissertation, two different channel estimators are proposed for this purpose. Additionally, a low complexity detection scheme is proposed to reduce the required computational cost of the detection. Therefore, the main problems of the work presented in [13] are solved.

The other main contribution is the design of ESPAR antenna-based ISDB-T receivers. These receivers require only one ESPAR antenna and one cable so the installation of this receiver in a car can be simplified. An ISDB-T receiver with 3-element ESPAR antenna is designed and its performance is analyzed considering the ideal and real models of the antenna. An ISDB-T receiver with 4-element ESPAR antenna is also proposed. Additionally, compressed sensing-based channel estimation and low complexity detection schemes are designed for this receiver. The results show that this ISDB-T receiver obtains diversity gain and achieves an important improvement in the BER performance.

1.4 Research Tasks and Limitations

The first task is the theoretical design of the receivers and its components. This task includes the formulation of the signal model of each receiver, the design of the channel estimators, the formulation of the real model of the ESPAR antenna, and the design of the low complexity detection schemes. The second task is the implementation of simulation models for the designed receivers. These software simulations are utilized for evaluating the performance using different parameters such as the BER and required computational cost. For the real model of the ESPAR antenna, an electromagnetic software simulation is also performed to obtain the parameters of the antenna. This dissertation does not cover real experiments or hardware implementation of the receiver; hence, those can be considered as the limitations of this work.

1.5 Dissertation Layout

The rest of this dissertation is organized as follows. Chapter 2 presents a review of the related literature. A brief overview of ISDB-T, MIMO-OFDM, and antenna diversity technologies is included. Then, a review of some related works using ESPAR antenna and the theory of compressed sensing are also presented. In Chapter 3, the MIMO-OFDM receiver with 3-element ESPAR antenna is presented. It also includes the channel estimation and detection schemes designed for this receiver. Then, Chapter 4 introduces the ESPAR antenna-based ISDB-T receivers. The first part of this chapter presents an ISDB-T receiver with 3-element ESPAR antenna and shows its performance using the ideal and real models of the antenna. The second part of the chapter talks about the ISDB-T receiver with 4-element ESPAR antenna. Finally, Chapter 5 gives the conclusions and future works.

Chapter 2

Related Literature

In this chapter, first an overview of the ISDB-T and MIMO-OFDM systems, which are the main target of the work presented in this dissertation, is presented in Section 2.1. Then, a brief description of antenna diversity and ESPAR antenna is presented in Section 2.2 and 2.3, respectively. Two close related works are described in Section 2.4 and 2.5. Finally, the theory of compressed sensing and some recovery algorithms are introduced in Section 2.6.

2.1 Overview of ISDB-T and MIMO-OFDM Systems

2.1.1 ISDB-T

ISDB-T [5] is a DTV broadcasting standard that was developed in Japan and has been used since December 2003 for commercial DTV broadcasting. This standard has been also adopted in other Asian countries such as Philippines, Maldives, and Sri Lanka. A similar standard called ISDB-Tb has been adopted for DTV broadcasting in most of South and Central America countries. The basic difference between these two standards is the use of different video compression standards; while ISDB-T uses MPEG-2, ISDB-Tb uses MPEG-4. A map with the DTV standards used around the world is presented in Fig. 2.1.

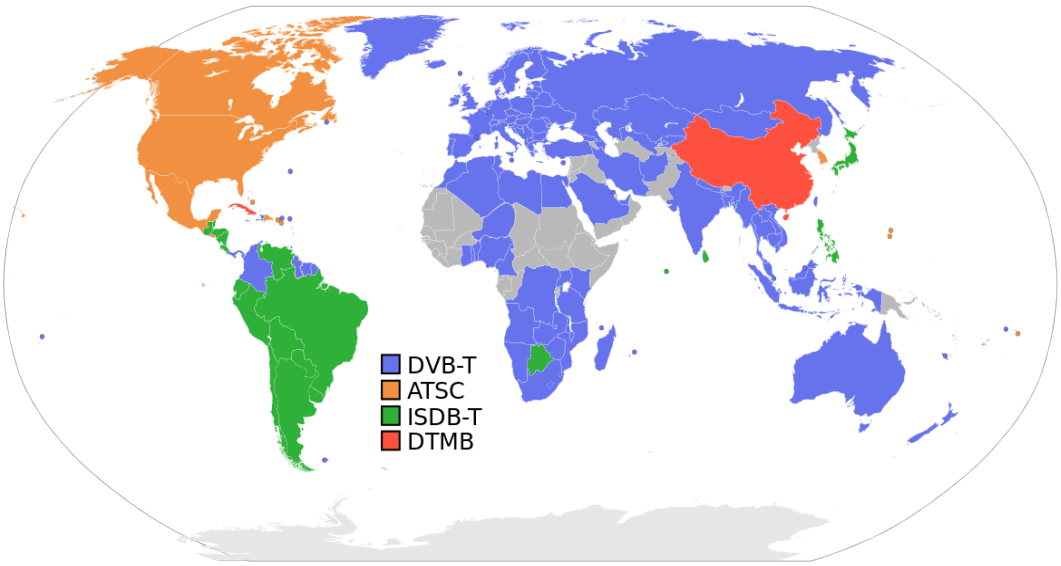

Figure 2.1: Digital TV standards used around the world [14].

The ISDB-T standard uses OFDM for digital multicarrier modulation. OFDM divides the channel into subchannels by using orthogonal subcarriers and this improves the spectral efficiency because it does not require guard bands between the subcarriers. The narrow bandwidth of the subcarriers makes it suitable for frequency-selective fading channels. It is also robust against ISI and multipath fading due to the guard interval that is inserted in front of the OFDM symbol [15].

Depending on the distance to the transmitting station and the required robustness to Doppler shift during mobile reception, ISDB-T offer three modes: mode 1, mode 2, and mode 3. The OFDM subcarrier spacing is approximately 4 kHz, 2 kHz, and 1 kHz for mode 1, 2, and 3, respectively. Mode 1 is robust for mobile reception but sensitive to multipath fading due to its small symbol length. On the other hand, mode 3 is robust against multipath fading but sensitive to the Doppler shift present in mobile reception. The number of total subcarriers, data subcarriers, FFT window size, and effective symbol length are also different among the three modes. Table 2.1 presents a summary of the parameters of the ISDB-T standard. These parameters are selected depending on the channel characteristics; thus, offering a great adaptability to different scenarios.

Table 2.1: Parameters of the ISDB-T standard

ISDBT-T mode	Mode 1	Mode 2	Mode 3
Number of OFDM segments	13		
Channel bandwidth	6 MHz		
Useful bandwidth	5.575 MHz	5.573 MHz	5.572 MHz
Subcarrier spacing	3.968 kHz	1.984 kHz	0.9992 kHz
Number of total subcarriers	1405	2809	5617
Number of data subcarriers	1248	2496	4992
Modulation method	DPSK, QPSK, 16QAM, 64QAM		
FFT window size	2048	4096	8192
Number of symbols per frame	204		
Effective symbol length	252 μs	504 μs	1008 μs
Guard interval length	1/4,1/8,1/16,1/32 of effective sym. length		
Inner code	Convolutional code (1/2, 2/3, 3/4, 5/6, 7/8)		
Outer code	Reed-Solomon (204,188)		
Data bit rate	3.65 - 23.23 Mbps		

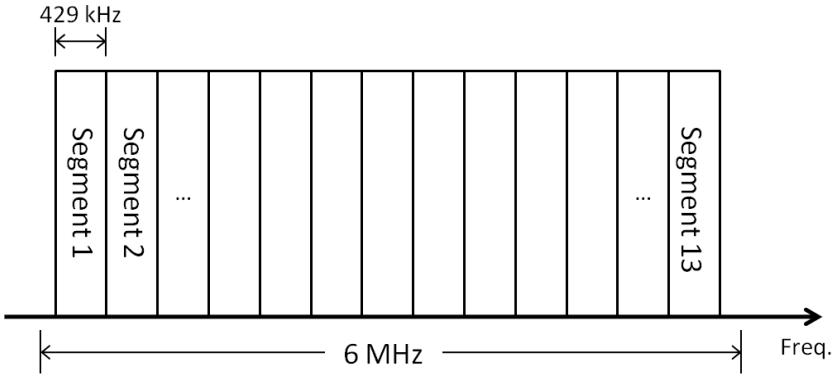

Figure 2.2: Division of the channel bandwidth into OFDM segments.

In ISDB-T, the channel is divided into 13 OFDM blocks that are called segments and are illustrated in Fig. 2.2. Each segment has a bandwidth of approximately 429 kHz. The number of subcarriers in each segment depends of the transmission mode, e.g., in mode 3 there are 432 subcarriers per segment. A hierarchical layer consists of one or more OFDM segments and each layer can have different coding rate, modulation scheme, and other parameters. These layers allow the use of the same channel for fixed and mobile reception without additional transmitting infrastructure.

An overview of the ISDB-T transmitter is presented in Fig. 2.3. It shows that video, sound, and data are multiplexed into one or more transport stream (TS), and then re-multiplexed into a single TS. Then, the TS is separated into parallel hierarchical layers and the channel coding is performed in each layer. Finally, the inverse fast Fourier transform (IFFT) block is used to obtain the OFDM signal that is transmitted.

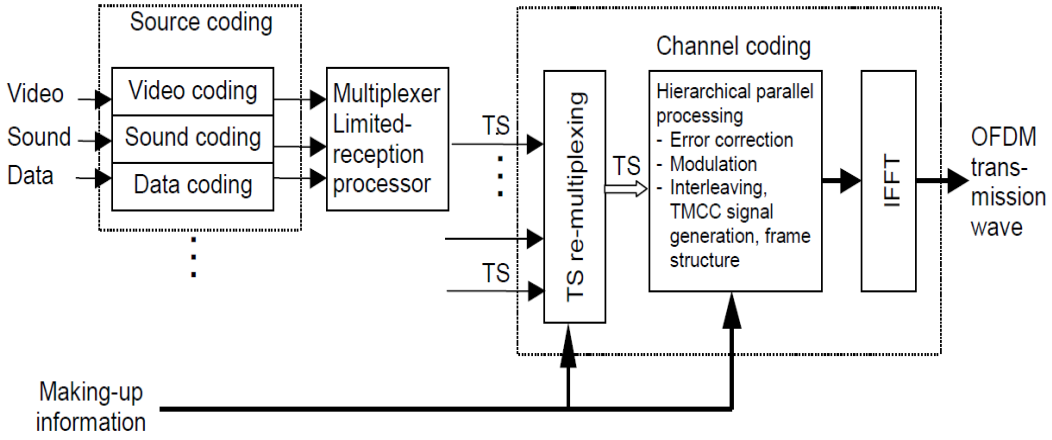

Figure 2.3: Overview of the ISDB-T transmitter [5].

The services that can be provided using ISDB-T are: standard-definition TV (SDTV), high-definition TV (HDTV), one-seg mobile reception for hand-held devices, interactive TV, and emergency warning broadcasting. Another advantage of ISDB-T is the capability of using a single frequency network, where all the repeaters can transmit using the same channel; thus, offering effective utilization of the frequency resource. It also requires lower transmitter power compared with analog TV; moreover, the reception is possible using an indoor antenna.

2.1.2 MIMO-OFDM

A MIMO system is composed of multiple transmit and receive antennas. It has the ability to turn multipath propagation, which is traditionally a pitfall of wireless transmission, into a benefit for the user [16]. MIMO offers increased spectral efficiency through spatial multiplexing gain and improved link reliability due to antenna diversity gain [17]. In multipath fading channels, it can achieve a great increase in the channel capacity [18].

Assuming a flat-fading channel, a MIMO system can be represented by the following discrete-time model [19]

$$\begin{pmatrix} y_1 \\ \vdots \\ y_{N_R} \end{pmatrix} = \begin{pmatrix} h_{11} & \dots & h_{1N_T} \\ \vdots & \ddots & \vdots \\ h_{N_R1} & \dots & h_{N_R,N_T} \end{pmatrix} \begin{pmatrix} x_1 \\ \vdots \\ x_{N_T} \end{pmatrix} + \begin{pmatrix} n_1 \\ \vdots \\ n_{N_R} \end{pmatrix}, \tag{2.1}$$

or simply as

$$\mathbf{y} = \mathbf{H}\mathbf{x} + \mathbf{n}, \tag{2.2}$$

where $\mathbf{y} = [y_1, \dots, y_{N_R}]^T$ is the vector of received symbols, $\mathbf{x} = [x_1, \dots, y_{N_T}]^T$ represents the vector of transmitted symbols, $\mathbf{n} = [n_1, \dots, n_{N_R}]^T$ is a vector of additive noise terms assumed independent and identically distributed (i.i.d.) complex Gaussian with each element having a variance of σ^2, and $\mathbf{H}$ is the $N_R \times N_T$ matrix of channel gains that is given by

$$\mathbf{H} = \begin{pmatrix} h_{11} & \dots & h_{1N_T} \\ \vdots & \ddots & \vdots \\ h_{N_R1} & \dots & h_{N_R,N_T} \end{pmatrix} \tag{2.3}$$

where h_{ik} represents the gain from the k-th transmit antenna to the i-th receive antenna.

OFDM is robust against frequency-selective fading, multipath fading, and ISI [20]. This technology can transform a frequency-selective fading channel into parallel flat-fading subchannels. The combination of MIMO and OFDM technologies is known as MIMO-OFDM [21]-[23]. The block diagram of a MIMO-OFDM transmitter is shown in Fig. 2.4. The MIMO-OFDM transmitter basically consists of N_T OFDM transmitters [23]. The input data is multiplexed into parallel data

streams and fed to every transmitter branch. Then, each branch performs: encoding, interleaving, quadrature amplitude modulation (QAM) mapping, inverse IFFT, and adds a cyclic prefix. The digital to analog converter (DAC) obtains the analog signal that is up-converted and amplified using the RF high power amplifier (HPA). Finally, the signals are fed to the transmitting antennas.

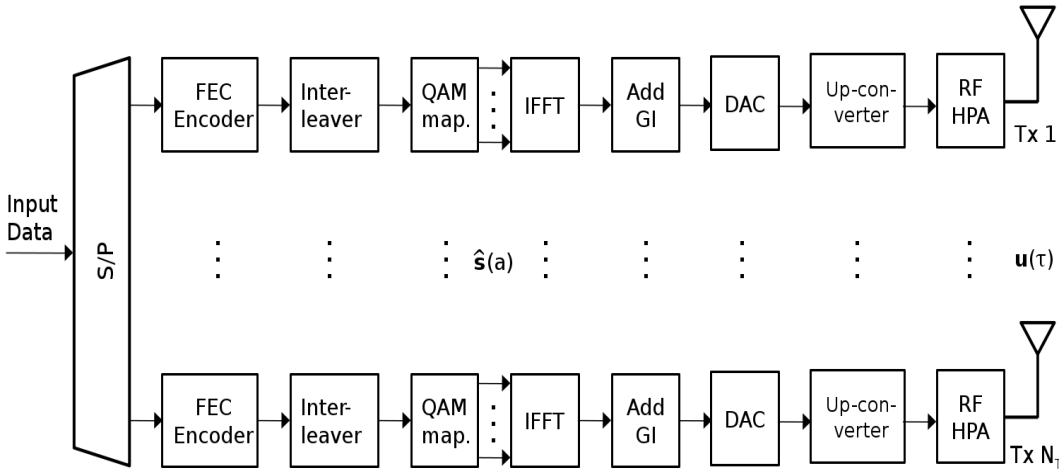

Figure 2.4: Block diagram of a MIMO-OFDM transmitter.

The block diagram of a MIMO-OFDM receiver is shown in Fig. 2.5. The signal received in each antenna is digitalized using the RF front-end, down-converter, and analog to digital converter (ADC). Then, the cyclic prefix is removed and the frequency domain signal is obtained using the FFT. Next, the MIMO detection is performed for each OFDM subcarrier [22] using the information provided by the channel estimator. After the subcarriers of every branch are detected, the signal is demapped, deinterleaved, and decoded.

Referring to [23], a MIMO-OFDM system with N_T transmit and N_R receive antennas in a frequency-selective fading channel is considered. Additionally, a quasistatic channel is assumed so the communication channel remains constant during a packet transmission. At a discrete time instance τ, the transmitter sends an N_T-size complex vector $\mathbf{u}(\tau) = [u_1(\tau), \ldots, u_{N_T}(\tau)]^T$ and receives an N_R-size complex vector $\mathbf{r}(\tau) = [r_1(\tau), \ldots, r_{N_R}(\tau)]^T$, where $u_i(\tau)$ and $r_k(\tau)$ are the transmitted and received signals at time τ in the i-th transmitter antenna element and k-th receiver antenna, respectively. Let $\mathbf{G}(l)$ be the channel impulse

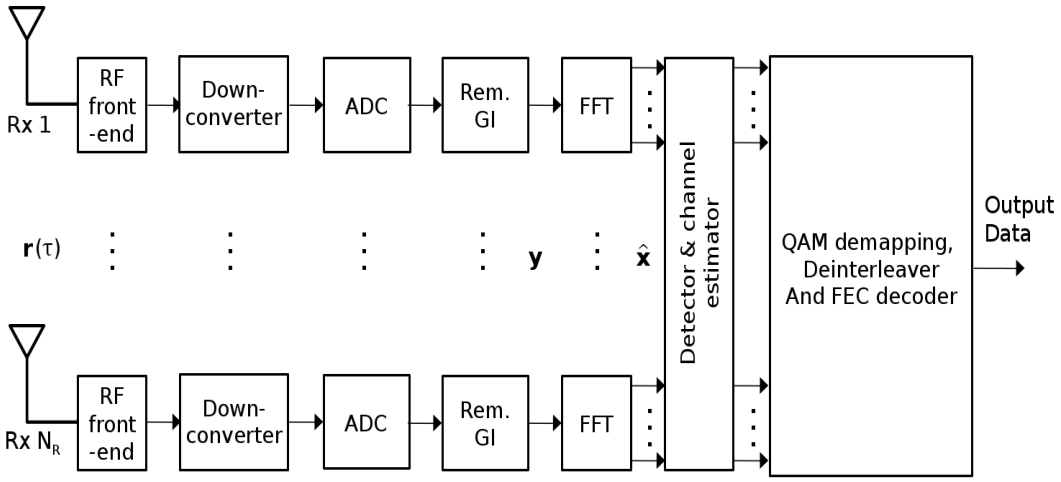

Figure 2.5: Block diagram of a MIMO-OFDM receiver.

response at delay interval l. The maximum delay has to be less than the guard interval size to avoid ISI. Assuming $g_{qp}(l)$ is the (q,p)-th element of the matrix $\mathbf{G}(l)$ with $l = 0, \ldots, L-1$, the discrete-time MIMO baseband signal model is given by

$$\mathbf{r}(\tau) = \sum_{l=0}^{L-1} \mathbf{G}(l)\mathbf{u}(\tau - l) + \mathbf{v}(\tau), \tag{2.4}$$

where $\mathbf{v}(\tau)$ represents additive white Gaussian noise (AWGN) at the τ-th sample with N_R i.i.d. zero-mean complex Gaussian elements with variance $(1/2)\sigma_v^2$ per dimension. The elements of $\mathbf{u}(\tau)$ are assumed zero-mean uncorrelated random variables with variance σ_u^2.

Considering that N_c subcarriers are transmitted in each antenna, the a-th received MIMO-OFDM symbol after removing the cyclic prefix of length N_g is given by

$$\hat{\mathbf{y}}(a) = \mathbf{C}\hat{\mathbf{u}}(a) + \hat{\mathbf{v}}(a), \qquad a = 0, 1, \ldots \tag{2.5}$$

where $\hat{\mathbf{u}}(a)$ and $\hat{\mathbf{v}}(a)$ are given by

$$\hat{\mathbf{u}}(a) = \begin{pmatrix} \mathbf{u}(aN_{tot} + N_g) \\ \vdots \\ \mathbf{u}(aN_{tot} + N_g + N_c - 1) \end{pmatrix}, \tag{2.6}$$

$$\hat{\mathbf{v}}(a) = \begin{pmatrix} \mathbf{v}(aN_{tot} + N_g) \\ \vdots \\ \mathbf{v}(aN_{tot} + N_g + N_c - 1) \end{pmatrix}, \tag{2.7}$$

where $N_{tot} = N_c + N_g$ and $\mathbf{C}$ is a $N_c N_R \times N_c N_T$ block circulant matrix.

Let $\mathbf{s}(i,a) = [s_1(i,a), \ldots, s_{N_T}(i,a)]^T$ represents the MIMO vector transmitted on the i-th subcarrier of the a-th MIMO-OFDM symbol, where $s_p(i,a)$ is the p-th element transmitted in the p-th Tx antenna. The transmitted block of samples in the time-domain is

$$\hat{\mathbf{u}}(a) = (\mathbf{F}^{-1} \otimes \mathbf{I}_{N_T}) \begin{pmatrix} \mathbf{s}(0,a) \\ \vdots \\ \mathbf{s}(N_c - 1, a) \end{pmatrix}, \tag{2.8}$$

where $\otimes$ denotes the Kronecker product, $\mathbf{I}_k$ is the k-size identity matrix, and $\mathbf{F}$ is the $N_c \times N_c$ Fourier matrix where the (i,k)-th element equals $\exp(-j2\pi(ik/N_c))$, where $j = \sqrt{-1}$ is the imaginary unit. The received signal after the FFT block is given by

$$\hat{\mathbf{x}}(a) = (\mathbf{F} \otimes \mathbf{I}_{N_R})\hat{\mathbf{y}}(a). \tag{2.9}$$

Then, replacing Eq. (2.5) and Eq. (2.8) into Eq. (2.9), the frequency domain MIMO-OFDM baseband signal model is expressed by

$$\hat{\mathbf{x}}(a) = \hat{\mathbf{H}}\hat{\mathbf{s}}(a) + \hat{\mathbf{n}}(a), \tag{2.10}$$

where $\hat{\mathbf{n}}(a)$ represents the frequency domain noise complex Gaussian elements with variance $(1/2)\sigma_n^2$ and i.i.d. zero-mean, $\hat{\mathbf{s}}(a)$ is given by

$$\hat{\mathbf{s}}(a) = \begin{pmatrix} \mathbf{s}(0,a) \\ \vdots \\ \mathbf{s}(N_c - 1, a) \end{pmatrix}, \tag{2.11}$$

and $\hat{\mathbf{H}}$ is a block diagonal matrix given by

$$\hat{\mathbf{H}} = \begin{pmatrix} \mathbf{H}(0) & & 0 \\ & \ddots & \\ 0 & & \mathbf{H}(N_c - 1) \end{pmatrix}. \tag{2.12}$$

The i-th block diagonal element is the $N_T \times N_R$ MIMO channel of the i-th subcarrier and is defined by

$$\mathbf{H}(i) = \sum_{l=0}^{L-1} \mathbf{G}(l) \exp\left(-j2\pi \frac{il}{N_c}\right), \tag{2.13}$$

and for that subcarrier

$$\mathbf{x}(i,a) = \mathbf{H}(i)\mathbf{s}(i,a) + \mathbf{n}(i,a), \tag{2.14}$$

which results in a flat-fading signal model per subcarrier.

2.2 Antenna Diversity

Antenna diversity, also known as space or spatial diversity, is a well known technique utilized to overcome the problem of multipath propagation that is present in wireless communication systems [24]. In a real communications scenario, the signal sent to the receiver travels through several paths and it is affected in different ways due to the random characteristics of the wireless channels. This phenomenon is know as *multipath fading*, and it can greatly reduce the quality and reliability of a wireless link. Figure 2.6 presents a wireless communication system with antenna diversity in the receiver side. In the left part of the figure the multipath propagation of the signal is illustrated. The signal sent by the transmitter travels through three different paths and reach the receiver that is equipped with two antennas. These antennas are spatially separated and receive different replicas of the transmitted signal. These received signals experienced different fading; hence, they are combined to improve the signal quality.

The main ways to combine the signals are: selection, equal gain, and maximal ratio combining (MRC). In selection combining, the strongest signal is selected; while in equal gain combing all signals are summed with equal weight. In MRC, the signals are weighted according to the channel state information (CSI), then summed. Among these three techniques, MRC obtains the best diversity gain; although, it requires a priori known of the CSI.

The main limitations of a receiver with antenna diversity are the additional hardware required and the separation between antennas. As observed in Fig. 2.6,

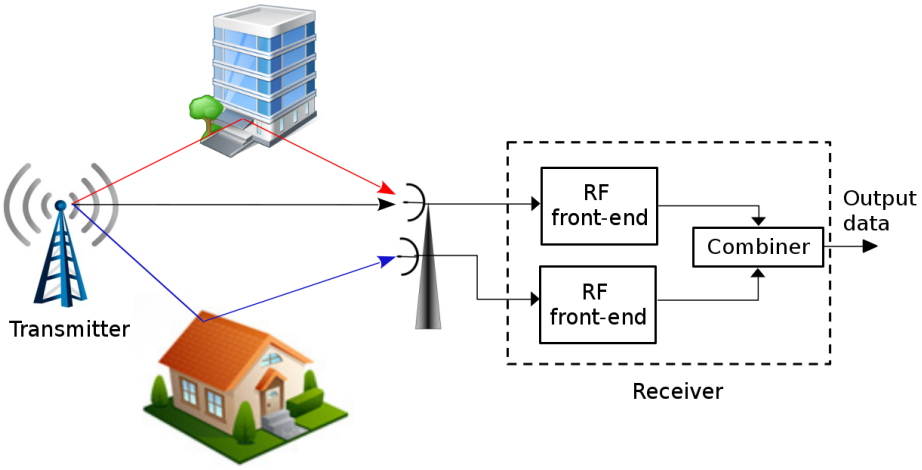

Figure 2.6: Multipath fading and receiver with antenna diversity.

the receiver requires two antennas, two RF front-end circuits, a combiner, and additional cabling for the antennas. This increases the hardware complexity and energy consumption. The other limitation is that the separation between the antennas should be big enough to offer signals that suffered independent fading. These two limitations make it difficult to implement in hand-held devices, which have the constraints of small size and limited power.

2.3 ESPAR Antenna

An ESPAR antenna is a small size and low power consumption antenna [25, 26]. It is composed of a radiator element, which is connected to the RF front-end, and one or more parasitic (passive) elements loaded by variable reactances. The antenna's directivity is controlled by changing the bias voltage supplied to the variable reactances. A 7-element ESPAR antenna is shown in Fig. 2.7. The radiator element, which is located in the center, is connected to the RF front-end of the receiver. The six surrounding elements are the parasitic elements which are connected to variable capacitance diodes (varactor). The main applications of ESPAR antenna are: adaptive analog beamforming at the receiver [27], reactance diversity receiver [28, 29], and MIMO transmission using a single RF front-end [30, 31].

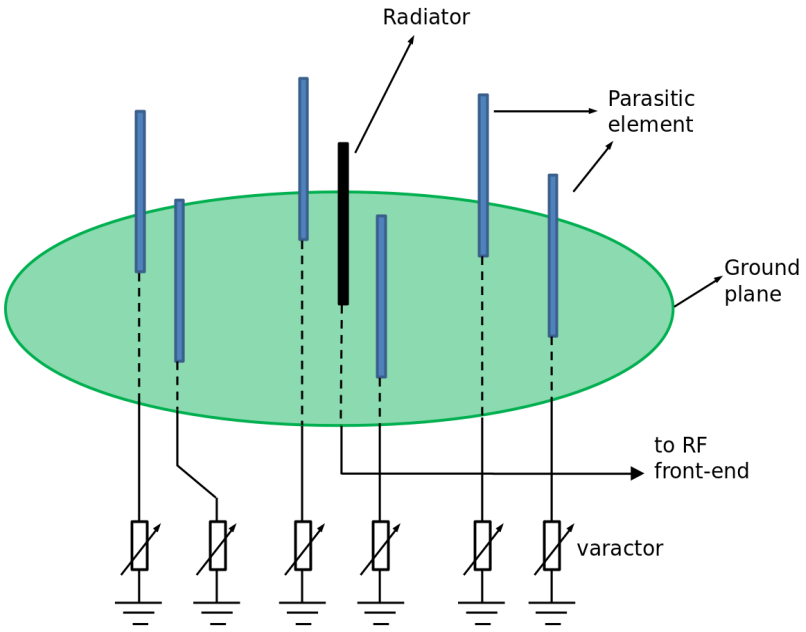

Figure 2.7: 7-element ESPAR antenna.

To explain the effect of the ESPAR antenna in the received signal, let us consider the 3-element ESPAR antenna presented in Fig. 2.8. It is composed of the radiator element (#0) and two parasitic elements (#1,#2). The distance d between the elements can be as small as 0.05λ [29], where λ is the wavelength.

The impedance matrix, which results from the mutual coupling between the different antenna elements, is given by

$$\mathbf{Z} = \begin{bmatrix} Z_{00} & Z_{01} & Z_{02} \\ Z_{10} & Z_{11} & Z_{12} \\ Z_{20} & Z_{21} & Z_{22} \end{bmatrix}, \tag{2.15}$$

where Z_{ii} is the self-impedance of the i-th antenna element and Z_{kl} (for $k \neq l$) is the mutual-impedance between the k-th and l-th element. The values of $\mathbf{Z}$ can be obtained from the Numerical Electromagnetics Code (NEC) simulator [32].

Let $\mathbf{X}$ define the diagonal matrix

$$\mathbf{X} = \begin{bmatrix} Z_0 & 0 & 0 \\ 0 & jx_1 & 0 \\ 0 & 0 & jx_2 \end{bmatrix}, \tag{2.16}$$

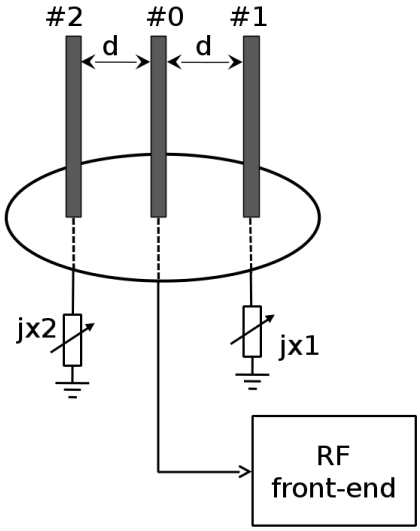

Figure 2.8: 3-element ESPAR antenna.

where Z_0 is the load impedance, $j = \sqrt{-1}$ is the imaginary unit, and jx_1, jx_2 are the variable reactances of the parasitic elements. Let us also define the vector

$$\mathbf{u}_0 = [1, 0, 0]^T, \tag{2.17}$$

where $[\cdot]^T$ represents the transpose of the vector. Referring to [27, 29], the equivalent weight vector $\mathbf{w}$ is defined as

$$\mathbf{w} = 2Z_0(\mathbf{Z} + \mathbf{X})^{-1}\mathbf{u}_0. \tag{2.18}$$

The steering vector $\boldsymbol{\alpha}(\gamma)$ is based on the array geometry of the 3-element ESPAR antenna presented in Fig. 2.8 and is defined as

$$\boldsymbol{\alpha}(\gamma) = [1, e^{j2\pi d\cos(\gamma)}, e^{j2\pi d\cos(\gamma-\pi)}]^T, \tag{2.19}$$

where γ is the azimuthal direction of the incoming waves. Hence, in receiving mode the voltage signal $r(t)$ at the RF port is given by

$$r(t) = \mathbf{w}^T\boldsymbol{\alpha}(\gamma)s(t), \tag{2.20}$$

where $s(t)$ represents the incident waves.

2.4 OFDM Receiver using ESPAR Antenna with Periodically Alternating Directivity

An OFDM diversity receiver using an ESPAR antenna with periodically alternating directivity was presented in [12]. The block diagram of this scheme is shown in Fig. 2.9. It is composed of a 2-element ESPAR antenna, RF front-end, ADC, FFT block, channel estimator, and frequency domain equalizer. The variable capacitance, which is connected to the parasitic element of the antenna, is controlled by a periodic wave whose frequency is the OFDM symbol rate. Since the variable capacitance is periodically changing, the directivity of the ESPAR antenna is also periodically changing.

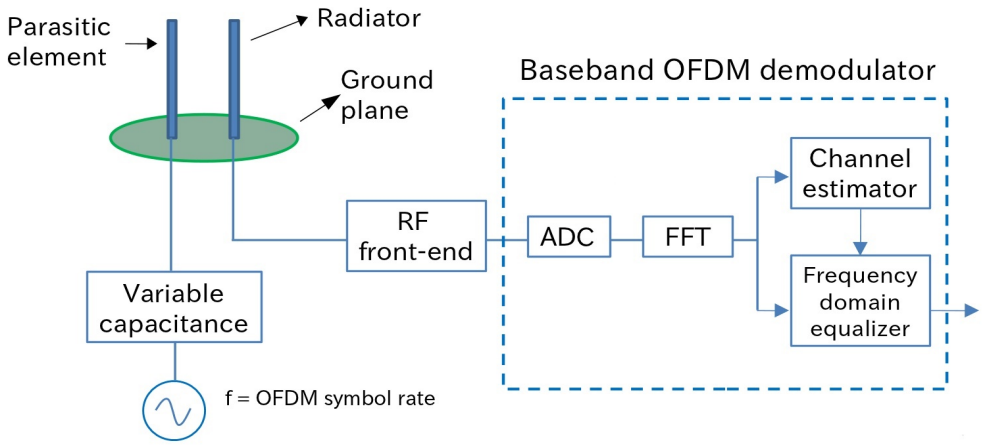

Figure 2.9: Block diagram of the OFDM receiver using an ESPAR antenna with periodically alternating directivity.

The signal at the output of the RF front-end is the weighted sum of the signal received in each antenna element. Considering an ideal design of the antenna, the frequency domain signal at the output of the FFT block is the sum of three components and can be expressed by

$$\mathbf{u} = \mathbf{G}_{-1}\mathbf{H}_{-1}\mathbf{x} + \mathbf{H}_0\mathbf{x} + \mathbf{G}_1\mathbf{H}_1\mathbf{x} + \mathbf{z}, \tag{2.21}$$

where $\mathbf{x}$ is the vector of transmitted symbols in frequency domain, $\mathbf{z}$ is the vector of AWGN noise, and $\mathbf{H}_0, \mathbf{H}_{-1}, \mathbf{H}_1$ are the channel frequency response matrices

of the frequency non-shifted, negative frequency shifted, and positive frequency shifted components of the signal, respectively. The matrices $\mathbf{G}_{-1}$ and $\mathbf{G}_1$ are composed of a diagonal of ones that is shifted upwards and downwards, respectively. They are given by

$$\mathbf{G}_{-1} = \begin{pmatrix} 0 & 1 & 0 & \dots & 0 \\ 0 & 0 & 1 & \ddots & \vdots \\ \vdots & \vdots & 0 & \ddots & 0 \\ 0 & \vdots & \vdots & \ddots & 1 \\ 1 & 0 & 0 & \dots & 0 \end{pmatrix} \tag{2.22}$$

and

$$\mathbf{G}_1 = \begin{pmatrix} 0 & 0 & \dots & 0 & 1 \\ 1 & 0 & \ddots & \vdots & 0 \\ 0 & 1 & \ddots & \vdots & \vdots \\ \vdots & \ddots & \ddots & 0 & \vdots \\ 0 & \dots & 0 & 1 & 0 \end{pmatrix}. \tag{2.23}$$

The channel frequency response matrix $\mathbf{H}$ can be expressed by

$$\mathbf{H} = \mathbf{G}_{-1}\mathbf{H}_{-1} + \mathbf{H}_0 + \mathbf{G}_1\mathbf{H}_1, \tag{2.24}$$

and its matrix structure is shown in Eq. (2.25). The element $H_0(k)$ in red is the frequency response of the non-shifted component at the k-th subcarrier. Similarly, the elements in blue and green corresponds to the positive and negative frequency shifted components, respectively.

$$\mathbf{H} = \begin{pmatrix} H_0(0) & H_{-1}(1) & 0 & \dots & \dots & \dots & 0 & H_1(N-1) \\ H_1(0) & H_0(1) & \ddots & \ddots & \dots & \dots & \dots & 0 \\ 0 & H_1(1) & \ddots & \ddots & \ddots & \dots & \dots & \vdots \\ \vdots & 0 & \ddots & \ddots & \ddots & \ddots & \dots & \vdots \\ \vdots & \dots & \ddots & \ddots & \ddots & \ddots & 0 & \vdots \\ \vdots & \dots & \dots & \ddots & \ddots & \ddots & H_{-1}(N-2) & 0 \\ 0 & \dots & \dots & \dots & \ddots & \ddots & H_0(N-2) & H_{-1}(N-1) \\ H_{-1}(0) & 0 & \dots & \dots & \dots & 0 & H_1(N-2) & H_0(N-1) \end{pmatrix} \tag{2.25}$$

Due to the special structure of the channel matrix $\mathbf{H}$, this receiver requires a special channel estimation. It uses a pilot symbol that is transmitted prior to the data symbols and is defined as

$$\mathbf{p} = [p_1, p_2, \dots, p_N]^T, \tag{2.26}$$

where p_k is the pilot element of the k-th subcarrier and N is the total number of subcarriers. When the pilot symbol is transmitted, Eq. (2.21) can be expressed as

$$\mathbf{u} = \mathbf{G}_{-1}\mathbf{P}\mathbf{h}_{-1} + \mathbf{P}\mathbf{h}_0 + \mathbf{G}_1\mathbf{P}\mathbf{h}_1 + \mathbf{z}, \tag{2.27}$$

where $\mathbf{P}$=diag($\mathbf{p}$) is a matrix whose diagonal elements are the pilot symbols and $\mathbf{h}_i$ is a vector with the diagonals elements of $\mathbf{H}_i$, i={-1,0,1}. Using the minimum mean square error (MMSE) criteria, the auto-correlation matrix $\mathbf{R}_u$=E[$\mathbf{u}\mathbf{u}^H$] is given by

$$\mathbf{R}_u = \mathbf{G}_{-1}\mathbf{P}\mathbf{R}_h\mathbf{P}^H\mathbf{G}_{-1}^H + \mathbf{P}\mathbf{R}_h\mathbf{P}^H + \mathbf{G}_1\mathbf{P}\mathbf{R}_h\mathbf{P}^H\mathbf{G}_1^H + \sigma_z^2\mathbf{I}, \tag{2.28}$$

where σ_z^2 is the noise variance and $\mathbf{R}_h$ is the covariance matrix that is modeled as an exponential decaying filter which is given by

$$\mathbf{R}_h(l,k) = \frac{1}{1 + j2\pi f_s(l-k)\tau}, \tag{2.29}$$

where f_s is the subcarrier frequency spacing and τ is the root mean squared delay of the channel.

The cross-correlation matrices are given by

$$\mathbf{B}_{-1} = \mathbf{G}_{-1}\mathbf{P}\mathbf{R}_h, \tag{2.30}$$

$$\mathbf{B}_0 = \mathbf{P}\mathbf{R}_h, \tag{2.31}$$

$$\mathbf{B}_1 = \mathbf{G}_1\mathbf{P}\mathbf{R}_h. \tag{2.32}$$

Then, the estimated channel response of every frequency component is given by

$$\widetilde{\mathbf{h}}_i = (\mathbf{R}_u^{-1}\mathbf{B}_i)^H\mathbf{u}. \tag{2.33}$$

2.5 RF Signal Processing-based Diversity Scheme for MIMO-OFDM Systems

This work proposed a diversity scheme for a MIMO-OFDM system [13], and it uses a similar idea to the work presented in [12]. Although, instead of using a 2-element ESPAR antenna, it proposed to use a 2-element phased array antenna. This RF signal processing scheme is a MIMO-OFDM system with two transmitters and two receivers. It achieved diversity gain but its two main disadvantages are very high computational cost for the detection and that usually the phased array antennas are expensive; thus, it was not suitable for low cost implementation.

The block diagrams of the transmitter and receiver are shown in Fig. 2.10 and 2.11, respectively. The transmitter is based on the WLAN standard IEEE 802.11n [9]. The input data is divided into two independent streams and each transmitter branch modulates it, obtains the IFFT, and adds a guard interval (GI). Finally, the symbols of every stream are transmitted simultaneously by both antennas. Therefore, this is a spatial multiplexing system [16].

The receiver uses a 2-element phased array antenna composed of a phase non-shifting and phase shifting element. The phase of the shifting element is periodically changing at the OFDM symbol rate. After the ADC, the GI is removed and every signal is fed to the FFT block. Like in [12], an MMSE channel estimator is used to obtain the channel state information. Let $\mathbf{p}_i$ be the pilot symbol vector transmitted by the i-th transmitter. When the pilot symbol is

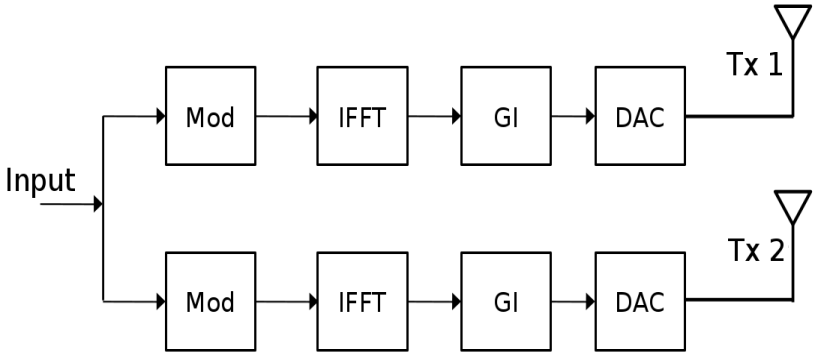

Figure 2.10: Block diagram of the WLAN MIMO-OFDM transmitter.

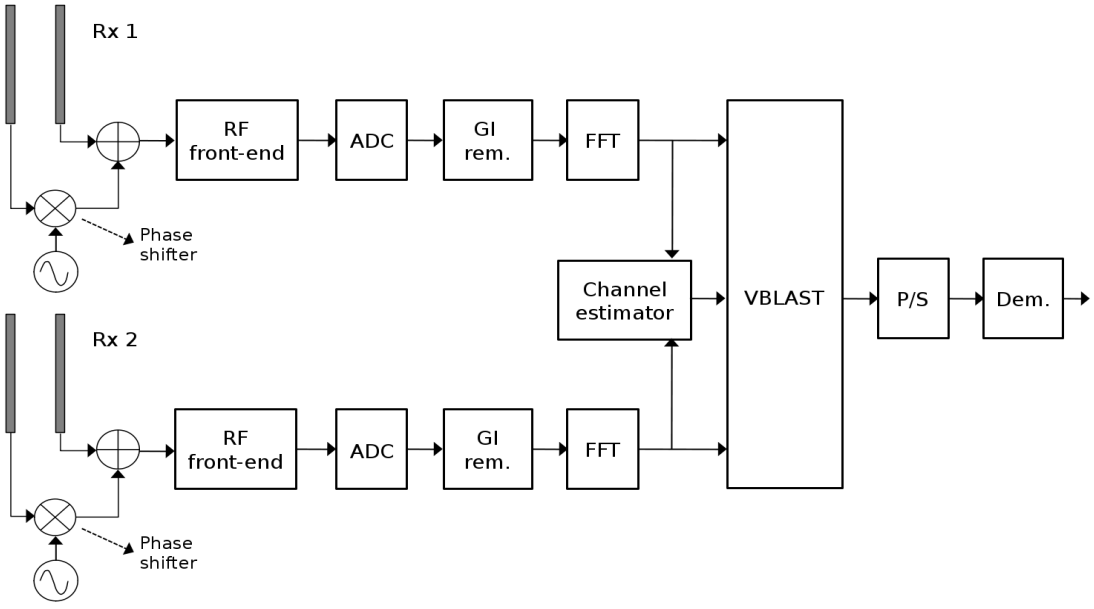

Figure 2.11: Block diagram of the MIMO-OFDM receiver with RF signal processing diversity.

transmitted, the received signal at the output of the FFT for the i-th receiver is given by

$$\mathbf{u_i} = \mathbf{P}_1\mathbf{h}_{i,1}^{ns} + \mathbf{G}\mathbf{P}_1\mathbf{h}_{i,1}^{s} + \mathbf{P}_2\mathbf{h}_{i,2}^{ns} + \mathbf{G}\mathbf{P}_2\mathbf{h}_{i,2}^{s} + \mathbf{z}, \tag{2.34}$$

where $\mathbf{h}_{i,l}^{ns}$ and $\mathbf{h}_{i,l}^{s}$ are the channel response between the i-th receive antenna and l-th transmit antenna for the phase non-shifted (ns) and phase shifted (s) elements, respectively. $\mathbf{P}_i$=diag($\mathbf{p}_i$) is a matrix whose diagonal elements are the pilot symbols and $\mathbf{z}$ is the AWGN vector. The matrix $\mathbf{G}$ is defined as

$$\mathbf{G} = \begin{pmatrix} 0 & 0 & \dots & 0 & 1 \\ 1 & 0 & \ddots & \vdots & 0 \\ 0 & 1 & \ddots & \vdots & \vdots \\ \vdots & \ddots & \ddots & 0 & \vdots \\ 0 & \dots & 0 & 1 & 0 \end{pmatrix}. \tag{2.35}$$

The auto-correlation matrix $\mathbf{R}$=E[$\mathbf{u}_i\mathbf{u}_i^H$] is given by

$$\mathbf{R}_u = \mathbf{P}_1\mathbf{R}_h\mathbf{P}_1^H + \mathbf{G}\mathbf{P}_1\mathbf{R}_h\mathbf{P}_1^H\mathbf{G}^H + \mathbf{P}_2\mathbf{R}_h\mathbf{P}_2^H + \mathbf{G}\mathbf{P}_2\mathbf{R}_h\mathbf{P}_2^H\mathbf{G}^H + \sigma_z^2\mathbf{I}, \tag{2.36}$$

where σ_z^2 is the noise variance and $\mathbf{R}_h$ is the covariance matrix defined in Eq. (2.29). The cross-correlation matrices $\mathbf{B}_i$=E[$\mathbf{u}\mathbf{h}^H$] are given by

$$\mathbf{B}_i^{ns} = \mathbf{P}_i\mathbf{R}_h, \tag{2.37}$$

$$\mathbf{B}_i^{s} = \mathbf{G}\mathbf{P}_i\mathbf{R}_h. \tag{2.38}$$

Finally, the estimated frequency channel response between the i-th receive antenna and l-th transmit antenna for the phase non-shifted and phase shifted elements is given by

$$\widetilde{\mathbf{h}}_{i,l}^{ns} = (\mathbf{R}_u^{-1}\mathbf{B}_i^{ns})^H\mathbf{u}_i, \tag{2.39}$$

$$\widetilde{\mathbf{h}}_{i,l}^{s} = (\mathbf{R}_u^{-1}\mathbf{B}_i^{s})^H\mathbf{u}_i. \tag{2.40}$$

For detection, Vertical-Bell Laboratories Layered Space-Time (VBLAST) [33, 34] is used. The proposed RF signal processing diversity needs to detect all subcarriers simultaneously so the channel frequency response matrix $\mathbf{H}$ has a large

size. Additionally, the VBLAST detector has a complexity in the order of $O(n^4)$; thus, the detection precess demands a huge computational effort. Consequently, it cannot be practically implemented and becomes the main limitation of this scheme.

2.6 Compressed Sensing

Compressed sensing (CS), which is also known as compressive sensing or compressive sampling, is a new methodology that allows the recovery of sparse signals from much fewer measurements than what is conventionally required [35, 36]. It is based on the assumption that a lot of signals on the real world are sparse in some transform domain, i.e. mostly negligibly small or zero. This methodology is being applied to several fields such as: imaging, data acquisition, magnetic resonance imaging (MRI), radar, data compression, and channel estimation in wireless communications [37].

A standard linear measurement model is defined by

$$\mathbf{r} = \mathbf{\Psi}\boldsymbol{\theta}, \tag{2.41}$$

where $\mathbf{r}$ is an n-size observation vector, $\mathbf{\Psi}$ is an $n \times m$ measurement matrix with $n<m$, and $\boldsymbol{\theta}$ is a m-size unknown S-sparse vector with S non-zero elements. Figure 2.12 shows a representation of this model. In this figure, we can observe that it is an under-determined system with fewer equations than unknowns. The knowledge of the sparsity of the unknown vector $\boldsymbol{\theta}$ is used in CS to obtain a unique solution for the system.

The possibility of recovering a signal in CS depends mainly in: the sparsity of $\boldsymbol{\theta}$, the measurement matrix $\mathbf{\Psi}$, and the recovery algorithm. The restricted isometry property (RIP) [38, 39] is an important requirement for the measurement matrix $\mathbf{\Psi}$. A matrix $\mathbf{\Psi}$ with unit ℓ_2-norm columns satisfies the RIP of order S if there exists a constant $\delta_S \in (0, 1)$ which is the smallest number such that

$$(1 - \delta_S)\|\boldsymbol{\theta}\|_2^2 \leq \|\mathbf{\Psi}\boldsymbol{\theta}\|_2^2 \leq (1 + \delta_S)\|\boldsymbol{\theta}\|_2^2 \tag{2.42}$$

is valid for any $\boldsymbol{\theta}$ that has S non-zero elements. Calculating the RIP for a matrix is a very difficult problem and up to date there is no algorithm that can check

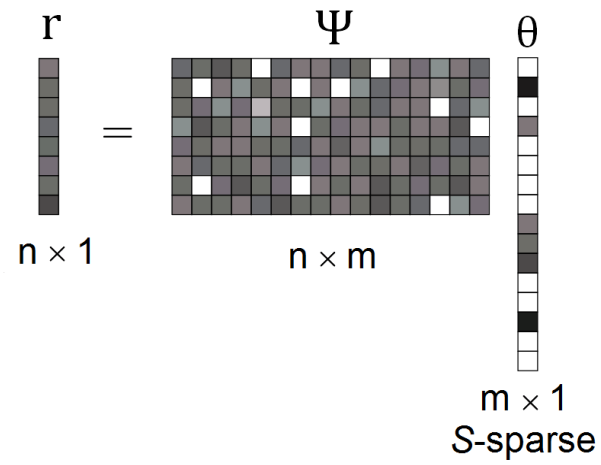

Figure 2.12: Illustration of the linear model of compressed sensing.

the RIP in polynomial time [40]. However, it has been demonstrated that several matrices satisfy the RIP condition with high probability. For example, an $n \times m$ random matrix, whose entries are independent and identically distributed samples of a sub-Gaussian distribution, satisfy with high probability the RIP of order S if the number of observations is given by [41]

$$n = O\left(S \log\left(\frac{m}{S}\right)\right). \tag{2.43}$$

It is also well known that matrices whose columns were selected from an orthogonal matrix, like the discrete Fourier transform (DFT), have a high probability of following the RIP condition if the number of observations is given by [42, 43]

$$n = O\left(S \log^4\left(\frac{m}{S}\right)\right). \tag{2.44}$$

The results of Eq. (2.43) and Eq. (2.44) shows that in CS the required number of observations grows linearly with S but logarithmically with m.

A logical approach to obtain a sparse solution to the under-determined system of Eq. (2.41) is to minimize the number of non-zero elements in $\boldsymbol{\theta}$. This optimization problem, which is known as ℓ_0-minimization, is given by

$$\hat{\boldsymbol{\theta}} = \arg\min_{\boldsymbol{\theta} \in \mathbb{C}^m} \|\boldsymbol{\theta}\|_0 \quad \text{s.t. } \mathbf{r} = \boldsymbol{\Psi}\boldsymbol{\theta}, \tag{2.45}$$

where $\|\cdot\|_0$ denotes the ℓ_0-norm. However, this is a non-convex optimization

problem that is very difficult to solve. The outstanding characteristic of CS is that if the RIP of $\boldsymbol{\Psi}$ is satisfied, the ℓ_0-minimization is equivalent to the convex optimization problem given by

$$\hat{\boldsymbol{\theta}} = \arg \min_{\boldsymbol{\theta} \in \mathbb{C}^m} \|\boldsymbol{\theta}\|_1 \quad \text{s.t. } \mathbf{r} = \boldsymbol{\Psi}\boldsymbol{\theta}, \tag{2.46}$$

where $\|\cdot\|_1$ denotes the ℓ_1-norm which is equivalent to the sum of the absolute values of the elements of $\boldsymbol{\theta}$.

In the case of noisy observations, Eq. (2.41) can be expressed as

$$\mathbf{r} = \boldsymbol{\Psi}\boldsymbol{\theta} + \boldsymbol{\eta}, \tag{2.47}$$

where $\|\boldsymbol{\eta}\|_2 \leq \epsilon$, for a given constant $\epsilon > 0$. Then, the ℓ_1-minimization problem is given by

$$\hat{\boldsymbol{\theta}} = \arg \min_{\boldsymbol{\theta} \in \mathbb{C}^m} \|\boldsymbol{\theta}\|_1 \quad \text{s.t. } \|\mathbf{r} - \boldsymbol{\Psi}\boldsymbol{\theta}\|_2 \leq \epsilon. \tag{2.48}$$

For the case of AWGN with zero mean and σ^2 noise variance, the Dantzig selector (DS) [44] is formulated as

$$\hat{\boldsymbol{\theta}} = \arg \min_{\tilde{\boldsymbol{\theta}} \in \mathbb{C}^m} \|\boldsymbol{\theta}\|_1 \quad \text{s.t. } \|\boldsymbol{\Psi}^H(\mathbf{r} - \boldsymbol{\Psi}\boldsymbol{\theta})\|_\infty \leq \xi, \tag{2.49}$$

where $\|\cdot\|_\infty$ denotes the ℓ_∞-norm and ξ is given by

$$\xi = \sqrt{2\sigma^2(1+a)\log m}, \tag{2.50}$$

for any $a \geq 0$.

The main disadvantage of the algorithms based on ℓ_1-minimization is its high computational cost. Another option for recovering the sparse signal is the family of iterative greedy algorithms. Some of the most relevant algorithms of this family are: orthogonal matching pursuit (OMP) [45], regularized OMP (ROMP) [46], compressive sampling matching pursuit (CoSaMP) [47], and subspace pursuit (SP) [48]. The advantages of these algorithms are simple implementation and low computational cost. In general, the greedy algorithms may lead to a local minimum instead of the optimal solution [49]. However, some recent works have also shown that they can obtain an optimal solution, but requiring tighter conditions like a slightly higher number of observations [37].

In OMP, the idea is to pick at each iteration a column of the measurement matrix in a greedy way. This column is the most correlated with the residual and is added to a subset. Using least squares, a new signal estimation is obtained and subtracted from the original signal. This process is iterated S times, where S is the sparsity of the unknown signal $\boldsymbol{\theta}$. The pseudocode of the OMP algorithm is presented in Alg. 2.1.

Algorithm 2.1 Orthogonal matching pursuit (OMP)

Input: $\mathbf{r}$ (n-size observation vector)
Input: $\boldsymbol{\Psi}$ ($n \times m$ measurement matrix)
Input: S (sparsity level)
$\mathbf{v}_0 := \mathbf{r}$, $\Lambda_0 := \emptyset$, $\boldsymbol{\Phi}_0 := [\ ]$
for $t = 1, \ldots, S$ **do**
    $\lambda_t :=$arg $\max_{j=1,\ldots,m} |\boldsymbol{\psi}_j^T \mathbf{v}_{t-1}|$
    $\Lambda_t := \Lambda_{t-1} \cup \lambda_t$
    $\boldsymbol{\Phi}_t := [\boldsymbol{\Phi}_{t-1} \ \ \boldsymbol{\psi}_{\lambda_t}]$
    $\mathbf{y}_t :=$arg $\min_y \|\mathbf{r} - \boldsymbol{\Phi}_t \mathbf{y}\|_2^2$
    $\mathbf{v}_t := \mathbf{r} - \boldsymbol{\Phi}_t \mathbf{y}_t$
end for
Output: $\tilde{\boldsymbol{\theta}}$ (composed of $\mathbf{y}_t$ values at Λ_t positions)

For the OMP algorithm, the RIP has been analyzed in several works including [45, 50], and it is still a topic of research. The limitation of these analyses is that the case of noisy observations is not considered; however, other greedy algorithms consider this case. Nonetheless, the more practical way to determine the efficiency of an algorithm for a specific measurement matrix and number of observations is using numerical simulations [51].

In the real world, some signals are sparse but also can have a common structure. An example is the channel impulse response (CIR) in the ISDB-T system, where one frame is composed of multiple OFDM symbols. The CIR of the symbols in a frame has a small variation so the positions of the non-zero elements can be considered to be the same for all OFDM symbols in the frame. Structured CS [52] can exploit this property to whether reduce the number of required observations or improve the recovery efficiency. For structured CS, the linear measurement model is given by

$$\mathbf{Y} = \mathbf{\Psi X}, \tag{2.51}$$

where $\mathbf{Y}$ is an $n \times q$ matrix with its columns being the observation vectors, $\mathbf{\Psi}$ is an $n \times m$ measurement matrix with $n<m$, and $\mathbf{X}$ is an $m \times q$ unknown matrix with S non-zero rows. Each column of $\mathbf{X}$ is a sparse vector that share the same non-zero positions (common support). To exploit this joint information, there is a variation of OMP called simultaneous OMP (SOMP) [53].

The pseudocode of SOMP is presented in Alg. 2.2. The main differences to OMP are first that in SOMP the input is the matrix of observation vectors $\mathbf{X}$. Also, it uses a residual matrix $\mathbf{R}$ and the solution of the least squares problem is the matrix $\mathbf{W}$. Another difference is how to obtain the most correlated column with the residual, which is shown in line (6). It looks for the maximum norm of the vector resulting from $\boldsymbol{\psi}_j^T \mathbf{R}_{t-1}$. The output $\tilde{\mathbf{Y}}$ is also a matrix that has non-zero rows in the positions given by the index set Λ_t.

Algorithm 2.2 Simultaneous orthogonal matching pursuit (SOMP)

1: Input: $\mathbf{X}$ ($n \times q$ matrix of observation vectors)
2: Input: $\mathbf{\Psi}$ ($n \times m$ measurement matrix)
3: Input: S (sparsity level)
4: $\mathbf{R}_0 := \mathbf{X}$, $\Lambda_0 := \emptyset$, $\mathbf{\Phi}_0 := [\ ]$
5: **for** $t = 1, \ldots, S$ **do**
6: $\quad \lambda_t :=$arg $\max_{j=1,\ldots,m} \|\boldsymbol{\psi}_j^T \mathbf{R}_{t-1}\|$
7: $\quad \Lambda_t := \Lambda_{t-1} \cup \lambda_t$
8: $\quad \mathbf{\Phi}_t := [\mathbf{\Phi}_{t-1} \ \ \boldsymbol{\psi}_{\lambda_t}]$
9: $\quad \mathbf{W}_t :=$arg $\min_W \|\mathbf{X} - \mathbf{\Phi}_t \mathbf{W}\|_2^2$
10: $\quad \mathbf{R}_t := \mathbf{X} - \mathbf{\Phi}_t \mathbf{W}_t$
11: **end for**
12: Output: $\tilde{\mathbf{Y}}$ (composed of rows of $\mathbf{W}_t$ at indices Λ_t)

Chapter 3

MIMO-OFDM Receiver with 3-element ESPAR Antenna

This chapter presents a MIMO-OFDM receiver with 3-element ESPAR antenna and the detail of its components. First, the system model of the receiver is presented. Then, two channel estimation schemes that obtain the channel state information are presented. Next, the problem of designing a low complexity detection scheme and also the synchronization are addressed. Finally, the simulation results are presented to discuss the performance of the ESPAR antenna-based MIMO-OFDM receiver.

3.1 Introduction

A MIMO-OFDM system combines the advantages of MIMO systems with OFDM modulation; thus, it increases the channel capacity while being robust to multipath fading and ISI. Due to these advantages, it can provide high data rates in wireless communications systems. It is used in some of the leading standards like: WLAN IEEE 802.11n [9], WLAN IEEE 802.11ac [10], and LTE [11].

Antenna diversity is a well known technique which is utilized to overcome the problem of multipath fading [24]. This technique can be used in MIMO-OFDM systems to obtain diversity gain, but it increases the number of RF chains in the receiver. Every RF chain is composed of an antenna, RF front-end, FFT block, and other electronics circuits. Therefore, antenna diversity has the disadvantages

of increased hardware complexity, energy consumption, and receiver size.

An ESPAR antenna is a small size and low power consumption antenna [25, 26]. Recently, an OFDM diversity receiver using a 2-element ESPAR antenna with periodically alternating directivity was presented in [12]. This receiver obtained diversity gain and improved the BER performance without additional RF chains; therefore, it solves some of the disadvantages of the antenna diversity technique. However, it requires special channel estimation and detection schemes that increase the computational cost of the receiver. An RF signal processing-based diversity scheme for MIMO-OFDM was proposed in [13], and it used a similar idea to the work proposed in [12]. Although, it utilized a 2-element phased array instead of an ESPAR antenna. This scheme was able to obtain diversity gain in a MIMO-OFDM system; however, the computational cost of the detection was too high and the 2-element phased array is an expensive antenna. Consequently, it was not suitable for low-cost practical implementation.

In this chapter, a MIMO-OFDM receiver using a 3-element ESPAR antenna with periodically alternating directivity is presented. Compared to the conventional 2×2 MIMO-OFDM systems, this scheme achieves diversity gain and substantially improves the BER performance. Due to the different signal model, this receiver requires special channel estimation and detection schemes. For channel estimation, an MMSE estimator is designed with the assumption of having rich multipath channels. However, some recent studies have shown that in practice, real multipath channels with large bandwidth tend to exhibit a sparse structure. This multipath channel is composed of few propagation paths with different delays. Almost all of the CIR components are either zero or below the noise floor, except for the few delayed path components [37]. This means that the multipath channel has a sparse structure.

Compressed sensing, which was presented in Chapter 2, is a new methodology that allows the recovery of sparse signals from much fewer measurements than what is conventionally required [35, 36]. Recently, CS has been used for the channel estimation of wireless communication systems [37, 40]. Compared to conventional channel estimation schemes, CS-based channel estimation can whether reduce the pilot overhead or improve the estimation accuracy [54]. The CS-based channel estimation has also been proposed for MIMO-OFDM systems

[55, 56]. However, the challenge of using CS-based channel estimation for the MIMO-OFDM receiver with ESPAR antenna is that the channel response of the three antenna elements has to be simultaneously estimated. This is a challenge because it is necessary to estimate three different channel impulse response without increasing the number of pilots that are used for channel estimation. A simultaneous multichannel reconstruction using CS has been recently proposed in [57]; however, it is focused in a different channel and OFDM technology. In this chapter, a CS-based channel estimation for the proposed MIMO-OFDM receiver with ESPAR antenna is also presented. First, the channel estimation is expressed as a CS problem and then, a modified version of the OMP [45] recovery algorithm is proposed to reduce the required computational cost and improve the recovery accuracy.

Another requirement of the proposed receiver is low complexity detection. The MIMO-OFDM receiver presented in [13] used the VBLAST [33, 34] algorithm for detection. The limitation of VBLAST is that its computational cost is in the order of $O(n^4)$ for an $n \times n$ channel matrix. Additionally, the channel matrix had a large size so the computational cost of the detection was huge. In the case of the proposed MIMO-OFDM receiver with 3-element ESPAR antenna, it also has a large channel matrix that cannot be processed per subcarrier. Despite of its large size, the channel matrix is composed of only a few non-zero diagonals. Therefore, the sparsity can be exploited to reduce the computational cost of the detection. The MMSE sparse-sorted QR decomposition (MMSE sparse-SQRD) detection exploits the sparsity and can considerably reduce the required computational cost. To further reduce the computational cost of the detection, this chapter also presents a submatrix divided detection scheme that divides the channel matrix into smaller submatrices. In spite of introducing a small degradation in the BER, this scheme reduces the computational cost.

3.2 System Model

The system model consist of a MIMO-OFDM scheme with two transmitters and two receivers. The transmitter is based on the WLAN IEEE 802.11n standard [9] and its block diagram is shown in Fig. 3.1. Each transmitter branch performs

the modulation, IFFT, and GI insertion. For simplicity, forward error correction (FEC) and interleaver blocks are not included as part of the system. It is important to remark that the transmitter uses conventional antennas for transmitting the signal.

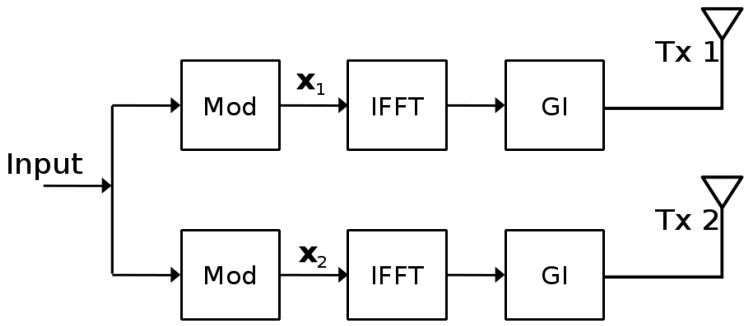

Figure 3.1: Block diagram of the MIMO-OFDM transmitter.

The MIMO-OFDM receiver uses a 3-element ESPAR antenna with periodically alternating directivity. The physical model of this ESPAR antenna is presented in Fig. 3.2. It is composed of a radiator element (#0) and two parasitic elements (#1, #2). The directivity of the ESPAR antenna is periodically changed by the sinusoidal waves supplied as bias voltage to the parasitic elements. The frequency of the sinusoidal waves is the same as the OFDM subcarrier frequency spacing f_s. Figure 3.2 also presents the equivalent baseband model of the ESPAR antenna. Due to the effect of electrical coupling between the antenna elements, the total received signal is the sum of the signals received in the radiator and parasitic elements. Considering an ideal design of the ESPAR antenna, the effect of the sinusoidal waves connected to the parasitic elements is equivalent to multiplying the signals received in the parasitics elements (#1, #2) with the exponential functions $e^{j2\pi f_s t}$ and $e^{-j2\pi f_s t}$, respectively; where $j = \sqrt{-1}$ is the imaginary unit. Therefore, the baseband representation of the received signal at the output of the RF front-end is modeled as

$$v(t) = v_0(t) + e^{j2\pi f_s t} v_1(t) + e^{-j2\pi f_s t} v_2(t), \tag{3.1}$$

where $v_0(t)$ is the signal received by the radiator element and $v_1(t)$, $v_2(t)$ are the signals received by the parasitic elements.

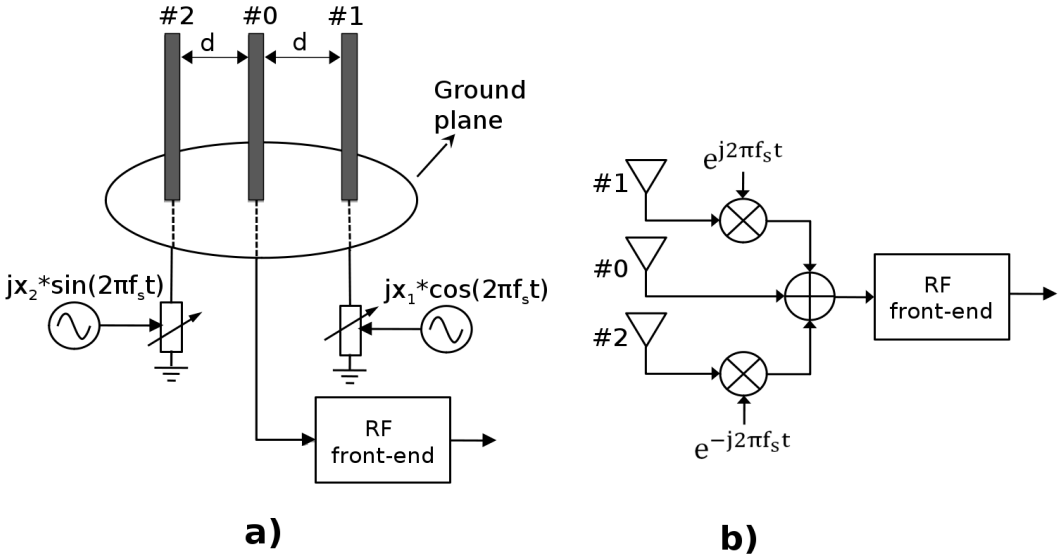

Figure 3.2: 3-element ESPAR antenna with periodically alternating directivity. a) Physical model, b) equivalent baseband model.

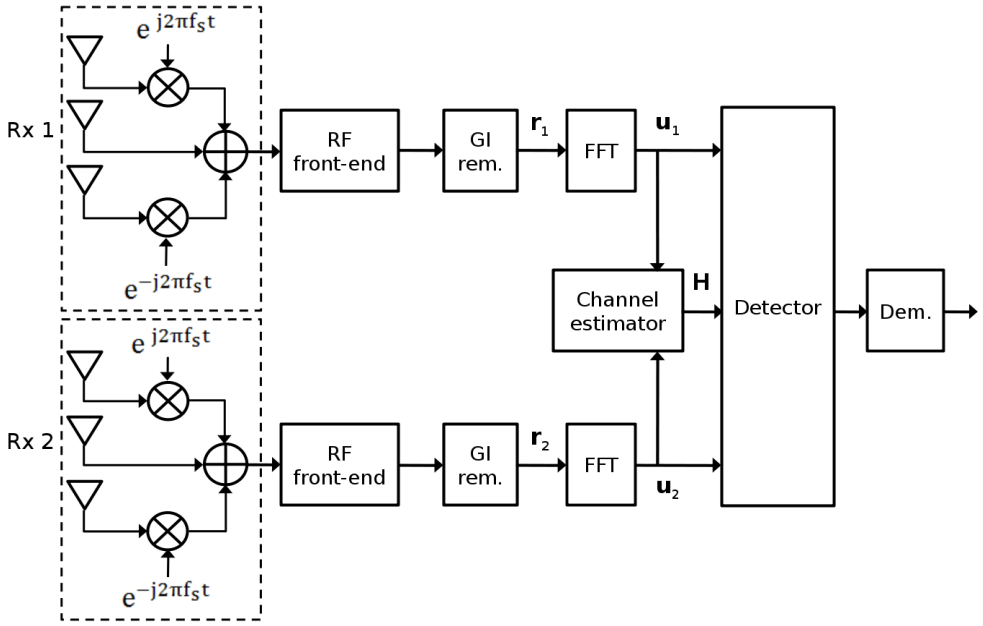

Figure 3.3: Block diagram of the MIMO-OFDM receiver with 3-element ESPAR antenna.

The block diagram of the receiver is shown in Fig. 3.3. While each transmitter uses a conventional antenna, every receiver uses the 3-element ESPAR antenna with periodic alternating directivity. In every receiver, after the RF front-end the GI is removed from the signal. Then, the FFT block obtains the frequency domain equivalent of the signal which is fed to the channel estimator and detector. The channel estimator obtains the CSI and with it the detector can determine the transmitted symbols. Finally, the demodulator outputs the transmitted data.

For deriving the signal model, let us denote the vector of transmitted symbols in frequency domain as

$$\mathbf{x}_i = [x_0^{(i)}, x_1^{(i)}, \ldots, x_{N-1}^{(i)}]^T, \tag{3.2}$$

where $x_k^{(i)}$ is the transmitted symbol at the k-th subcarrier for the i-th transmitter, N is the FFT window size, and $(\cdot)^T$ represents the transpose of that vector. The transmitted signal in time domain at the output of the IFFT block for the i-th transmitter is given by

$$\mathbf{v}_i = \mathbf{F}^H \mathbf{x}_i, \tag{3.3}$$

where $\mathbf{F}$ is the Fourier transform matrix and $(\cdot)^H$ represents the Hermitian transpose of that matrix. The matrix element $F_{l,m}$ corresponding to the l-th row and m-th column of $\mathbf{F}$ is given by

$$F_{l,m} = \frac{1}{\sqrt{N}} e^{-j\frac{2\pi lm}{N}}. \qquad \begin{matrix} 0 \leq l \leq N-1 \\ 0 \leq m \leq N-1 \end{matrix} \tag{3.4}$$

To mitigate the ISI, a guard interval consisting of a cyclic prefix (CP) of length N_{GI} is inserted in front of every OFDM symbol before it is transmitted.

The model is a 2×2 MIMO-OFDM system; hence, each receiver has signals transmitted from both antennas. From Eq. (3.1) and considering that the signals received by each element of the ESPAR antenna have independent fading, the vector of received symbols at the i-th receiver after the GI is removed is given by

$$\begin{aligned} \mathbf{r}_i = &\left(\mathbf{C}_{i,1}^{(0)} + \mathbf{D}_1\mathbf{C}_{i,1}^{(1)} + \mathbf{D}_2\mathbf{C}_{i,1}^{(2)}\right)\mathbf{v}_1 \\ &+ \left(\mathbf{C}_{i,2}^{(0)} + \mathbf{D}_1\mathbf{C}_{i,2}^{(1)} + \mathbf{D}_2\mathbf{C}_{i,2}^{(2)}\right)\mathbf{v}_2 + \mathbf{z}_i, \end{aligned} \tag{3.5}$$

where $\mathbf{C}_{i,l}^{(k)}$ is the channel impulse response matrix between the i-th receiving and l-th transmitting antenna for the $\#k$-th element of the ESPAR antenna. The vector $\mathbf{z}_i$ is the AWGN noise vector. The matrices $\mathbf{D}_1$ and $\mathbf{D}_2$ are diagonal matrices whose k-th diagonal element is given by

$$d_{(1)}^{k} = e^{j\frac{2\pi k}{N}} \tag{3.6}$$

and

$$d_{(2)}^{k} = e^{-j\frac{2\pi k}{N}}, \tag{3.7}$$

respectively. The vector of received symbols at the i-th receiver and after the FFT block is given by

$$\begin{aligned}\mathbf{u}_i = &\left(\mathbf{H}_{i,1}^{(0)} + \mathbf{G}_1\mathbf{H}_{i,1}^{(1)} + \mathbf{G}_2\mathbf{H}_{i,1}^{(2)}\right)\mathbf{x}_1 \\ &+ \left(\mathbf{H}_{i,2}^{(0)} + \mathbf{G}_1\mathbf{H}_{i,2}^{(1)} + \mathbf{G}_2\mathbf{H}_{i,2}^{(2)}\right)\mathbf{x}_2 + \boldsymbol{\zeta}_i,\end{aligned} \tag{3.8}$$

where $\mathbf{H}_{i,l}^{(k)}$ is the channel frequency response matrix between the i-th receiving and l-th transmitting antenna for the $\#k$-th element of the ESPAR antenna and it is defined as

$$\mathbf{H}_{i,l}^{(k)} = \mathbf{F}\mathbf{C}_{i,l}^{(k)}\mathbf{F}^{H}. \tag{3.9}$$

The vector $\boldsymbol{\zeta}_i$ is the noise in frequency domain for the i-th receiver. The matrices $\mathbf{G}_1$ and $\mathbf{G}_2$ are the frequency domain equivalents of $\mathbf{D}_1$ and $\mathbf{D}_2$, respectively. The matrices $\mathbf{G}_1$ and $\mathbf{G}_2$ are composed of a diagonal of ones elements that is shifted upwards and downwards, respectively. These matrices introduce a negative and positive frequency-shift effect in the components of the channel frequency response, and they can be expressed as

$$\mathbf{G}_1 = \begin{pmatrix} 0 & 0 & \dots & 0 & 1 \\ 1 & 0 & \ddots & \vdots & 0 \\ 0 & 1 & \ddots & \vdots & \vdots \\ \vdots & \ddots & \ddots & 0 & \vdots \\ 0 & \dots & 0 & 1 & 0 \end{pmatrix} \tag{3.10}$$

and

$$\mathbf{G}_2 = \begin{pmatrix} 0 & 1 & 0 & \dots & 0 \\ 0 & 0 & 1 & \ddots & \vdots \\ \vdots & \vdots & 0 & \ddots & 0 \\ 0 & \vdots & \vdots & \ddots & 1 \\ 1 & 0 & 0 & \dots & 0 \end{pmatrix}. \tag{3.11}$$

Equation (3.8) can also be expressed as

$$\mathbf{u}_i = \mathbf{H}_{i,A}\mathbf{x}_1 + \mathbf{H}_{i,B}\mathbf{x}_2 + \boldsymbol{\zeta}_i, \tag{3.12}$$

where $\mathbf{H}_{i,A}$, $\mathbf{H}_{i,B}$ are defined by

$$\mathbf{H}_{i,A} = \mathbf{H}_{i,1}^{(0)} + \mathbf{G}_1\mathbf{H}_{i,1}^{(1)} + \mathbf{G}_2\mathbf{H}_{i,1}^{(2)} \tag{3.13}$$

and

$$\mathbf{H}_{i,B} = \mathbf{H}_{i,2}^{(0)} + \mathbf{G}_1\mathbf{H}_{i,2}^{(1)} + \mathbf{G}_2\mathbf{H}_{i,2}^{(2)}. \tag{3.14}$$

Equation (3.12) can also be expressed in matrix form by

$$\begin{bmatrix} \mathbf{u}_1 \\ \mathbf{u}_2 \end{bmatrix} = \begin{bmatrix} \mathbf{H}_{1,A} & \mathbf{H}_{1,B} \\ \mathbf{H}_{2,A} & \mathbf{H}_{2,B} \end{bmatrix} \begin{bmatrix} \mathbf{x}_1 \\ \mathbf{x}_2 \end{bmatrix} + \begin{bmatrix} \boldsymbol{\zeta}_1 \\ \boldsymbol{\zeta}_2 \end{bmatrix}. \tag{3.15}$$

Consequently, the channel frequency response matrix $\mathbf{H}$ for the MIMO-OFDM receiver with ESPAR antenna is given by

$$\mathbf{H} = \begin{bmatrix} \mathbf{H}_{1,A} & \mathbf{H}_{1,B} \\ \mathbf{H}_{2,A} & \mathbf{H}_{2,B} \end{bmatrix}, \tag{3.16}$$

and its structure is presented in Eq. (3.17).

$$\mathbf{H} = \begin{pmatrix}
H_{1,1}^{(0)}(0) & H_{1,1}^{(2)}(1) & 0 & \dots & 0 & H_{1,1}^{(1)}(N-1) & H_{1,2}^{(0)}(0) & H_{1,2}^{(2)}(1) & 0 & \dots & 0 & H_{1,2}^{(1)}(N-1) \\
H_{1,1}^{(1)}(0) & H_{1,1}^{(0)}(1) & \ddots & \ddots & \ddots & 0 & H_{1,2}^{(1)}(0) & H_{1,2}^{(0)}(1) & \ddots & \ddots & \ddots & 0 \\
0 & H_{1,1}^{(1)}(1) & \ddots & \ddots & \ddots & \vdots & 0 & H_{1,2}^{(1)}(1) & \ddots & \ddots & \ddots & \vdots \\
\vdots & \dots & \ddots & \ddots & H_{1,1}^{(2)}(N-2) & 0 & \vdots & \dots & \ddots & \ddots & H_{1,2}^{(2)}(N-2) & 0 \\
0 & \ddots & \ddots & \ddots & H_{1,1}^{(0)}(N-2) & H_{1,1}^{(2)}(N-1) & 0 & \ddots & \ddots & \ddots & H_{1,2}^{(0)}(N-2) & H_{1,2}^{(2)}(N-1) \\
H_{1,1}^{(2)}(0) & 0 & \dots & 0 & H_{1,1}^{(1)}(N-2) & H_{1,1}^{(0)}(N-1) & H_{1,2}^{(2)}(0) & 0 & \dots & 0 & H_{1,2}^{(1)}(N-2) & H_{1,2}^{(0)}(N-1) \\
H_{2,1}^{(0)}(0) & H_{2,1}^{(2)}(1) & 0 & \dots & 0 & H_{2,1}^{(1)}(N-1) & H_{2,2}^{(0)}(0) & H_{2,2}^{(2)}(1) & 0 & \dots & 0 & H_{2,2}^{(1)}(N-1) \\
H_{2,1}^{(1)}(0) & H_{2,1}^{(0)}(1) & \ddots & \ddots & \ddots & 0 & H_{2,2}^{(1)}(0) & H_{2,2}^{(0)}(1) & \ddots & \ddots & \ddots & 0 \\
0 & H_{2,1}^{(1)}(1) & \ddots & \ddots & \ddots & \vdots & 0 & H_{2,2}^{(1)}(1) & \ddots & \ddots & \ddots & \vdots \\
\vdots & \dots & \ddots & \ddots & H_{2,1}^{(2)}(N-2) & 0 & \vdots & \dots & \ddots & \ddots & H_{2,2}^{(2)}(N-2) & 0 \\
0 & \ddots & \ddots & \ddots & H_{2,1}^{(0)}(N-2) & H_{2,1}^{(2)}(N-1) & 0 & \ddots & \ddots & \ddots & H_{2,2}^{(0)}(N-2) & H_{2,2}^{(2)}(N-1) \\
H_{2,1}^{(2)}(0) & 0 & \dots & 0 & H_{2,1}^{(1)}(N-2) & H_{2,1}^{(0)}(N-1) & H_{2,2}^{(2)}(0) & 0 & \dots & 0 & H_{2,2}^{(1)}(N-2) & H_{2,2}^{(0)}(N-1)
\end{pmatrix} \tag{3.17}$$

3.3 Channel Estimator

The channel estimation is possible due to the transmission of symbols, which are known as pilots, that are known in the transmitter and receiver. The WLAN IEEE 802.11n standard [9] is considered; hence, a block-type pilot pattern is used. This means that at the beginning of every packet an OFDM symbol, which is composed of pilots in all subcarriers, is transmitted. Let $\mathbf{p}_1$ be the pilot symbol vector in frequency domain which is transmitted by the first transmitter and uses a high throughput-long training field (HT-LTF) pattern. Vector $\mathbf{p}_2$ is the pilot symbol in frequency domain that is transmitted by the second transmitter. The pattern of $\mathbf{p}_2$ is the same as $\mathbf{p}_1$ but using a cyclic shift delay (CSD). When the pilot symbols are transmitted, Eq. (3.8) can be expressed as

$$\begin{aligned}\mathbf{u}_i = &\mathbf{P}_1\mathbf{h}_{i,1}^{(0)} + \mathbf{G}_1\mathbf{P}_1\mathbf{h}_{i,1}^{(1)} + \mathbf{G}_2\mathbf{P}_1\mathbf{h}_{i,1}^{(2)} \\ &+ \mathbf{P}_2\mathbf{h}_{i,2}^{(0)} + \mathbf{G}_1\mathbf{P}_2\mathbf{h}_{i,2}^{(1)} + \mathbf{G}_2\mathbf{P}_2\mathbf{h}_{i,2}^{(2)} + \boldsymbol{\zeta}_i,\end{aligned} \tag{3.18}$$

where $\mathbf{h}_{i,l}^{(k)}$ is a vector with the diagonal elements of $\mathbf{H}_{i,l}^{(k)}$. The matrices $\mathbf{P}_1$ and $\mathbf{P}_2$ are diagonal matrices whose diagonal elements are the pilot vectors $\mathbf{p}_1$ and $\mathbf{p}_2$, respectively

3.3.1 MMSE Channel Estimation

The MMSE channel estimator is an extension of the estimator designed for the OFDM receiver with ESPAR antenna presented in [12]. From Eq. (3.18), the auto-correlation matrix $\mathbf{R}_u$=E[$\mathbf{u}_i\mathbf{u}_i^H$] is given by

$$\begin{aligned}\mathbf{R_u} = \mathbf{P}_1\mathbf{R}_h\mathbf{P}_1^H + \mathbf{G}_1\mathbf{P}_1\mathbf{R}_h\mathbf{P}_1^H\mathbf{G}_1^H + \mathbf{G}_2\mathbf{P}_1\mathbf{R}_h\mathbf{P}_1^H\mathbf{G}_2^H \\ + \mathbf{P}_2\mathbf{R}_h\mathbf{P}_2^H + \mathbf{G}_1\mathbf{P}_2\mathbf{R}_h\mathbf{P}_2^H\mathbf{G}_1^H + \mathbf{G}_2\mathbf{P}_2\mathbf{R}_h\mathbf{P}_2^H\mathbf{G}_2^H + \sigma_\zeta^2\mathbf{I},\end{aligned} \tag{3.19}$$

where σ_ζ^2 is the noise variance and $\mathbf{R}_h$ is the covariance matrix that is modeled as an exponential decaying filter which is given by

$$\mathbf{R}_h(l,k) = \frac{1}{1 + j2\pi f_s(l-k)\tau}, \tag{3.20}$$

where f_s is the subcarrier frequency spacing and τ is the root mean squared delay of the channel.

The cross-correlation matrices $\mathbf{B}_i$=E[$\mathbf{uh}^H$] are given by

$$\mathbf{B}_i^{(0)} = \mathbf{P}_i\mathbf{R}_h, \tag{3.21}$$

$$\mathbf{B}_i^{(1)} = \mathbf{G}_1\mathbf{P}_i\mathbf{R}_h, \tag{3.22}$$

and

$$\mathbf{B}_i^{(2)} = \mathbf{G}_2\mathbf{P}_i\mathbf{R}_h. \tag{3.23}$$

Finally, the estimated channel responses between the i-th receiving antenna and l-th transmitting antenna are given by

$$\widetilde{\mathbf{h}}_{i,l}^{(0)} = (\mathbf{R_u}^{-1}\mathbf{B}_i^{(0)})^H\mathbf{u}_l, \tag{3.24}$$

$$\widetilde{\mathbf{h}}_{i,l}^{(1)} = (\mathbf{R_u}^{-1}\mathbf{B}_i^{(1)})^H\mathbf{u}_l, \tag{3.25}$$

and

$$\widetilde{\mathbf{h}}_{i,l}^{(2)} = (\mathbf{R_u}^{-1}\mathbf{B}_i^{(2)})^H\mathbf{u}_l. \tag{3.26}$$

Obtaining the estimated channel responses requires a matrix inverse calculation and several matrix by matrix multiplications that have high computational cost. Therefore, this becomes a drawback of the MMSE channel estimator.

3.3.2 CS-Based Channel Estimation

Some recent studies have shown that the CIR is sparse. This means that only few of its components are zero or under the noise floor so they can be considered as zero. For this reason, CS-based channel estimation has been proposed for MIMO-OFDM systems [55, 56]. Equation (3.18) showed that is necessary to estimate six channel frequency responses $\left(\mathbf{h}_{i,1}^{(0)}, \mathbf{h}_{i,1}^{(1)}, \mathbf{h}_{i,1}^{(2)}, \mathbf{h}_{i,2}^{(0)}, \mathbf{h}_{i,2}^{(1)}, \mathbf{h}_{i,2}^{(2)}\right)$ in the i-th receiver. This is three times bigger compared to what is required by conventional MIMO-OFDM systems. One option would be to increase the number of pilot symbols; however, this would reduce the spectral efficiency. Consequently, the challenges are to perform the channel estimation without increasing the number of pilots and at the same time having good accuracy and low complexity.

Due to the sparse nature of the CIR, the channel can be estimated using the CS methodology. First, the received signal has to be expressed similarly to the linear measurement model given by

$$\mathbf{r} = \boldsymbol{\Psi}\boldsymbol{\theta} + \boldsymbol{\eta}, \tag{3.27}$$

where $\mathbf{r}$ is an n-size vector of observations, $\boldsymbol{\Psi}$ is an $n \times m$ measurement matrix with $n<m$, $\boldsymbol{\theta}$ is a m-size unknown S-sparse vector with S non-zero elements, and $\boldsymbol{\eta}$ is the noise vector.

Let N_p define the number of pilot subcarriers and $\boldsymbol{\rho}$ the index vector containing the pilot positions as $\boldsymbol{\rho} = [\rho_1, \rho_2, \ldots, \rho_{N_p}]$. The vector of received pilot symbols at the i-th receiver is given by

$$\mathbf{a}_i = [u_i(\rho_1), u_i(\rho_2), \cdots, u_i(\rho_{N_p})], \tag{3.28}$$

where $u_i(k)$ is the received signal at the k-th subcarrier of the i-th receiver. The N_p-size vector $\mathbf{a}_i$ becomes the vector of observations.

The measurement matrix is obtained from the union of six submatrices and it is defined by

$$\boldsymbol{\Psi} = [\mathbf{P}_1\mathbf{F}_L, \mathbf{G}_1\mathbf{P}_1\mathbf{F}_L, \mathbf{G}_2\mathbf{P}_1\mathbf{F}_L, \mathbf{P}_2\mathbf{F}_L, \mathbf{G}_1\mathbf{P}_2\mathbf{F}_L, \mathbf{G}_2\mathbf{P}_2\mathbf{F}_L], \tag{3.29}$$

where $\mathbf{F}_L$ is an $N_p \times L$ matrix built with parts of the Fourier transform matrix

and it is given by

$$\mathbf{F}_L = \frac{1}{\sqrt{N}} \begin{bmatrix} 1 & \omega^{\rho_1} & \dots & \omega^{\rho_1(L-1)} \\ 1 & \omega^{\rho_2} & \dots & \omega^{\rho_2(L-1)} \\ \vdots & \vdots & \dots & \vdots \\ 1 & \omega^{\rho_{N_p}} & \dots & \omega^{\rho_{N_p}(L-1)} \end{bmatrix}, \tag{3.30}$$

where $\omega = e^{-j2\pi/N}$ and L is equivalent to the GI size N_{GI}. In the resulting $N_p \times 6L$ measurement matrix Ψ, the number of rows is less than the columns ($N_p < 6L$) so it is an under-determined system.

The unknown vector $\boldsymbol{\theta}_i$ at the i-th receiver is obtained from the union of six subvectors and it is given by

$$\boldsymbol{\theta}_i = [\mathbf{c}_{i,1}^{(0)}, \mathbf{c}_{i,1}^{(1)}, \mathbf{c}_{i,1}^{(2)}, \mathbf{c}_{i,2}^{(0)}, \mathbf{c}_{i,2}^{(1)}, \mathbf{c}_{i,2}^{(2)}]^T, \tag{3.31}$$

where $\mathbf{c}_{i,1}^{(0)}, \mathbf{c}_{i,1}^{(1)}, \mathbf{c}_{i,1}^{(2)}, \mathbf{c}_{i,2}^{(0)}, \mathbf{c}_{i,2}^{(1)}$, and $\mathbf{c}_{i,2}^{(2)}$ are row subvectors of length L containing part of the CIR of the components of the signal generated by the MIMO-OFDM receiver with ESPAR antenna.

The system that has to be solved for the i-th receiver using the CS methodology is given by

$$\mathbf{a}_i = \boldsymbol{\Psi}\boldsymbol{\theta}_i + \boldsymbol{\eta}. \tag{3.32}$$

The answer to this system can be obtained using any of the CS recovery algorithms, but greedy algorithms are more appealing due to its low computational cost. The output of the recovery algorithm is the estimated vector $\tilde{\boldsymbol{\theta}}_i$ which is given by

$$\tilde{\boldsymbol{\theta}}_i = [\tilde{\mathbf{c}}_{i,1}^{(0)}, \tilde{\mathbf{c}}_{i,1}^{(1)}, \tilde{\mathbf{c}}_{i,1}^{(2)}, \tilde{\mathbf{c}}_{i,2}^{(0)}, \tilde{\mathbf{c}}_{i,2}^{(1)}, \tilde{\mathbf{c}}_{i,2}^{(2)}]^T. \tag{3.33}$$

Finally, the estimated channel responses between the i-th receiving antenna and l-th transmitting antenna are given by

$$\widetilde{\mathbf{h}}_{i,l}^{(0)} = \mathbf{F}_L \left(\tilde{\mathbf{c}}_{i,l}^{(0)}\right)^T, \tag{3.34}$$

$$\widetilde{\mathbf{h}}_{i,l}^{(1)} = \mathbf{F}_L \left(\tilde{\mathbf{c}}_{i,l}^{(1)}\right)^T, \tag{3.35}$$

and

$$\widetilde{\mathbf{h}}_{i,l}^{(2)} = \mathbf{F}_L \left(\tilde{\mathbf{c}}_{i,l}^{(2)}\right)^T. \tag{3.36}$$

Modified-OMP

The sparse vector $\boldsymbol{\theta}_i$ has more non-zero components compared to conventional MIMO-OFDM systems. This causes an increase in the computational cost required by the recovery algorithm and also reduces the recovery accuracy of the positions of the non-zero elements. The separation between the three elements of the ESPAR antenna is small so the delay positions in the CIR can be considered the same for the three antenna elements. This assumption can be exploited to reduce the computational cost required by the recovery algorithm and it is applied into the OMP algorithm. The resulting algorithm is called *modified-OMP*.

The main differences between the proposed modified-OMP algorithm and OMP are: the number of iterations, the number of columns that are selected in each iteration, and how these columns are selected. The pseudocode of the proposed modified-OMP is presented in Algorithm 3.1. To obtain the most correlated column with the residual, first the vector $\mathbf{proj}{:=}\ |\boldsymbol{\Psi}^H\mathbf{r}_{t-1}|$ is obtained. This vector is affected by the noise present in the vector of observations, but is also the union of six subvectors of size L that have the maximum values in similar positions. Therefore, these six subvectors can be summed to improve the accuracy of the algorithm. The *for* loop in lines (9-11) obtains the sum of the six subvectors. Then, the index ω of the element in vector **sum** with maximum value is obtained. The next *for* loop in lines (14-18) replicates the index ω into the other six subvectors and builds an index set Ω with these indices. Additionally, a matrix $\mathbf{E}$ is built with the columns of $\boldsymbol{\Psi}$ corresponding to these indices. The set Ω is added to the index set Λ_t and also $\mathbf{E}$ is added to $\boldsymbol{\Phi}_t$. Then, like in OMP, the new estimated signal is obtained by solving the least squares problem of line (21). The next step is to update the residual and the procedure continues for the next iteration.

While the conventional OMP algorithm selects one new column in each iteration, our proposed modification selects six columns. Therefore, the number of total iterations is divided by six and the required computational cost is reduced. Additionally, by using the sum of the six subvectors to obtain the most correlated column, the algorithm improves the recovery accuracy.

Algorithm 3.1 Modified-OMP

Input: $\mathbf{a}$ (n-size vector of observations for the i-th receiver)
Input: $\mathbf{\Psi}$ ($n \times m$ measurement matrix)
Input: S (sparsity level)
Input: L
$\mathbf{r}_0 := \mathbf{a}$, $\Lambda_0 := \emptyset$, $\mathbf{\Phi}_0 := [\ ]$
for $t = 1, \ldots, (S/6)$ **do**
    proj:= $|\mathbf{\Psi}^H \mathbf{r}_{t-1}|$
    sum:= **0**
    for $i = 0, \ldots, 5$ **do**
        sum := **sum** + **proj**$(i * L : (i+1)L - 1)$
    end for
    ω :=arg $\max_{j=1,\ldots,L}$(**sum**)
    $\Omega := \emptyset, \mathbf{E} := [\ ]$
    for $i = 0, \ldots, 5$ **do**
        $tmp := \omega + i * L$
        $\Omega := \Omega \cup \{tmp\}$
        $\mathbf{E} := [\mathbf{E}\ \ \boldsymbol{\psi}_{tmp}]$
    end for
    $\Lambda_t := \Lambda_{t-1} \cup \Omega$
    $\mathbf{\Phi}_t := [\mathbf{\Phi}_{t-1}\ \ \mathbf{E}]$
    $\mathbf{y}_t$:=arg $\min_y \|\mathbf{a} - \mathbf{\Phi}_t \mathbf{y}\|_2^2$
    $\mathbf{r}_t := \mathbf{a} - \mathbf{\Phi}_t \mathbf{y}_t$
end for
Output: $\tilde{\boldsymbol{\theta}}$ (composed of $\mathbf{y}_t$ values at Λ_t positions)

3.3.3 Computational Complexity

In this section the computational complexity of the MMSE and CS-based channel estimators is derived. In the case of the MMSE channel estimator, it requires the calculation of the matrix inverse, 12 matrix by matrix multiplications, and 12 matrix by vector multiplications. Therefore, its total complexity can be expressed as

$$C_{MMSE} = O(14N_p^3) + O(12N_p^2), \tag{3.37}$$

where N_p is the number of pilot subcarriers.

According to [45], in terms of complexity the dominant step in the OMP algorithm is to find the column that is most correlated with the residual. Therefore, the computational complexity of OMP is in the order of $O(Snm)$ for an $n \times m$ measurement matrix and sparse vector with S non-zero elements. In the proposed modified-OMP algorithm, the number of total required iterations is divided by six and the size of the measurement matrix is $N_p \times 6L$. Consequently, the complexity of the modified-OMP algorithm is in the order of $O(SN_pL)$. For calculating the channel frequency response, the CS-based channel estimation requires 12 matrix by vector multiplications. Therefore, considering the two receivers, the total computational complexity of the proposed CS-based calculation can be expressed as

$$C_{CS} = O(2SN_pL) + O(12N_pL). \tag{3.38}$$

Considering that L is a fraction of the number of pilot subcarriers N_p and that the sparsity S is a small number, the CS-based channel estimation has a computational complexity that is roughly around N_p-times smaller compared with that of the MMSE channel estimator.

3.4 Detector

3.4.1 MMSE Sparse-SQRD

In the proposed MIMO-OFDM receiver with 3-element ESPAR antenna, the detection cannot be performed in a per subcarrier fashion. The entire channel matrix has to be detected simultaneously and this implies a high computational cost. The MMSE sparse-SQRD algorithm is a low complexity detection scheme based on the MMSE-SQRD [58] algorithm. It is based on a QR decomposition of the channel matrix $\mathbf{H}$. Let us consider the communications system given by

$$\mathbf{u} = \mathbf{H}\mathbf{x} + \mathbf{z}, \tag{3.39}$$

where $\mathbf{u}$ is the vector of received symbols, $\mathbf{x}$ is the vector of transmitted symbols, and $\mathbf{z}$ is the noise vector. The extended channel matrix $\underline{\mathbf{H}}$ and extended vector

of received symbols are given by

$$\underline{\mathbf{H}} = \begin{bmatrix} \mathbf{H} \\ \sigma_z \mathbf{I}_{2N} \end{bmatrix}, \tag{3.40}$$

$$\underline{\mathbf{u}} = \begin{bmatrix} \mathbf{u} \\ \mathbf{0}_{2N,1} \end{bmatrix}, \tag{3.41}$$

where σ_z is the noise standard deviation, $\mathbf{I}_{2N}$ is a $2N \times 2N$ identity matrix, and $\mathbf{0}_{2N,1}$ is a $2N$-size column vector with zero elements. The QR decomposition of $\underline{\mathbf{H}}$ is given by

$$\underline{\mathbf{H}} = \underline{\mathbf{Q}}\underline{\mathbf{R}}, \tag{3.42}$$

where $\underline{\mathbf{Q}}$ is a unitary matrix and $\underline{\mathbf{R}}$ is an upper triangular matrix. Using Eq. (3.42), $\underline{\mathbf{u}}$ can be expressed as

$$\underline{\mathbf{u}} = \underline{\mathbf{Q}}\underline{\mathbf{R}}\mathbf{x} + \mathbf{z}, \tag{3.43}$$

and multiplying it by $\underline{\mathbf{Q}}^H$

$$\mathbf{y} = \underline{\mathbf{Q}}^H \underline{\mathbf{u}} = \underline{\mathbf{R}}\mathbf{x} + \underline{\mathbf{Q}}^H \mathbf{z}. \tag{3.44}$$

After the QR decomposition of $\underline{\mathbf{H}}$ is calculated, the transmitted signal is obtained using Eq. (3.44). In the MMSE-SQRD algorithm, the columns of $\underline{\mathbf{Q}}$ are sorted depending on its minimum norm.

The MMSE sparse-SQRD algorithm exploits the sparsity of the extended channel matrix $\underline{\mathbf{H}}$ to reduce the required computational cost for the detection. Its pseudocode is presented in Algorithm 3.2. The inputs of the algorithm are the extended channel matrix $\underline{\mathbf{H}}$ and the matrix **Hnz** which contains the indices of the initial positions of the non-zero elements. This information is used for the square norm calculation shown in lines (5-9) of the algorithm. The vector **nz**, which contains only the indices of the non-zero elements of the column $\underline{\mathbf{q}}_i$, is obtained in line (14). Using this vector, the reduced computation of $\underline{\mathbf{q}}_i$, $\underline{\mathrm{r}}_{i,l}$, $\underline{\mathbf{q}}_l$, $\mathbf{y}$ are shown in lines (15-17), (19-21), (23-25), and (29-34), respectively. The output of the algorithm is the estimated transmitted signal $\hat{\mathbf{x}}$ which is obtained in lines (36-40).

Algorithm 3.2 MMSE sparse-SQRD algorithm

Input: $\underline{\mathbf{H}}$, **Hnz**
$cols \leftarrow$ # of columns of $\underline{\mathbf{H}}$
$rows \leftarrow$ # of rows of $\underline{\mathbf{H}}$
$\underline{\mathbf{R}} = \mathbf{0}$, $\underline{\mathbf{Q}} = \underline{\mathbf{H}}$, $\mathbf{p} = (1,\ldots,\text{cols})$
for $i = 1, \ldots, cols$ **do**
  for $j = 1, \ldots, 5$ **do**
    $\mathbf{norm}(i) := \mathbf{norm}(i) + \|\underline{q}(Hnz(j,i),i)\|^2$
  end for
end for
for $i = 1, \ldots, cols$ **do**
  $k_i =$arg $\min_{l=i,\ldots,cols}\mathbf{norm}(l)$
  exchange columns i and k_i in $\underline{\mathbf{R}}$, $\underline{\mathbf{Q}}$, **norm**, **p**
  $\underline{r}(i,i) = \sqrt{\mathbf{norm}(i)}$
  nz $\leftarrow$ indices of the non-zero elements of $\underline{\mathbf{q}}_i$
  for $j = 1, \ldots, length(\mathbf{nz})$ **do**
    $\underline{q}(nz(j),i) := \underline{q}(nz(j),i)/\underline{r}(i,i)$
  end for
  for $l = i+1, \ldots, cols$ **do**
    for $j = 1, \ldots, length(\mathbf{nz})$ **do**
      $\underline{r}(i,l) := \underline{r}(i,l) + (\underline{q}^*(nz(j),i))\underline{q}(nz(j),l)$
    end for
    if $\|\underline{r}(i,l)\|^2 \neq 0$ **then**
      for $j = 1, \ldots, length(\mathbf{nz})$ **do**
        $\underline{q}(nz(j),l) := \underline{q}(nz(j),l) - \underline{r}(i,l)\underline{q}(nz(j),i)$
      end for
      $\mathbf{norm}(l) := \mathbf{norm}(l) - \|\underline{r}(i,l)\|^2$
    end if
  end for
  for $k = 1, \ldots, length(\mathbf{nz})$ **do**
    $\mathbf{y}(i) := \mathbf{y}(i) + (\underline{q}^*(nz(k),i))u(nz(k))$
    if $\mathbf{nz}(k) \geq (rows - cols)$ **then**
      break
    end if
  end for
end for
for $k = cols, \ldots, 1$ **do**
  $\hat{d} = \sum_{i=k+1}^{cols} \underline{r}(k,i)\hat{\mathbf{x}}(i)$
  $\hat{\mathbf{x}}(k) = \mathscr{Q}\left[(\mathbf{y}(k) - \hat{d})/\underline{r}(k,k)\right]$
end for
Permutate $\hat{\mathbf{x}}$ according to **p**

3.4.2 Submatrix Detection

The problem of detecting the transmitted symbols in MIMO-OFDM with ESPAR antenna is similar to the equalization of time-variant channels because in both cases there are multiple diagonals in the channel matrix. When the entire channel matrix is processed, it is called block equalization. The problem of block equalization is its high computational cost. There are several low complexity iterative techniques for equalization of time-variant channels such as serial [59] and decision-feedback equalizer (DFE) [60]. The serial equalizer iteratively selects one section of the channel matrix to detect one transmitted symbol. It is a fast algorithm but does not have a good accuracy. The DFE improves the accuracy by using the previous detected symbol to compensate the equalization of the next symbol. Its drawback is that is slower because it depends on the detection of the previous symbols. The advantage of the serial equalizer and DFE is the lower computational cost compared with block equalizers. On the other hand, the disadvantage is a degradation in the BER.

Some of the previously discussed features of iterative equalizers are combined to further reduce the computational cost of the detection of the MIMO-OFDM receiver with ESPAR antenna. A low complexity submatrix detection scheme, which is composed of eight MMSE sparse-SQRD detectors, is presented in Fig. 3.4. The submatrix builder block divides the channel matrix into eight smaller submatrices $\mathbf{J}_k (k = 1, \ldots, 8)$. Then, the k-th detector is fed with a subvector $\mathbf{s}_k$ of received symbols and the channel submatrix $\mathbf{J}_k$. The aim of this detection scheme is to reduce the computational cost but keeping a low detection time and minimizing the degradation in the BER. To obtain a low detection time, the detectors are divided into these two groups: (1,3,5,7) and (2,4,6,8). The four detectors of each group can operate in parallel to obtain a low detection time. The detected symbols obtained in detector 1, 3, 5, and 7 are used for compensating the received symbols that are fed to the other detectors. The objective of this feedback is to minimize the degradation in the BER; however, this implies that detectors 2, 4, 6, and 8 have to wait until the other detectors finished the detection process. Another strategy to reduce the degradation is an overlap between the subvectors and submatrices. These two features successfully reduce the degradation in the BER performance.

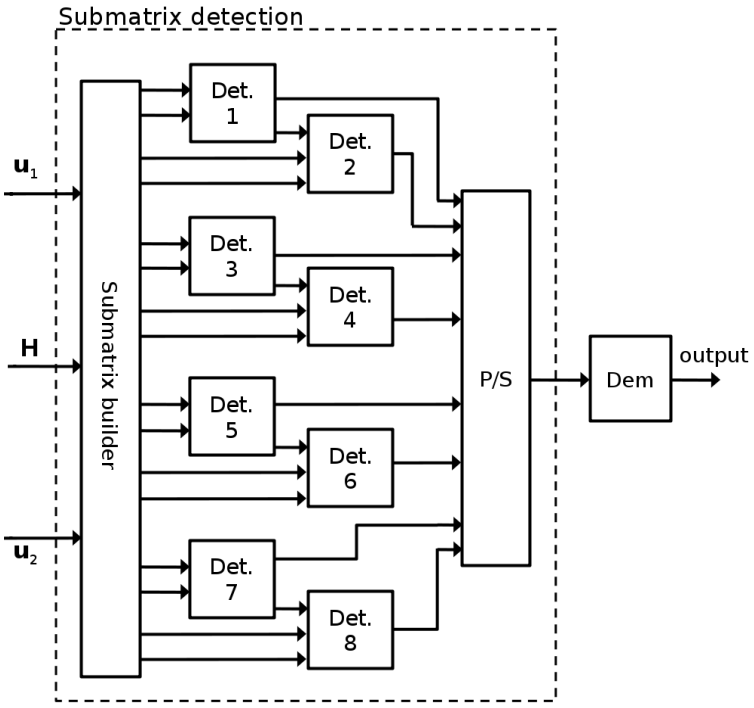

Figure 3.4: Block diagram of the submatrix detection.

Figure 3.5 presents a graphical representation of the procedure to obtain the submatrices and subvectors that are fed to the detectors. In the left, the vectors of received symbols $\mathbf{u}_1$ and $\mathbf{u}_2$, and the procedure to divide them into subvectors are presented. It can be seen that there is an overlap between $\mathbf{s}_{1,A}$ and $\mathbf{s}_{2,A}$, which means that both subvectors included the overlapped symbols to minimize the BER degradation. The structure of the channel matrix $\mathbf{H}$ is presented in the center of the figure. The non-zero elements in the diagonals are covered by several submatrices that also have overlapping elements. In the right, the subvector $\mathbf{s}_1$ is obtained by combining $\mathbf{s}_{1,A}$ and $\mathbf{s}_{1,B}$. The submatrix $\mathbf{J}_1$ is obtained from the combination of $\mathbf{J}_{1,A}$, $\mathbf{J}_{1,B}$, $\mathbf{J}_{1,C}$, and $\mathbf{J}_{1,D}$. Although not fully included in the figure, the other seven subvectors and submatrices are obtained in the same way.

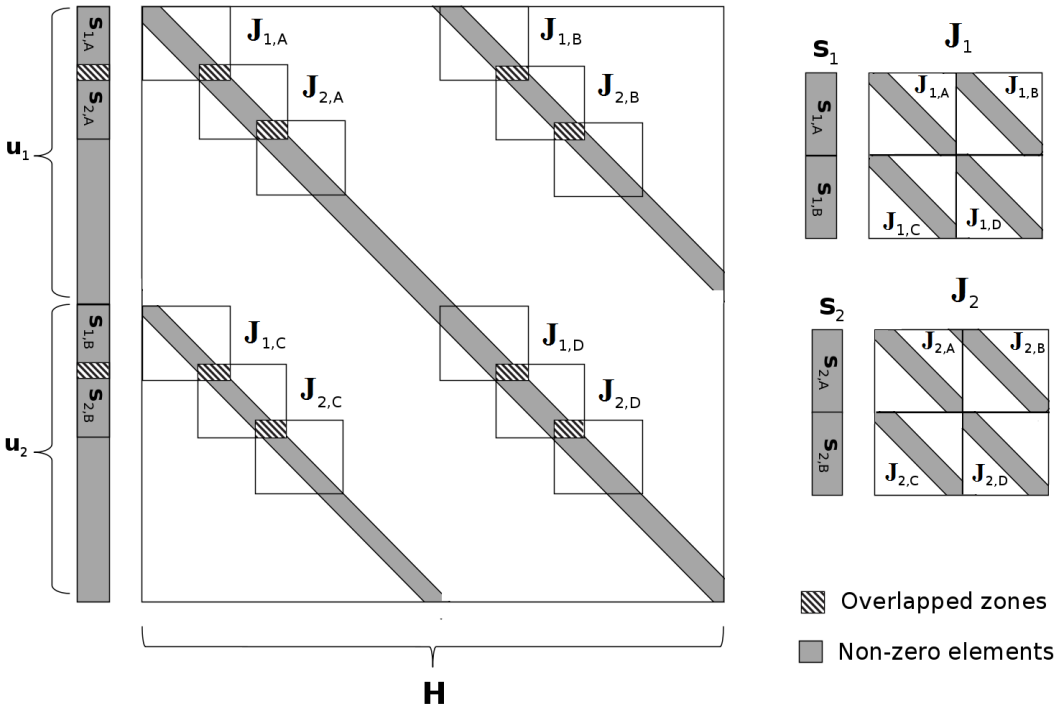

Figure 3.5: Graphical representation of the procedure to obtain the submatrices and subvectors.

3.5 Synchronization

Synchronization is an important step in an OFDM receiver and if not properly addressed, it can severely degrade the BER performance [61]. Its objectives are to determine the starting position of a frame and the carrier frequency offset (CFO) that is generated due to the mismatch between the oscillators in the transmitter and receiver. There are several methods for synchronization and they can use the received symbols in time or frequency domain. In an OFDM transmitter, a guard interval of size N_{GI} is added in the OFDM symbol to deal with the multipath channel. The guard interval is composed of a CP that is a copy of the tail of the OFDM symbol, and this feature is shown in Fig. 3.6. This similarity between the CP and tail of the OFDM symbol in time domain is used for low-complexity synchronization in [62, 63].

For applying this low complexity synchronization in the MIMO-OFDM re-

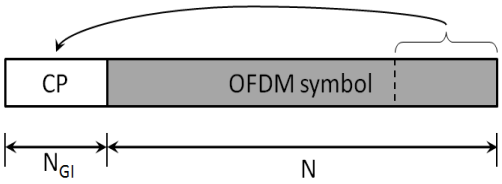

Figure 3.6: Relation between the OFDM symbol and cyclic prefix.

ceiver with ESPAR antenna, we need to show that the signal generated by the ESPAR antenna maintains the similarity between the CP and the tail of the OFDM symbol. For this purpose, the signal at the output of the ESPAR antenna, which was presented in Eq. (3.1), is expressed as

$$v(k) = v_0(k) + e^{j\frac{2\pi k}{N}} v_1(k) + e^{-j\frac{2\pi k}{N}} v_2(k), \tag{3.45}$$

where k is a discrete time index. The separation between elements in the CP and tail is equal to N; hence, if $v(k)$ represents an element in the CP, then the elements in the tail can be given by

$$v(k+N) = v_0(k+N) + e^{j\frac{2\pi(k+N)}{N}} v_1(k+N) + e^{-j\frac{2\pi(k+N)}{N}} v_2(k+N). \tag{3.46}$$

Considering a negligible channel effect and $k \in [-N_{GI}, -1]$, it can be assumed that

$$\begin{aligned} v_0(k+N) &= v_0(k) \\ v_1(k+N) &= v_1(k) \\ v_2(k+N) &= v_2(k). \end{aligned} \tag{3.47}$$

Then, replacing Eq. (3.47) into Eq. (3.46)

$$v(k+N) = v_0(k) + e^{j\frac{2\pi(k+N)}{N}} v_1(k) + e^{-j\frac{2\pi(k+N)}{N}} v_2(k), \tag{3.48}$$

and by solving Eq. (3.48), it is shown that

$$\begin{aligned} v(k+N) &= v_0(k) + e^{j\frac{2\pi k}{N}} e^{j2\pi} v_1(k) + e^{-j\frac{2\pi k)}{N}} e^{-j2\pi} v_2(k) \\ &= v_0(k) + e^{j\frac{2\pi k}{N}} v_1(k) + e^{-j\frac{2\pi k}{N}} v_2(k) \\ v(k+N) &= v(k). \end{aligned} \tag{3.49}$$

The result of Eq. (3.49) confirms the similarity between the CP and tail of the OFDM symbol when ESPAR antenna is used. Therefore, the synchronization techniques based on this feature can be also used in the MIMO-OFDM receiver.

Table 3.1: Simulation Settings

Modulation	QPSK, 16-QAM
Pilot type	Block-type
Pilot pattern	HT-LTF
Data subcarriers	52
FFT window size	64
GI	1/4
Noise type	AWGN
Fading	Frequency selective
Channel bandwidth	20MHz
Channel estimation	MMSE, CS-based
Detection	Block, submatrix detection
Channel model	4-ray exponential, 3GPP case B
Synchronization	Perfect

3.6 Simulation Results

A simulation model was implemented in c++ using it++ [64] communications library. In the simulation, the 2×2 MIMO-OFDM scheme using 3-element ESPAR antenna with periodically alternating directivity was implemented. The model is based on the transmitter and receiver schemes previously shown in Fig. 3.1 and 3.3, respectively. A summary of the simulation settings is shown in Table 3.1. To compare the performance in different channel scenarios, a 4-ray exponential channel and 3GPP case B [65] channel model were implemented. The power delay profiles of these channels are presented in Table 3.2 and 3.3, respectively.

In the simulation model, the pilot pattern is block-type and the pilot symbols $\mathbf{p}_1$ and $\mathbf{p}_2$ are composed of 56 pilot subcarriers. The vector $\mathbf{p}_2$ is a cyclic shifted version of $\mathbf{p}_1$ with a cyclic shift of 850 ns. For the CS-based channel estimation, L is equal to the GI size so ($L = 16$). Additionally, the OMP and modified-OMP CS-based recovery algorithms were implemented. For the detection, the block and submatrix detectors are employed.

First, a BER performance comparison of the MIMO-OFDM receiver with 3-element ESPAR antenna versus other conventional MIMO-OFDM schemes with-

Table 3.2: Power delay profile of 4-ray exponential channel

Tap index	Delay [ns]	Power [dB]
1	0	0
2	50	-3.0
3	100	-6.0
4	150	-9.0

Table 3.3: Power delay profile of 3GPP case B channel

Tap index	Delay [ns]	Power [dB]
1	0	0
2	110	-9.7
3	190	-19.2
4	410	-22.8

out ESPAR antenna is presented in Fig. 3.7. In this figure, perfect CSI and the 4-ray exponential channel are assumed. Compared to a conventional 2×2 MIMO-OFDM scheme (blue line), the MIMO-OFDM receiver with ESPAR antenna obtains a substantial improvement in the BER. For a BER of 10^{-3}, the diversity gain is about 14 dB. Additionally, the receiver obtains a BER close to the conventional 2×4 MIMO-OFDM scheme (red line) that has four RF chains. Therefore, the ESPAR antenna-based receiver is able to obtain diversity gain without additional RF chains.

3.6.1 Channel Estimation Performance

The BER, normalized mean square error (NMSE), and recovery accuracy of the CS algorithms were obtained to determine the performance of the proposed channel estimation schemes. The NMSE is defined as

$$NMSE = \frac{\sum_i |c_i - \tilde{c}_i|^2}{\sum_i |c_i|^2}, \tag{3.50}$$

where c_i is the i-th element of the CIR vector $\mathbf{c}$ and $\tilde{c}_i$ is the i-th element of the estimated CIR vector $\tilde{\mathbf{c}}$.

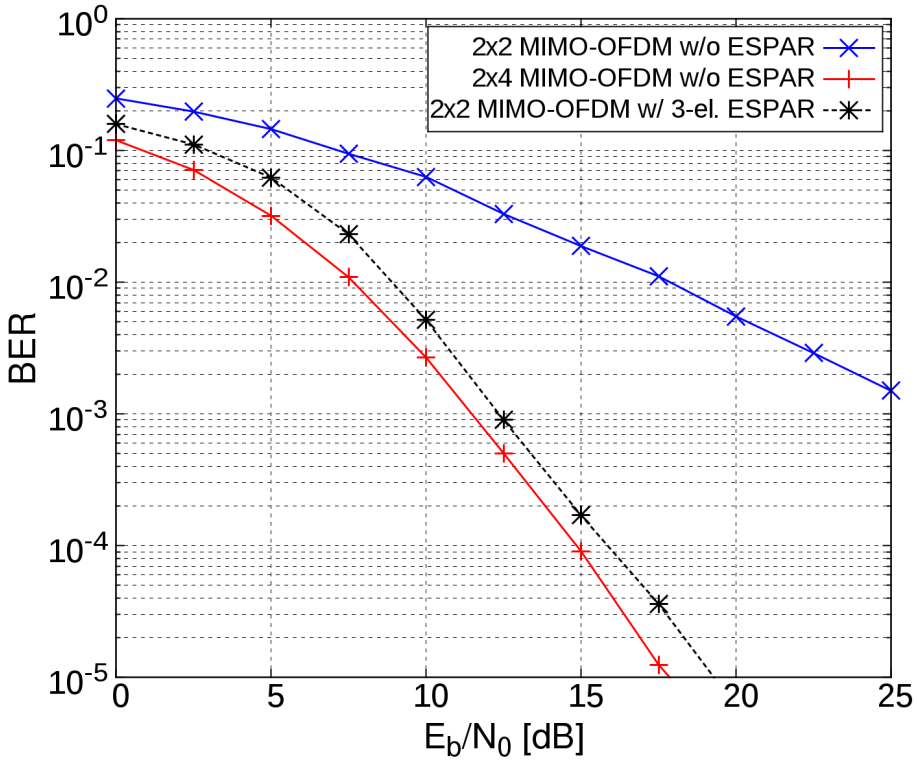

Figure 3.7: BER of the MIMO-OFDM receiver with ESPAR antenna (dashed line) versus other conventional MIMO-OFDM schemes without ESPAR antenna (solid line). Perfect CSI, 4-ray exponential channel, 16-QAM modulation, and block detection.

The BER performance of the MMSE and CS-based channel estimation schemes for the MIMO-OFDM receiver with ESPAR antenna is presented in Fig. 3.8 for the 3GPP case B channel. As reference, the BER with perfect CSI is included. For the CS-based channel estimation, it included the BER with OMP and modified-OMP. It can be observed that the CS-based channel estimation with modified-OMP obtains the best BER outperforming the OMP algorithm. The MMSE channel estimation has a bad BER and it is not suitable for this channel.

Similarly, the BER of the MMSE and CS-based channel estimation schemes for the the 4-ray exponential channel is presented in Fig. 3.9. In this figure, the CS-based channel estimation with modified-OMP also obtains the best BER performance and it is close to the BER with perfect CSI. The MMSE channel

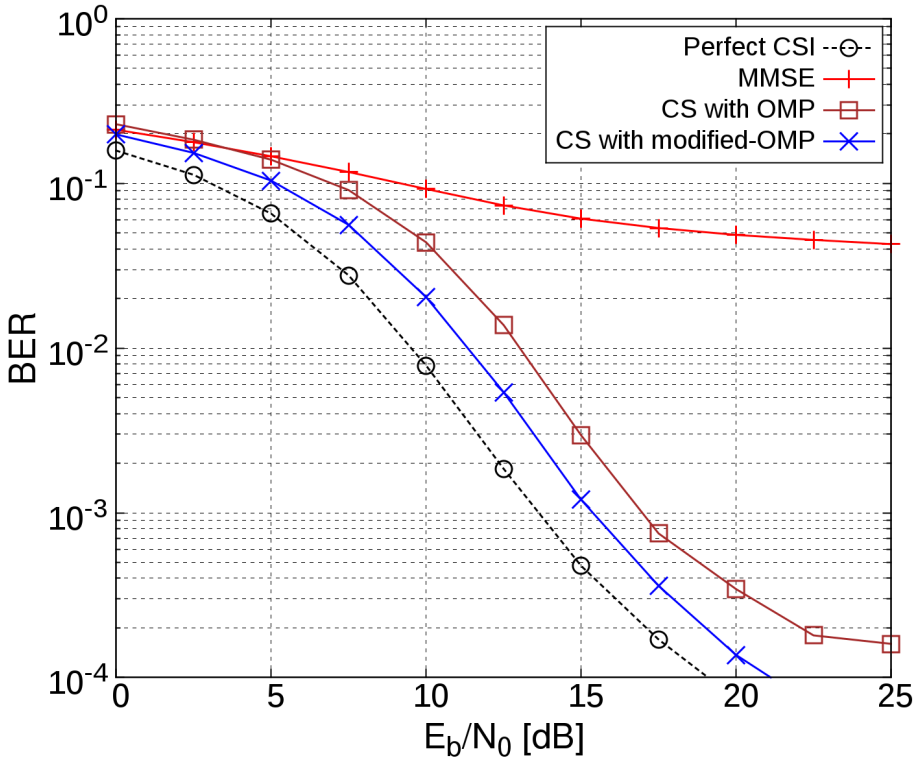

Figure 3.8: BER of the MMSE and CS-based channel estimation using the 3GPP case B channel, 16-QAM, and submatrix detection.

estimation obtains a better performance in the 4-ray exponential channel, but it is still not better than the CS-based channel estimation with modified-OMP algorithm.

For comparison, a lower bound of the NMSE is obtained for the CS-based channel estimation. This lower bound is based on an oracle estimator [66], which assumes that an oracle provides in advance the location of the non-zero elements of the CIR. Considering that the index vector λ_0 contains the location of the non-zero elements, the lower bound can be estimated from

$$\tilde{\mathbf{c}}_{oracle} = \left(\mathbf{\Psi}_{\lambda_0}^H \mathbf{\Psi}_{\lambda_0}\right)^{-1} \mathbf{\Psi}_{\lambda_0}^H \mathbf{u}, \tag{3.51}$$

where $\mathbf{\Psi}_{\lambda_0}$ is a submatrix constructed from the columns of the measurement matrix $\mathbf{\Psi}$ corresponding to the indices in λ_0.

Figure 3.10 shows the results of the NMSE of the channel estimation for the

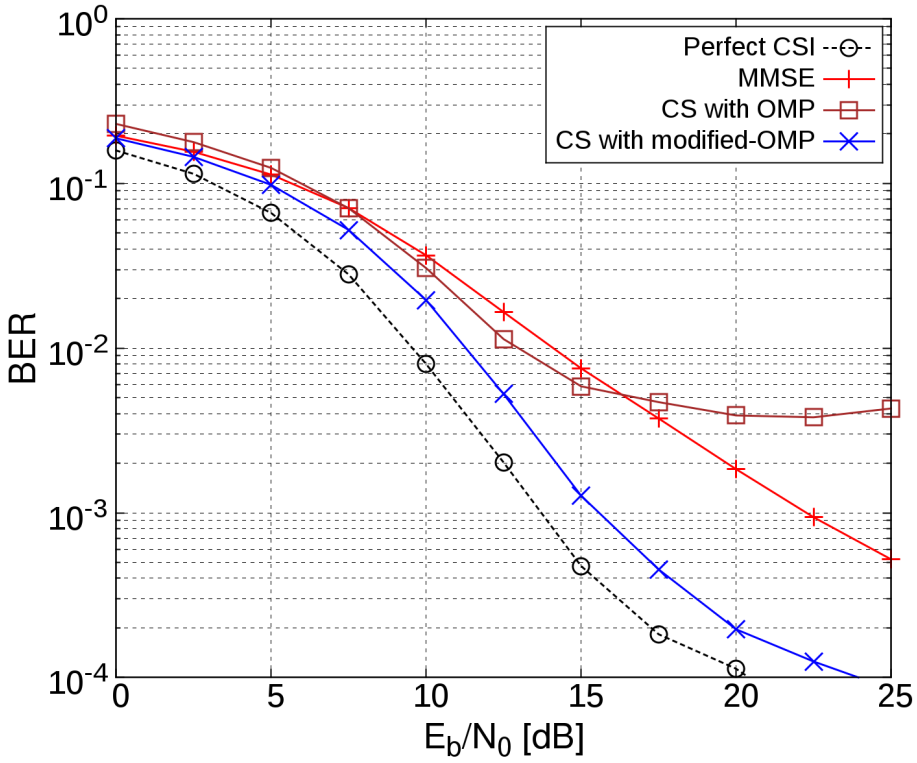

Figure 3.9: BER of the MMSE and CS-based channel estimation using 4-ray exponential channel, 16-QAM, and submatrix detection.

3GPP case B channel. For comparison, the NMSE of the lower bound when using an ideal oracle estimator is included. The NMSE of the MMSE channel estimation and CS-based based estimation with modified-OMP and conventional OMP are also included. The CS-based channel estimation with modified-OMP obtains smaller error than OMP and MMSE channel estimation. This figure shows that the NMSE of the MMSE channel estimation is also not good for the 3GPP channel. It can be seen that the gap between the lower bound and NMSE using modified-OMP decreases when the E_b/N_0 is increased. When $E_b/N_0 > 10$ dB, the gap is very small so the CS-based channel estimation with modified-OMP achieves an NMSE similar to the lower bound.

Figure 3.11 presents the NMSE of the channel estimation for the 4-ray exponential channel. In this channel, the MMSE channel estimation obtains a better performance compared with the 3GPP channel. Its NMSE is better than CS-

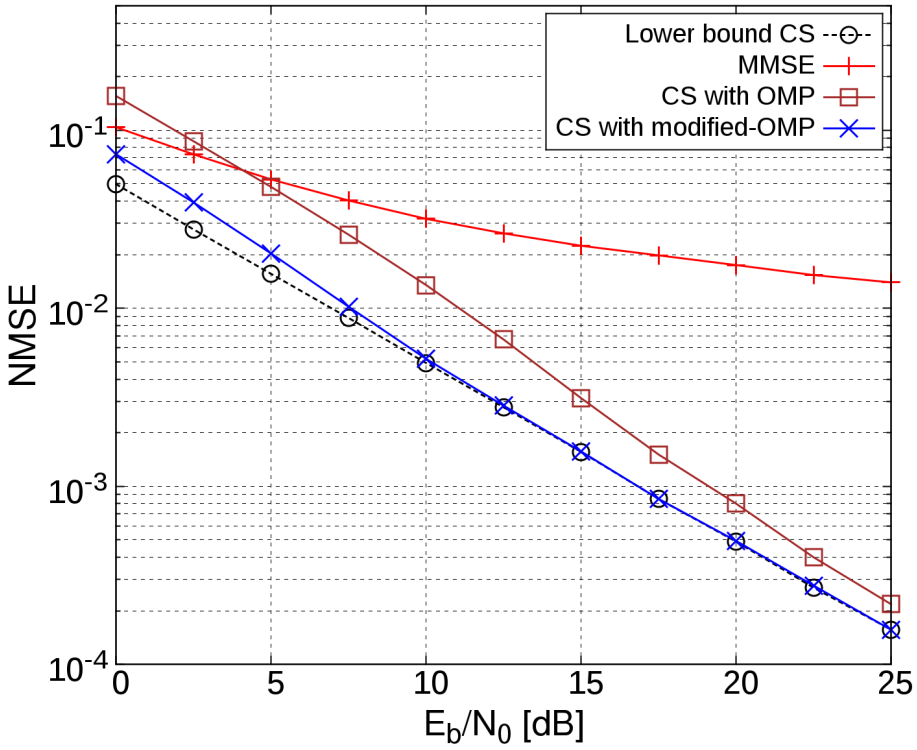

Figure 3.10: NMSE of the MMSE and CS-based channel estimation using the 3GPP case B channel and 16-QAM modulation.

based channel estimation with OMP. However, the CS-based channel estimation with modified-OMP obtains the smallest NMSE. Moreover, its NMSE is almost the same as the lower bound for all E_b/N_0.

From the BER and NMSE simulation results, it can be observed that with both channel models the CS-based channel estimation using modified-OMP gives better results. These results also confirm that the proposed modified-OMP algorithm achieves a better performance than OMP. Therefore, the modified-OMP algorithm has a better performance while also a smaller computational complexity.

The reason of the better performance of the modified-OMP algorithm is its higher recovery accuracy compared with OMP. The recovery accuracy determines how accurately the algorithm recovers the delay positions of the estimated CIR. Figure 3.12 presents the average recovery percentage of the delay positions for

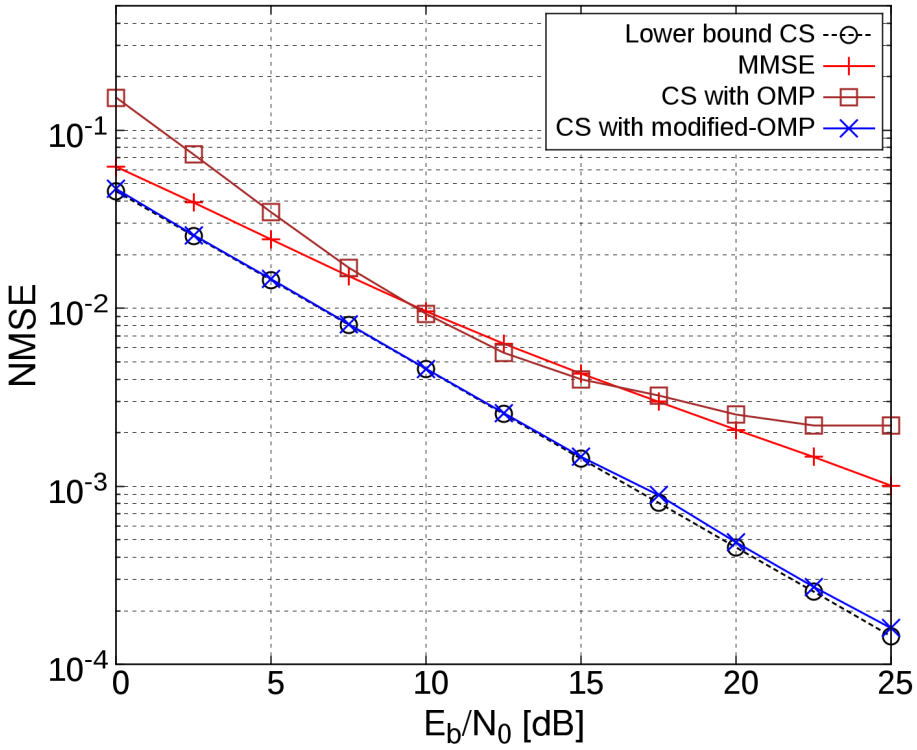

Figure 3.11: NMSE of the MMSE and CS-based channel estimation using 4-ray exponential channel and 16-QAM modulation.

channels with different number of paths. It considers k-path channels with exponential decay and the delay position of each path was randomly chosen from the interval [0,15]. Compared to OMP, the modified-OMP algorithm obtained a better recovery accuracy even in a 6-path channel. In the case of 2-path, modified-OMP recovers the exact position of the delays with 100% accuracy. In the case of 4-path, the accuracy of modified-OMP is very close to 100% except for E_b/N_0<5 dB. For 6-path, the accuracy is much smaller when E_b/N_0<10 dB, but it reaches around 100% for E_b/N_0>10 dB. Therefore, when the number of paths of the channel is increased, the recovery accuracy would be reduced and as consequence the BER would be degraded too.

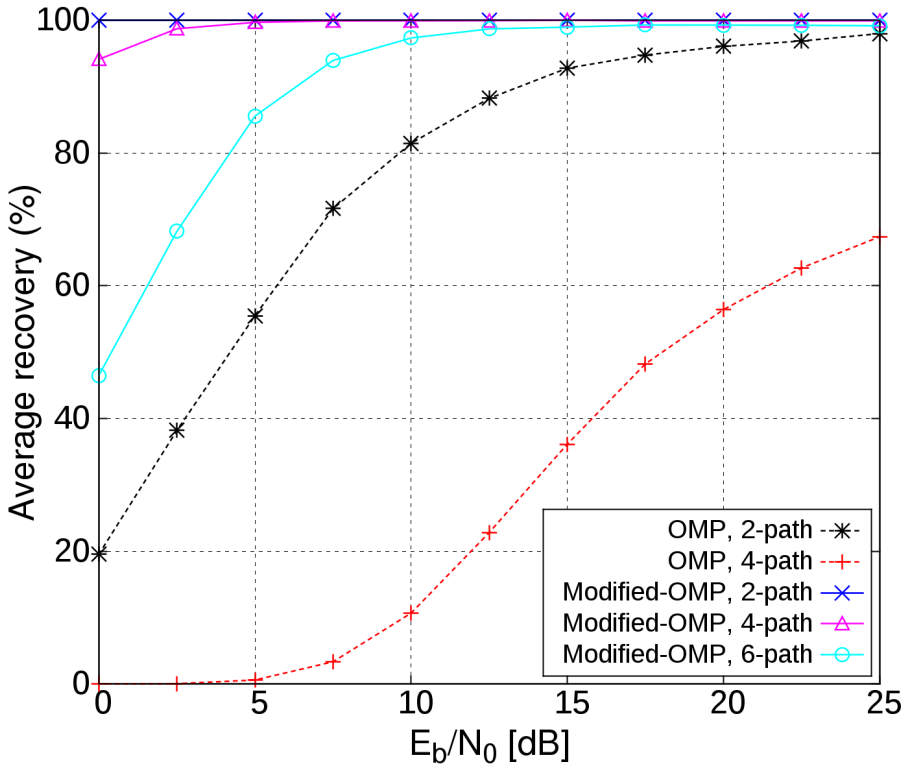

Figure 3.12: Average recovery percentage of the delay positions for the CS-based channel estimation using OMP and modified-OMP algorithms with 16-QAM.

3.6.2 Submatrix Detection Performance

The BER performance and average computational cost of the submatrix detection are compared with the block detection. Figure 3.13 presents a comparison of the BER performance between the block detection (dashed line) and submatrix detection (solid line), using QPSK and 16-QAM modulation. The CS-based channel estimation with modified-OMP and the 3GPP case B channel are also utilized in this simulation.

In the case of QPSK, the BER of the two detection schemes is very similar. However, in the case of 16-QAM there is a bigger degradation in the BER when the submatrix detection is used. This degradation is around 1 dB for a BER of 10^{-3}, while it is increased to around 3 dB for a BER of 10^{-4}.

The computational cost required in the detection was obtained from the sim-

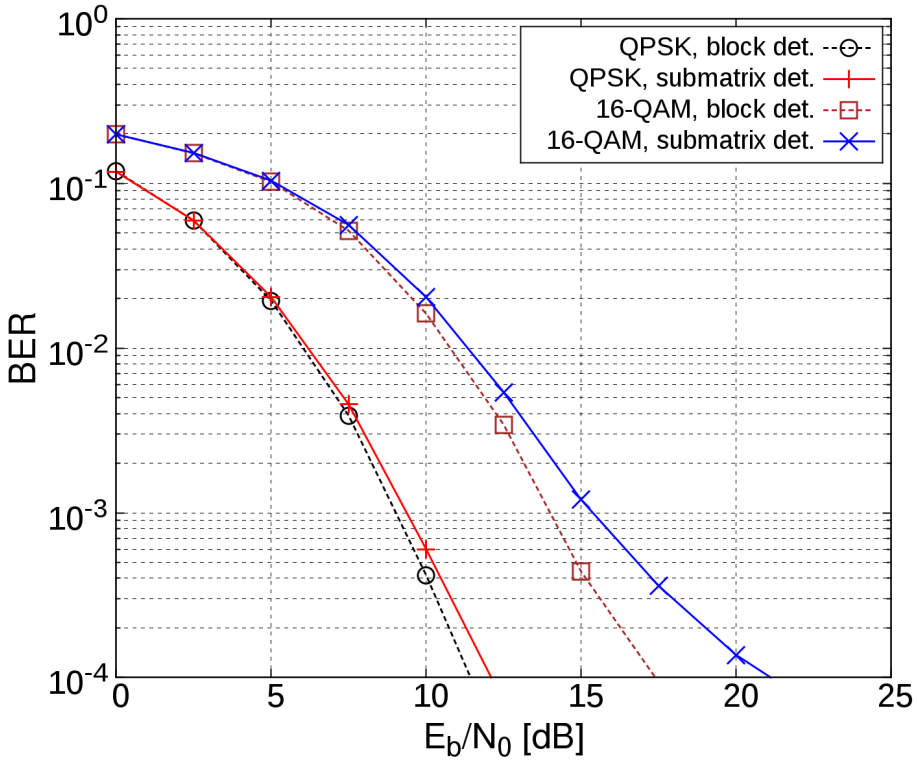

Figure 3.13: BER comparison of the block (dashed line) and submatrix detection (solid line) using CS-based channel estimation with modified-OMP and the 3GPP case B channel.

ulation and it is given as the number of average complex floating point operation (flop) required. As in [58], each complex addition is considered as one flop and each complex multiplication as three flop. Table 3.4 and Fig. 3.14 present the average number of flop per subcarrier required in the detection. The submatrix detection scheme, requires only around 8% of the computational cost required when the block detection is utilized. Consequently, the submatrix detection scheme reduces the computational cost by around 92% while the degradation in the BER is small. The proposed submatrix detection scheme offers a good trade-off between reduced computational cost and small BER degradation.

Table 3.4: Average number of flop per subcarrier required for the detection in the MIMO-OFDM receiver with ESPAR antenna

Detection scheme	QPSK	16-QAM	64-QAM
Block	27376	26669	26344
Submatrix	2171	2146	2135

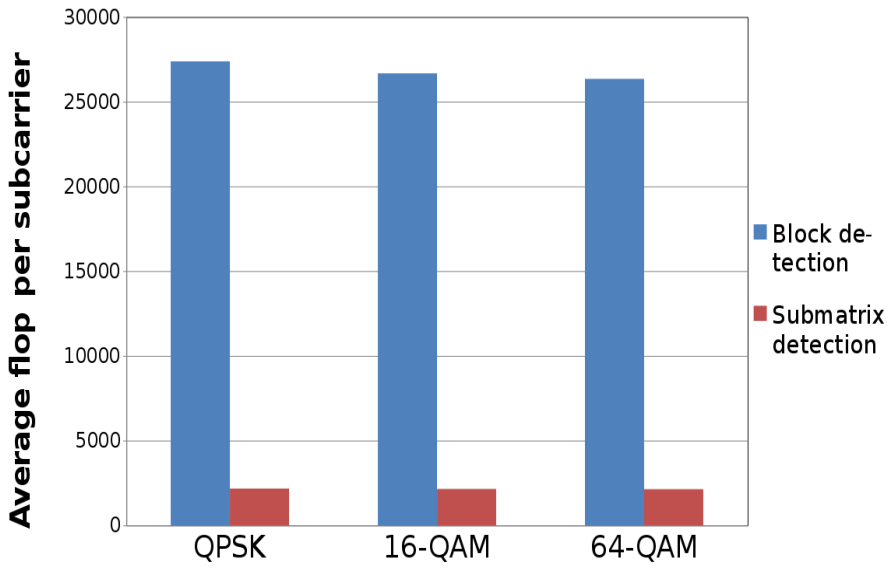

Figure 3.14: Comparison of the average flop per subcarrier required by block and submatrix detection.

3.6.3 Synchronization Performance

To confirm the results of the synchronization analysis presented in Section 3.5, a simulation to estimate and compensate the CFO was implemented. The CFO estimation is achieved by measuring the correlation between the CP and tail of the OFDM symbol, and it is obtained by [67]

$$\tilde{\epsilon} = \frac{1}{2\pi}\arg\left\{\sum_{n=-N_{cp}}^{-1} y^*(n)y(n+N)\right\}, \tag{3.52}$$

where $\tilde{\epsilon}$ is the estimated normalized CFO, $y(k)$ is the time domain received signal at time k, and $(\cdot)^*$ represents the conjugate operation.

Figure 3.15 shows the BER results using perfect CSI and normalized CFO of 0.3. It includes the BER with and without CFO estimation, and also for comparison it includes the BER with perfect synchronization. It can be seen that the CFO severely affects the BER when it is not estimated. On the other hand, using the CFO estimation the BER is very similar to the BER with perfect synchronization. Therefore, accurate CFO estimation is possible in the MIMO-OFDM receiver with ESPAR antenna.

3.7 Summary

This chapter presented a MIMO-OFDM receiver using a 3-element ESPAR antenna with periodic alternating directivity. The simulation results show that the receiver can obtain a diversity gain of about 14 dB for a BER of 10^{-3} and using perfect CSI. This diversity gain is obtained without requiring additional RF chains, which is the main disadvantage of conventional MIMO-OFDM systems. The receiver, which has only two RF chains in the receiver side, obtains a BER close to a conventional 2×4 MIMO-OFDM system that has four RF chains.

For channel estimation, MMSE and CS-based schemes were presented. The CS-based channel estimation with modified-OMP obtains the best performance and requires less computational complexity than the MMSE channel estimation. A submatrix detection scheme was proposed as a lower complexity alternative to the block detection. The submatrix detection reduces the required computational

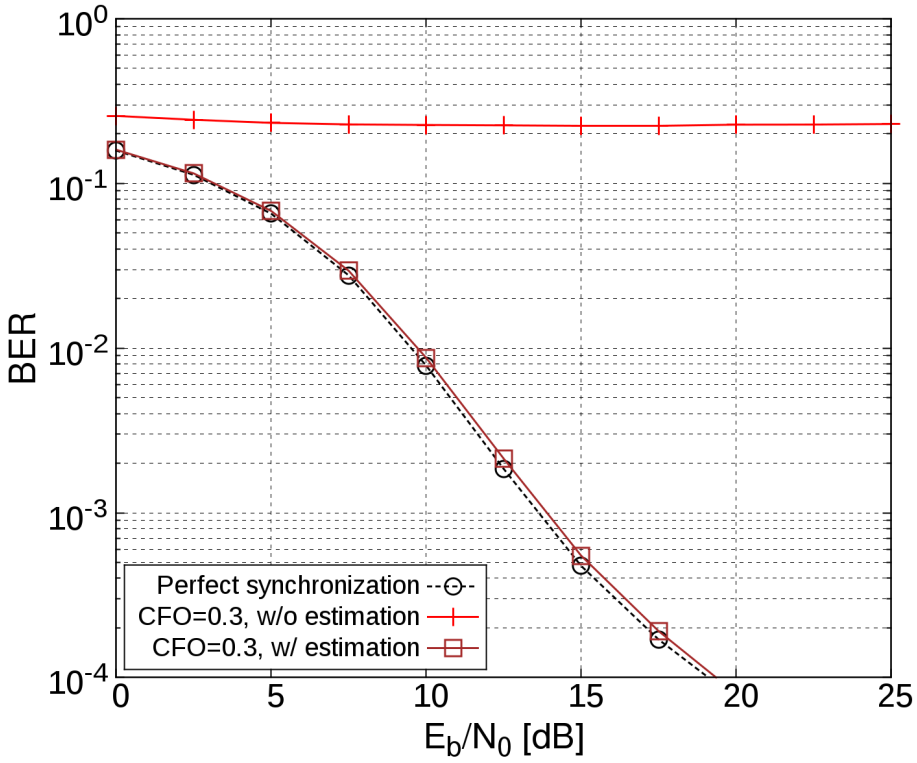

Figure 3.15: BER with CFO effect. Perfect CSI, 3GPP case B channel, 16-QAM, and submatrix detection.

cost; however, it causes a small degradation in the BER. For 16-QAM modulation, the degradation is about 1 dB for a BER of 10^{-3} and 3 dB for a BER of 10^{-4}. On the other hand, the advantage of this detection scheme is the reduction of about 92% of the required computational cost compared with the block detection approach.

The problem of the synchronization was also discussed in this chapter. It was shown that a simple synchronization scheme, which exploits the similarity between the cyclic prefix and tail of the OFDM symbol, can also be used in the ESPAR antenna-based receiver.

Chapter 4

ESPAR Antenna-Based ISDB-T Receivers

This chapter presents two ESPAR antenna-based ISDB-T receivers. In the first part of the chapter, an ISDB-T receiver with 3-element ESPAR antenna is presented. The ideal and real model of the 3-element ESPAR antenna are described, and the performance of the two models is obtained using a simulation. In the second part, an ISDB-T receiver considering the real model of a 4-element ESPAR antenna is presented. CS-based channel estimation and low complexity equalization are proposed for this receiver. Finally, the simulation results of the performance of this receiver are presented.

4.1 Introduction

The ISDB-T [5] standard for DTV broadcasting can provide SDTV, HDTV, one-seg reception for hand-held devices, and other services. This standard uses OFDM, which is robust against frequency-selective fading, multipath fading, and ISI [20]. In on-vehicle ISDB-T receivers, multipath fading and Doppler shift can significantly affect the received signal. One of the solutions to combat multipath fading is the antenna diversity, which employs multiple receiving antennas where each one is connected to a RF chain using coaxial cable. Figure 1.1 presented the on-vehicle ISDB-T receiver with antenna diversity. It is composed of two antennas, which are connected to the ISDB-T receiver using coaxial cable. It is also

composed of two RF chains and a combiner. The main problem of this diversity receiver is the installation of the antennas and cabling between the antennas and receiver. The additional antenna and cabling increases the installation time and complexity compared to a receiver that requires only one antenna. Therefore, a solution that uses only one antenna and still obtains diversity would reduce the installation cost.

A scheme to obtain diversity using a single ESPAR antenna was presented in [28]. It switches between two different radiation patterns according to the received signal strength and it can obtain diversity gain. However, the performance improvement is less than that of other schemes with antenna diversity. This scheme was also applied in an ISDB-T receiver in [29]. An OFDM receiver using a 2-element ESPAR antenna with periodically alternating directivity was proposed in [12]. The frequency of the directivity change is the same as the subcarrier frequency spacing. This scheme obtained diversity gain; however, it only considered an ideal model of the ESPAR antenna. It also assumed a block-type pilot structure where all subcarriers are used as pilots in the first OFDM symbol. On the other hand, ISDB-T employs a scattered pilot structure that has a pilot subcarrier every twelve subcarriers. Therefore, the scheme proposed in [12] cannot be directly adopted in ISDB-T due to the different pilot structure.

In this chapter, ESPAR antenna-based ISDB-T receivers are proposed. The objective of these receivers is to simplify its installation process in the vehicle. The ESPAR antenna-based receiver requires only a single ESPAR antenna; thus, a single coaxial cable connects it to the receiver. Additionally, it requires only a single RF chain; therefore, it reduces the hardware complexity. The channel estimation and detections schemes for this receivers are very important and its design presents challenges for obtaining good accuracy while reducing the required computational cost. These challenges are addressed with the schemes presented in this chapter.

In the first part of the chapter, an ISDB-T receiver using a 3-element ESPAR antenna with periodically alternating directivity is presented. The directivity is changing at 12 times the OFDM subcarrier frequency spacing, which is equivalent to the separation between two consecutive pilot subcarriers. The 3-element ESPAR antenna is utilized considering two models: ideal and real model. The

ideal model is similar to the one used in the previous chapter, while the real model is determined from the mutual coupling between the antenna elements. The performance results will show that the real model obtains less diversity gain compared with the real model.

In the second part of this chapter, an ISDB-T receiver using a 4-element ESPAR antenna with periodically alternating directivity is presented. This receiver considers the real model of the ESPAR antenna and improves the diversity gain. The ISDB-T receiver with 4-element ESPAR antenna cannot use least squares (LS) channel estimation [68] due to the intercarrier interference (ICI) generated by the periodically alternating directivity of the ESPAR antenna. Instead, it uses a CS-based channel estimation that is similar to the one utilized in the previous chapter. Due to the ICI, a block frequency equalization is required for obtaining the transmitted symbols. The MMSE sparse-SQRD algorithm can be used, but it requires a high computational cost due to the large size of the channel matrix. Similar to the previous chapter, a equalization scheme that is based on a submatrix division of the channel matrix is presented. The submatrix equalization reduces the required computational cost; however, it causes a small degradation in the BER performance.

4.2 ISDB-T Receiver with 3-element ESPAR Antenna

Figure 4.1 presents the 3-element ESPAR antenna with periodically alternating directivity that is used for this ISDB-T receiver. It is composed of a radiator element (#0) and two parasitic elements (#1, #2). The directivity of the ESPAR antenna is periodically changed by the sinusoidal waves supplied as bias voltage to the parasitic elements. These sine and cosine functions have frequency kf_s, where k is an integer constant and f_s is the OFDM subcarrier frequency spacing. In ISDB-T, the separation between two consecutive pilot subcarriers is 12; hence, the value of the integer constant is $k = 12$.

Due to the effect of electrical coupling between the antenna elements, the total received signal in the ESPAR antenna is the sum of the signals received in the radiator and parasitic elements. Considering an ideal design of the ESPAR

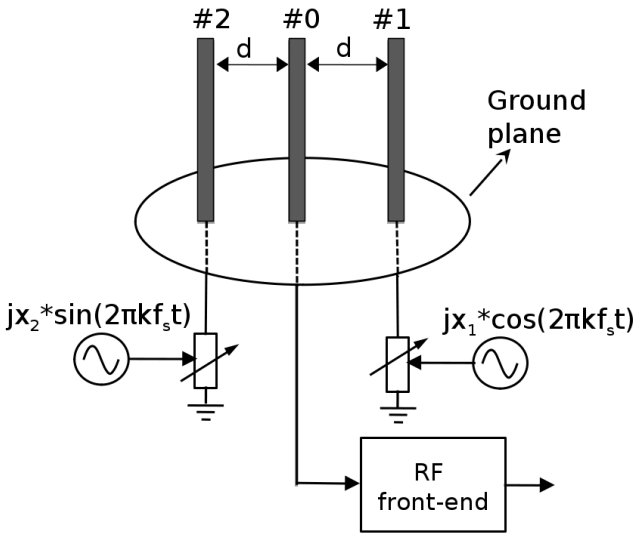

Figure 4.1: 3-element ESPAR antenna used in the ISDB-T receiver.

antenna, the effect of the sinusoidal waves connected to the parasitic elements is equivalent to multiplying the signals received in the parasitics elements (#1, #2) with the exponential functions $e^{j2\pi(12f_s)t}$ and $e^{-j2\pi(12f_s)t}$, respectively. Therefore, the baseband representation of the received signal at the output of the RF front-end is ideally modeled as

$$v(t) = v_0(t) + e^{j2\pi(12f_s)t}v_1(t) + e^{-j2\pi(12f_s)t}v_2(t), \tag{4.1}$$

where $v_0(t)$ is the signal received by the radiator element, $j = \sqrt{-1}$ is the imaginary unit, and $v_1(t)$, $v_2(t)$ are the signals received by the parasitic elements.

4.2.1 Real Model of 3-element ESPAR Antenna with Periodically Alternating Directivity

The impedance matrix of the 3-element ESPAR antenna with periodically alternating directivity is given by

$$\mathbf{Z} = \begin{bmatrix} Z_{00} & Z_{01} & Z_{02} \\ Z_{10} & Z_{11} & Z_{12} \\ Z_{20} & Z_{21} & Z_{22} \end{bmatrix}, \tag{4.2}$$

where due to the symmetry of the antenna elements

$$\begin{aligned} Z_{00} &= Z_{11} = Z_{22} \\ Z_{01} &= Z_{02} = Z_{10} = Z_{20} \\ Z_{12} &= Z_{21}. \end{aligned} \tag{4.3}$$

The values of $\mathbf{Z}$ depend of the antenna physical structure and can be obtained from the NEC simulator [32]. The reactance matrix $\mathbf{X}$ is periodically changing and it can be expressed at the discrete time i by

$$\mathbf{X}(i) = \begin{bmatrix} Z_0 & 0 & 0 \\ 0 & jx_1 \sin(\phi_i) & 0 \\ 0 & 0 & jx_2 \cos(\phi_i) \end{bmatrix}, \tag{4.4}$$

where Z_0 is the load impedance, $j = \sqrt{-1}$ is the imaginary unit, and ϕ_i is given by

$$\phi_i = 2\pi \frac{12i}{N}, \tag{4.5}$$

where N is the FFT window size of the ISDB-T receiver and $i = \{0, 1, \ldots, N-1\}$. The equivalent weight vector at instant i is given by

$$\mathbf{w}(i) = 2Z_0(\mathbf{Z} + \mathbf{X}(i))^{-1} \cdot [1, 0, 0]^T, \tag{4.6}$$

and can be denoted also as

$$\mathbf{w}(i) = [w_0(i), w_1(i), w_2(i)]^T, \tag{4.7}$$

where $w_l(i)$ is the weight of the $\#l$-th antenna element at time i. The steering vector $\boldsymbol{\alpha}(\gamma)$ is based on the array geometry of the 3-element ESPAR antenna and is defined as

$$\boldsymbol{\alpha}(\gamma) = \begin{bmatrix} \alpha_0 \\ \alpha_1 \\ \alpha_2 \end{bmatrix} = \begin{bmatrix} 1 \\ e^{j2\pi d \cos(\gamma)} \\ e^{j2\pi d \cos(\gamma - \pi)} \end{bmatrix}, \tag{4.8}$$

where γ is the azimuthal direction of the incoming waves.

The baseband representation of the received signal at the output of the RF front-end is formulated as

$$v(t) = \alpha_0 w_0(t) v_0(t) + \alpha_1 w_1(t) v_1(t) + \alpha_2 w_2(t) v_2(t), \tag{4.9}$$

where $v_0(t)$ is the signal received by the radiator element and $v_1(t)$, $v_2(t)$ are the signals received by the parasitic elements. Equation (4.9) represents the real model of the 3-element ESPAR antenna. Figure 4.2 presents a representation of the equivalent baseband model of the ideal model, which was shown in Eq. (4.1), and the real model of the ESPAR antenna.

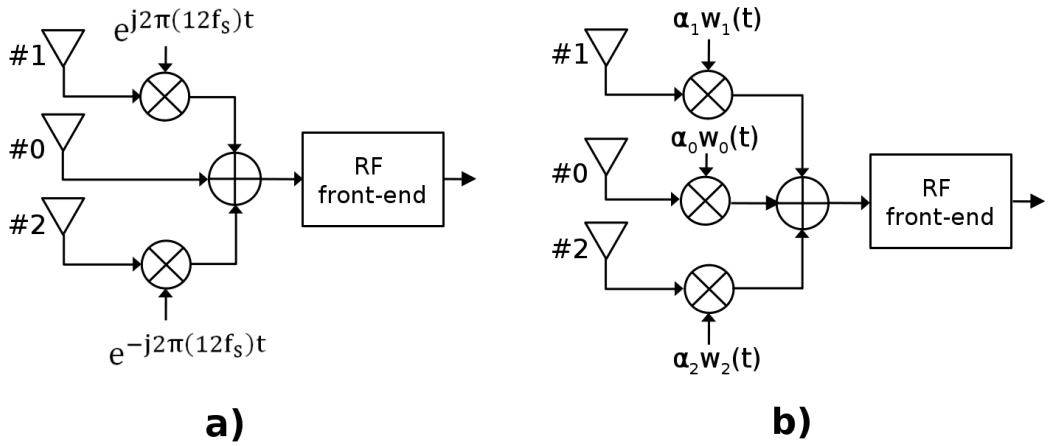

Figure 4.2: Equivalent baseband model of the 3-element ESPAR antenna. a) Ideal model, b) real model.

4.2.2 System Model

A conventional uncoded OFDM transmitter is considered; thus, the system does not require any special modification in the transmission side. The block diagram of the transmitter is shown in Fig. 4.3. The data stream is first modulated, then the data symbols are combined with the pilot symbols, which are used for channel estimation. It utilizes a comb-type pilot arrangement that inserts one pilot every 12 subcarriers. The data and pilot symbols are fed to the IFFT, and finally the GI is inserted.

The block diagram of the ISDB-T receiver is presented in Fig. 4.4. It uses the 3-element ESPAR antenna with its radiator element connected to the RF front-end. From the output of the RF front-end, the GI is removed and then the signal is fed to the FFT block to obtain the frequency domain equivalent. The

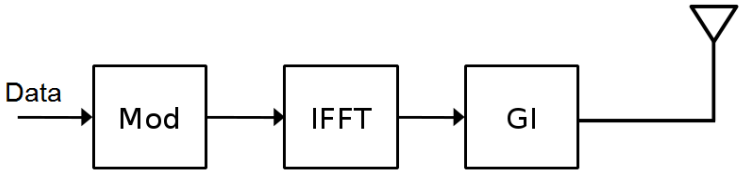

Figure 4.3: Block diagram of the OFDM transmitter.

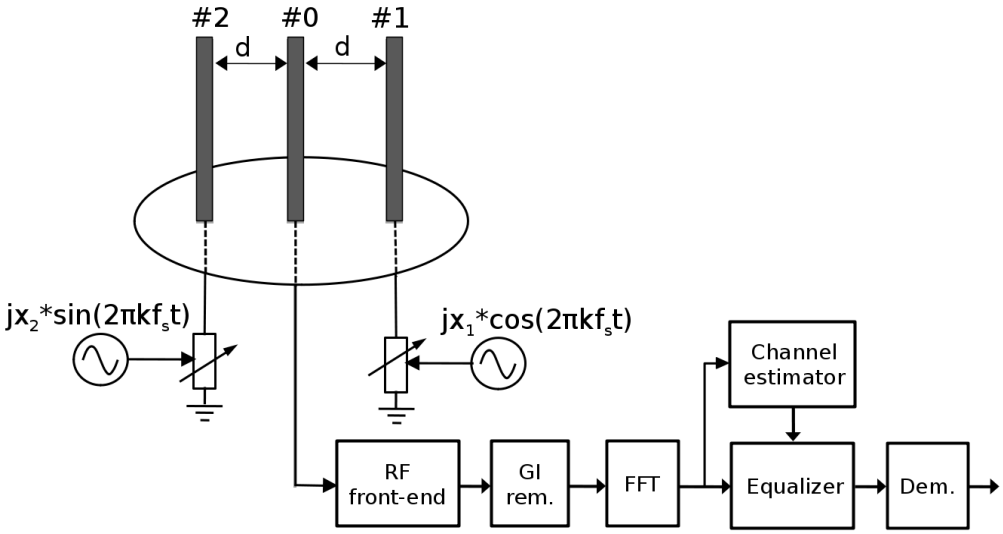

Figure 4.4: Block digram of the ISDB-T receiver with 3-element ESPAR antenna.

received pilot symbols are used for channel estimation and the equalizer recovers the transmitted symbols. Finally, the demodulator outputs the data stream.

Let $\mathbf{s}$ denote the vector of transmitted symbols in frequency domain given by

$$\mathbf{s} = [s_0, s_1, \ldots, s_{N-1}]^T, \tag{4.10}$$

where s_k represents the transmitted symbol at the k-th subcarrier. The vector of transmitted symbols in time domain at the output of the IFFT block is given by

$$\mathbf{v} = \mathbf{F}^H \mathbf{s}, \tag{4.11}$$

where $\mathbf{F}$ is the Fourier transform matrix. The matrix element $F_{l,m}$ corresponding to the l-th row and m-th column of $\mathbf{F}$ is given by

$$F_{l,m} = \frac{1}{\sqrt{N}} e^{-j\frac{2\pi lm}{N}}. \qquad \begin{matrix} 0 \leq l \leq N-1 \\ 0 \leq m \leq N-1 \end{matrix} \tag{4.12}$$

Considering that the signals received by each element of the ESPAR antenna have independent fading, the vector of received symbols after the GI is removed is given by

$$\mathbf{r} = (\mathbf{D}_0\mathbf{C}_0 + \mathbf{D}_1\mathbf{C}_1 + \mathbf{D}_2\mathbf{C}_2)\mathbf{v} + \mathbf{z}, \tag{4.13}$$

where $\mathbf{C}_k$ is the channel impulse response matrix corresponding to the $\#k$-th antenna element and $\mathbf{z}$ is the AWGN vector with σ^2 variance. The diagonal matrices $\mathbf{D}_k$ contain the antenna weights and depend on which model of the ESPAR antenna is considered. If the ideal model is considered, the matrices are given by

$$\begin{aligned} \mathbf{D}_0 &= \mathbf{I}_N \\ \mathbf{D}_1 &= \mathrm{diag}(1, e^{j2\pi\frac{12}{N}}, \ldots, e^{j2\pi\frac{12(N-1)}{N}}) \\ \mathbf{D}_2 &= \mathrm{diag}(1, e^{-j2\pi\frac{12}{N}}, \ldots, e^{-j2\pi\frac{12(N-1)}{N}}), \end{aligned} \tag{4.14}$$

where $\mathbf{I}_N$ is the identity matrix of size N $\times$ N. On the other hand, if the real model is considered the $\mathbf{D}_k$ matrix is given by

$$\mathbf{D}_k = \mathrm{diag}(\alpha_k w_k(0), \alpha_k w_k(1), \ldots, \alpha_k w_k(N-1)), \tag{4.15}$$

where α_k is the k-th component of the steering vector $\boldsymbol{\alpha}(\gamma)$ in Eq. (4.8), and $w_k(i)$ is the weight of the $\#k$-th antenna element at instant i obtained from equations (4.6) and (4.7).

The received signal $\mathbf{r}$ is applied to the FFT block and its frequency domain equivalent is given by

$$\mathbf{u} = \mathbf{F}\mathbf{r}, \tag{4.16}$$

and using Eq. (4.11) and (4.13), it is given by

$$\mathbf{u} = (\mathbf{G}_0\mathbf{H}_0 + \mathbf{G}_1\mathbf{H}_1 + \mathbf{G}_2\mathbf{H}_2)\mathbf{s} + \mathbf{z}_f, \tag{4.17}$$

where $\mathbf{z}_f$ is the noise vector in frequency domain, $\mathbf{H}_k$ is the channel frequency response matrix of the $\#k$-th antenna element given by

$$\mathbf{H}_k = \mathbf{F}\mathbf{C}_k\mathbf{F}^H, \tag{4.18}$$

and the matrix $\mathbf{G}_k$ is the frequency equivalent of $\mathbf{D}_k$, which contains the antenna weights, is given by

$$\mathbf{G}_k = \mathbf{F}\mathbf{D}_k\mathbf{F}^H. \tag{4.19}$$

Equation (4.17) can be expressed in a simplified way by

$$\mathbf{u} = \mathbf{H}\mathbf{s} + \mathbf{z}_f, \tag{4.20}$$

with the channel frequency response matrix $\mathbf{H}$ given by

$$\mathbf{H} = \mathbf{G}_0\mathbf{H}_0 + \mathbf{G}_1\mathbf{H}_1 + \mathbf{G}_2\mathbf{H}_2. \tag{4.21}$$

4.2.3 Simulation Results

Table 4.1: Parameters of the 3-element ESPAR antenna

Frequency	500MHz
Wavelength (λ)	0.6m
Z_0	75Ω
Monopole length (L_m)	0.25λ=15cm
d	0.1λ=6cm
x_1	50Ω
x_2	50Ω

Table 4.2: Power delay profile of the TU6 model

Tap number	Delay time(μs)	Power (dB)
1	0	-3
2	0.2	0
3	0.5	-2
4	1.6	-6
5	2.3	-8
6	5	-10

To obtain the impedance matrix of the 3-elements ESPAR antenna, the 4NEC2 [69] simulator was used. The antenna is composed of three monopoles of length ($L_m = 0.25\lambda$) with a separation of ($d = 0.1\lambda$) between them. The frequency of 500 MHz, which is part of the band used for TV broadcasting in Japan, was selected. A summary on the antenna parameters is presented in Table 4.1. The

Table 4.3: Simulation Settings

Modulation	QPSK
FFT window size	256
GI	1/8
Noise type	AWGN
Channel model	TU6
Channel estimation	Perfect CSI
Equalization	MMSE Sparse-SQRD

self-impedance Z_{00}, Z_{11}, and Z_{22} are obtained by simulating each antenna element separately. To obtain the mutual-impedance elements of the impedance matrix, we have to solve the system given by

$$\begin{aligned} V_0 &= I_0 Z_{00} + I_1 Z_{01} + I_2 Z_{02} \\ 0 &= I_0 Z_{10} + I_1 Z_{11} + I_2 Z_{12} \\ 0 &= I_0 Z_{20} + I_1 Z_{21} + I_2 Z_{22} \end{aligned} \tag{4.22}$$

where V_0 is the voltage in the terminals of the radiator element (#0), I_k is the current in the #k-th antenna element, and Z_{ik} (for $i \neq k$) is the mutual-impedance between the i-th and k-th antenna elements. The values of V_0, I_0, I_1, and I_2 are also obtained from the simulation. The rest of the parameters can be calculated replacing the equivalences shown in Eq. (4.3) into Eq. (4.22). Finally, the resulting impedance matrix is

$$\mathbf{Z} = \begin{bmatrix} 44.7 + j25.7 & 39.13 + j2.31 & 39.13 + j2.31 \\ 39.13 + j2.31 & 44.7 + j25.7 & 24.28 - j14.25 \\ 39.13 + j2.31 & 24.28 - j14.25 & 44.7 + j25.7 \end{bmatrix}. \tag{4.23}$$

A simulation model of the ISDB-T receiver with ESPAR antenna was implemented in c++ using the it++ [64] communications library. The BER performance is obtained using the ideal and real model of the 3-element ESPAR antenna. The simulation implemented the system depicted in Fig. 4.3 and 4.4, but only considering perfect CSI and $N = 256$. A Typical Urban 6-path (TU6) [70] channel model is considered and its power delay profile is presented in Table 4.2. Moreover, a summary of the simulation parameters is presented in Table 4.3.

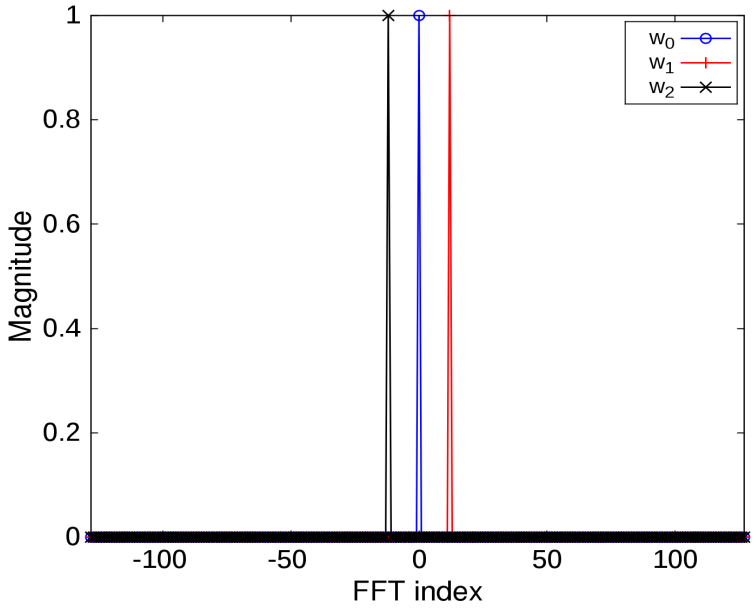

Figure 4.5: Frequency spectrum of $\mathbf{w}$ using the ideal model of the 3-element ESPAR antenna.

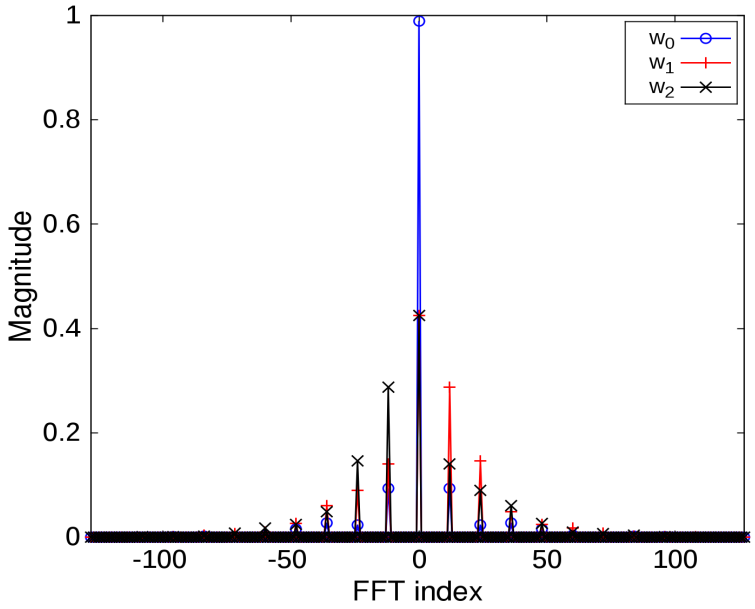

Figure 4.6: Frequency spectrum of $\mathbf{w}$ using the real model of the 3-element ESPAR antenna.

Figure 4.5 and 4.6 present the frequency spectrum of the antenna weights $\mathbf{w}_k$ for the ideal and real model, respectively. These figures show the magnitude of the frequency spectrum using the FFT operation. For fair comparison, the antenna weights $\mathbf{w}_k$ were normalized and limited to a maximum power of 1. Figure 4.5 shows that for the ideal model, $\mathbf{w}_0$ has only DC component. Additionally, $\mathbf{w}_1$ and $\mathbf{w}_2$ have only fundamental components at +12 and -12, respectively. On the other hand, the frequency spectrum of the real model presented in Fig. 4.6 has several differences compared with the ideal model. First, there are several harmonic components at multiples of +12 and -12, which have a decreasing magnitude. Second, $\mathbf{w}_1$ and $\mathbf{w}_2$ have positive and negative frequency components simultaneously. Finally, the amplitudes of $\mathbf{w}_1$ and $\mathbf{w}_2$ are smaller compared with $\mathbf{w}_0$.

Figure 4.7 presents the BER performance of the ISDB-T receiver considering the ideal and real model of the 3-element ESPAR antenna. For comparison, it is included the BER of other conventional systems: a single-input single-output (SISO), an antenna diversity scheme with one transmitter and two receivers (Tx=1, Rx=2) using MRC, and another antenna diversity scheme (Tx=1, Rx=3) using MRC. This figure shows that the ISDB-T receiver that considers the ideal model of the 3-element ESPAR antenna can obtain a BER that is better than a conventional antenna diversity scheme with two receivers (Tx=1, Rx=2). However, when the real model is considered, the BER is degraded and there is a reduction of about 6 dB in the diversity gain. This smaller diversity gain in the real model is caused by the smaller amplitudes of the antenna weights $\mathbf{w}_1$ and $\mathbf{w}_2$.

The simulation results showed that there is a big degradation in the BER when the real model of the 3-element ESPAR antenna is considered. This emphasizes the importance of the design of the antenna to obtain an impedance matrix $\mathbf{Z}$ that offers a strong coupling between the antenna elements. In the next section, an ISDB-T receiver with a 4-element ESPAR antenna is presented to improve the diversity gain even when the real model of the antenna is utilized.

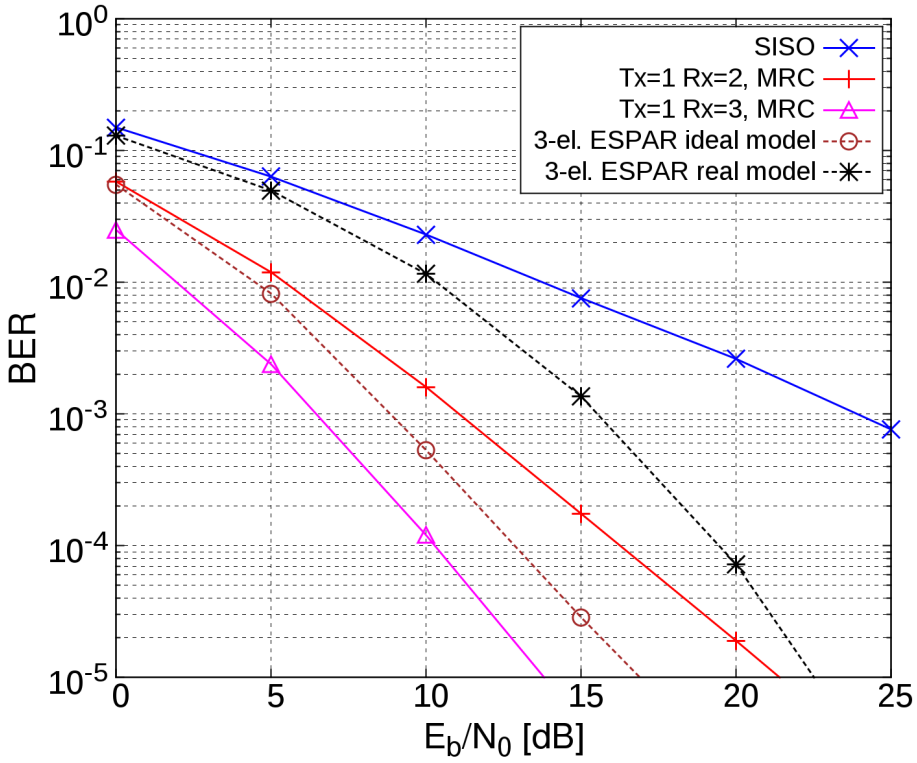

Figure 4.7: Comparison of the BER of the ISDB-T receiver with 3-element ESPAR antenna versus other conventional receivers without ESPAR antenna. Perfect CSI and TU-6 channel.

4.3 ISDB-T Receiver with 4-element ESPAR Antenna

4.3.1 Real Model of 4-element ESPAR Antenna

Figure 4.8 presents the proposed 4-element ESPAR antenna with periodically alternating directivity, which is composed of a radiator element (#0) and three parasitic elements (#1,#2,#3). Similar to the 3-element ESPAR antenna presented in the previous section, the variable reactances are controlled by sine and cosine functions of frequency kf_s.

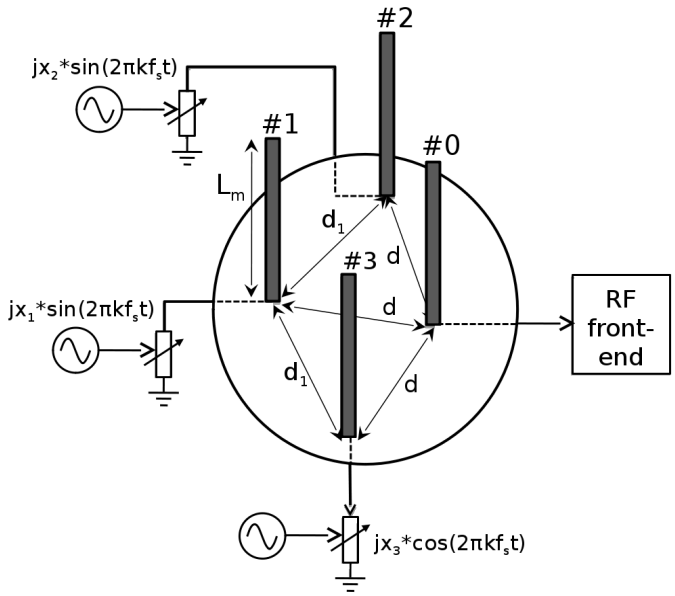

Figure 4.8: 4-element ESPAR antenna with periodically alternating directivity.

The impedance matrix of the 4-element ESPAR antenna is given by

$$\mathbf{Z} = \begin{bmatrix} Z_{00} & Z_{01} & Z_{02} & Z_{03} \\ Z_{10} & Z_{11} & Z_{12} & Z_{13} \\ Z_{20} & Z_{21} & Z_{22} & Z_{23} \\ Z_{30} & Z_{31} & Z_{32} & Z_{33} \end{bmatrix}, \tag{4.24}$$

and due to the symmetry of the elements

$$\begin{aligned} Z_{00} = Z_{11} = Z_{22} = Z_{33} \\ Z_{01} = Z_{02} = Z_{03} = Z_{30} = Z_{20} = Z_{10} \\ Z_{12} = Z_{13} = Z_{21} = Z_{31} \\ Z_{23} = Z_{32}. \end{aligned} \tag{4.25}$$

The reactance matrix $\mathbf{X}$ is periodically changing and it can be expressed at the discrete time instant i by

$$\mathbf{X}(i) = \begin{bmatrix} Z_0 & 0 & 0 & 0 \\ 0 & jx_1 \sin(\phi_i) & 0 & 0 \\ 0 & 0 & jx_2 \sin(\phi_i) & 0 \\ 0 & 0 & 0 & jx_3 \cos(\phi_i) \end{bmatrix}, \tag{4.26}$$

where $j = \sqrt{-1}$ is the imaginary unit and ϕ_i is given by

$$\phi_i = 2\pi \frac{12i}{N}, \tag{4.27}$$

for $i = \{0, 1, \ldots, N-1\}$. The equivalent weight vector at instant i is

$$\mathbf{w}(i) = 2Z_0(\mathbf{Z} + \mathbf{X}(i))^{-1} \cdot [1, 0, 0, 0]^T, \tag{4.28}$$

and can be denoted also as

$$\mathbf{w}(i) = [w_0(i), w_1(i), w_2(i), w_3(i)]^T, \tag{4.29}$$

where $w_l(i)$ is the weight of the $\#l$-th antenna element at instant i. The steering vector $\boldsymbol{\alpha}(\gamma)$ is formulated as

$$\boldsymbol{\alpha}(\gamma) = \begin{bmatrix} \alpha_0 \\ \alpha_1 \\ \alpha_2 \\ \alpha_3 \end{bmatrix} = \begin{bmatrix} 1 \\ e^{j2\pi d\cos(\gamma)} \\ e^{j2\pi d\cos(\gamma - \frac{11\pi}{36})} \\ e^{j2\pi d\cos(\gamma - \frac{61\pi}{36})} \end{bmatrix}. \tag{4.30}$$

Finally, the baseband representation of the received signal at the output of the RF front-end is formulated as

$$v(t) = \alpha_0 w_0(t) v_0(t) + \alpha_1 w_1(t) v_1(t) + \alpha_2 w_2(t) v_2(t) + \alpha_3 w_3(t) v_3(t). \tag{4.31}$$

4.3.2 System Model

The block diagram of the proposed ISDB-T receiver with 4-element ESPAR antenna is presented in Fig. 4.9. Although it is similar in structure to the receiver with 3-element ESPAR antenna, the signal model is different. On the other hand, the transmitter that was presented in Fig. 4.3 is also used. Therefore, the vector of transmitted symbols in time domain $\mathbf{v}$ given in Eq. (4.11) is considered.

In the 4-element ESPAR antenna presented in Fig. 4.8, the separation between elements is at least 0.09λ. The small separation between antenna elements gives strong mutual coupling. According to [71], the mutual coupling tends to reduce the correlation between elements so an acceptable diversity can be obtained with separations of 0.1λ. Another study, used even a smaller separation

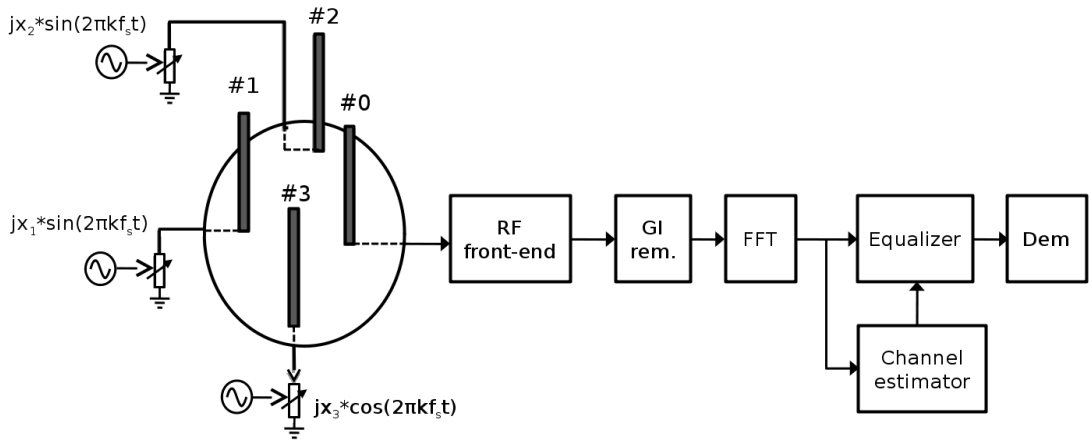

Figure 4.9: Block diagram of the ISDB-T receiver with 4-element ESPAR antenna.

of 0.05λ to obtain angle switch diversity [29] using ESPAR antenna. Therefore, the assumption of a separation of 0.09λ can ideally offer independent fading in the antenna elements; although, in practice they might have small correlations. It is important to clarify that a small correlation between elements does not affect the design of the proposed receiver; although, it would reduce the diversity gain. In this dissertation, we assume that the signal received in each element has independent fading so that we obtain the best possible diversity gain. With this assumption, the received signal at the output of the 4-element ESPAR antenna can be expressed as

$$\mathbf{r} = (\mathbf{D}_0\mathbf{C}_0 + \mathbf{D}_1\mathbf{C}_1 + \mathbf{D}_2\mathbf{C}_2 + \mathbf{D}_3\mathbf{C}_3)\mathbf{v} + \mathbf{z}, \tag{4.32}$$

where $\mathbf{C}_k$ is the channel impulse response matrix corresponding to the $\#k$-th antenna element and $\mathbf{z}$ is the AWGN vector with σ^2 variance. The diagonal matrices $\mathbf{D}_k$ are given by

$$\mathbf{D}_k = \text{diag}(\alpha_k w_k(0), \alpha_k w_k(1), \ldots, \alpha_k w_k(N-1)), \tag{4.33}$$

where α_k is the k-th component of the steering vector $\boldsymbol{\alpha}(\gamma)$ shown in Eq. (4.30), and $w_k(i)$ is the weight of the $\#k$-th antenna element at instant i obtained from equations (4.28) and (4.29).

From Eq. (4.32), the received signal in frequency domain is given by

$$\mathbf{u} = (\mathbf{G}_0\mathbf{H}_0 + \mathbf{G}_1\mathbf{H}_1 + \mathbf{G}_2\mathbf{H}_2 + \mathbf{G}_3\mathbf{H}_3)\mathbf{s} + \mathbf{z}_f, \tag{4.34}$$

where $\mathbf{z}_f$ is the noise vector in frequency domain. The channel frequency response matrix $\mathbf{H}$ given by

$$\mathbf{H} = \mathbf{G}_0\mathbf{H}_0 + \mathbf{G}_1\mathbf{H}_1 + \mathbf{G}_2\mathbf{H}_2 + \mathbf{G}_3\mathbf{H}_3. \tag{4.35}$$

The matrix structure of $\mathbf{H}$ is presented in Fig. 4.10. The white zones in the figure represent the elements with zero value, while the others are non-zero elements with an absolute value represented using the gray scale (black equals the strongest value and white the zero value). The figure shows that the matrix has a main diagonal, several upward shifted diagonals, and several downward shifted diagonals. The diagonals are shifted in intervals of 12, which is the same separation between two consecutive pilot subcarriers, and also is the frequency of the oscillators that controls the variable reactance of the antenna elements (#1, #2, #3). As observed in the figure, the elements of the main diagonal have the strongest absolute value, while the elements in the shifted diagonals have decreasing absolute value.

The matrix structure of $\mathbf{H}$ produces ICI, which affects the subcarriers. According to Fig. 4.10, the non-zero diagonals of $\mathbf{H}$ are shifted on intervals of twelve subcarriers. This interval was chosen so that the data subcarriers interfere only with other data subcarriers and the pilot subcarriers only with other pilot subcarriers. Therefore, we can still use the symbols received in the pilot subcarriers to estimate the channel state information.

To explain the diversity effect, let us first recall that the signal at the output of the proposed 4-element ESPAR antenna is the weighted sum of the signal on each of its elements. It is also considered that each antenna element has independent fading, therefore the received signal is the sum of four different observations of the transmitted signal. Additionally, the periodically alternating directivity generated by the oscillators creates a frequency shift in the received signals. This frequency shift is the explanation of the multiple non-zero diagonals present in the channel matrix $\mathbf{H}$. Consequently, we have the combination of four different observations of the transmitted signal and a channel matrix that is the

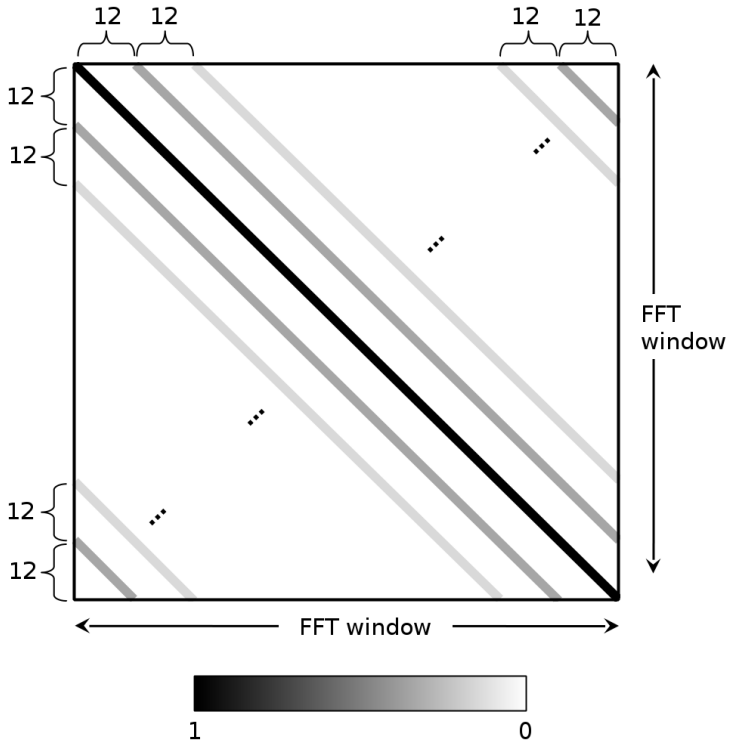

Figure 4.10: Matrix structure of **H** when the proposed 4-element ESPAR antenna is used.

combination of four channel responses distributed in several diagonals. These two characteristics are combined to achieve diversity gain.

4.3.3 CS-Based Channel Estimation

Least squares channel estimation [68] is commonly used in OFDM receivers due to its simplicity. Using this technique, the channel frequency response at the pilot subcarriers is easily computed by dividing the received pilot symbols with the transmitted pilot values. Then, the channel frequency response is obtained using interpolation. Regardless of its simplicity, the proposed receiver cannot use this technique due to the ICI generated by the 4-element ESPAR antenna. Like in the previous chapter, a CS-based channel estimation is a good alternative to recover the channel with good accuracy and low computational complexity.

The target of the proposed ISDB-T receiver with ESPAR antenna is vehicles;

hence, the effect of the mobility has to be considered. When the receiver is moving, the channel is changing so it is called a time-varying channel, and combined with the frequency-selectivity of the channel it becomes a doubly-selective fading channel. The effect of the movement of the receiver, which is called Doppler shift or Doppler spread, is the destruction of the orthogonality of the subcarriers and the presence of ICI. The Doppler shift can cause an important degradation in the BER when it is not estimated and compensated.

CS-based channel estimation for doubly-selective fading channels have been investigated in [40, 54, 72]. In these works, a 2-dimension measurement matrix is utilized. Considering a frame is composed of N_t OFDM symbols and a 1- dimension measurement matrix of size $n \times m$, the resulting 2-dimension measurement matrix has a size of $nN_t \times mN_t$. The large size of this matrix implies high computational cost for the recovery process. The output of the recovery algorithm contains the necessary parameters to build the channel impulse response matrix; however, to obtain the channel frequency response matrix another high complexity calculation is required. For these reasons, the CS-based channel estimation proposed in [40, 54, 72] is not practical for ISDB-T receivers due to the large number of subcarriers utilized.

A CS-based channel estimation using 1-dimension measurement matrix is presented in Fig. 4.11 for the ISDB-T receiver with 4-element ESPAR antenna. This scheme uses the received pilot symbols to estimate the CIR. Then, the channel frequency response is obtained using a FFT block and the channel matrix $\mathbf{H}$ is computed according to Eq. (4.35). In the rest of this section, the details of each step are presented.

Let N_p define the number of pilot subcarriers and $\boldsymbol{\rho}$ the index vector containing the pilot positions $\boldsymbol{\rho} = [\rho_1, \rho_2, \ldots, \rho_{N_p}]$. The vector of received pilot symbols is given by

$$\mathbf{a} = [u_{\rho_1}, u_{\rho_2}, \cdots, u_{\rho_{N_p}}]. \tag{4.36}$$

The matrix $\mathbf{G}_k$ presented in Eq. (4.19) is a circulant matrix composed of non-zero diagonals separated by 12 positions, and its structure is similar to Fig. 4.10. This matrix can be expressed as

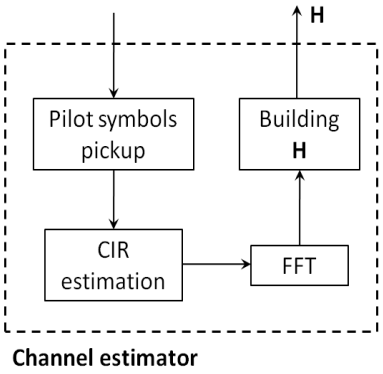

Figure 4.11: CS-based channel estimator of the ISDB-T receiver with 4-element ESPAR antenna.

$$\mathbf{G}_k = \begin{bmatrix} G_k^0 & 0 & \dots & G_k^{-12} & 0 & \dots & G_k^{12} & \dots & 0 \\ 0 & \ddots & \ddots & 0 & \ddots & \ddots & 0 & \ddots & \vdots \\ \vdots & \ddots & \ddots & \vdots & \ddots & \ddots & \vdots & \ddots & G_k^{12} \\ G_k^{12} & 0 & \dots & G_k^0 & 0 & \dots & G_k^{-12} & \dots & 0 \\ 0 & \ddots & \ddots & \vdots & \ddots & \ddots & \dots & \ddots & \vdots \\ \vdots & \ddots & \ddots & 0 & \dots & \ddots & 0 & \dots & G_k^{-12} \\ G_k^{-12} & 0 & \dots & G_k^{12} & 0 & \dots & G_k^0 & \ddots & \vdots \\ \vdots & \ddots & \ddots & \vdots & \ddots & \ddots & \dots & \ddots & 0 \\ 0 & \dots & G_k^{-12} & \dots & 0 & G_k^{12} & 0 & \dots & G_k^0 \end{bmatrix}, \tag{4.37}$$

where G_k^l represents the value of the diagonal with index l. Choosing only the

elements of the non-zero diagonals, the matrix $\mathbf{B}_k$ is given by

$$\mathbf{B}_k = \begin{bmatrix} G_k^0 & G_k^{-12} & \dots & \dots & G_k^{24} & G_k^{12} \\ G_k^{12} & G_k^0 & \dots & \dots & G_k^{36} & G_k^{24} \\ \vdots & \ddots & \ddots & \ddots & \ddots & \vdots \\ \vdots & \ddots & \ddots & \ddots & \ddots & \vdots \\ G_k^{-24} & G_k^{-36} & \dots & \dots & G_k^0 & G_k^{-12} \\ G_k^{-12} & G_k^{-24} & \dots & \dots & G_k^{12} & G_k^0 \end{bmatrix}. \tag{4.38}$$

The $N_p \times 4L$ measurement matrix is the union of four submatrices and is defined by

$$\mathbf{\Psi} = [\mathbf{B}_0\mathbf{P}\mathbf{F}_L, \mathbf{B}_1\mathbf{P}\mathbf{F}_L, \mathbf{B}_2\mathbf{P}\mathbf{F}_L, \mathbf{B}_3\mathbf{P}\mathbf{F}_L], \tag{4.39}$$

where $\mathbf{P} = \text{diag}(P_1, P_2, \dots, P_{N_p})$ is a diagonal matrix with its elements being the pilot values and $\mathbf{F}_L$ is an $N_p \times L$ matrix built with parts of the Fourier transform matrix and is given by

$$\mathbf{F}_L = \frac{1}{\sqrt{N}} \begin{bmatrix} 1 & \omega^{\rho_1} & \dots & \omega^{\rho_1(L-1)} \\ 1 & \omega^{\rho_2} & \dots & \omega^{\rho_2(L-1)} \\ \vdots & \vdots & \dots & \vdots \\ 1 & \omega^{\rho_{N_p}} & \dots & \omega^{\rho_{N_p}(L-1)} \end{bmatrix}, \tag{4.40}$$

where $\omega = e^{-j2\pi/N}$ and L is an integer number in the interval $L \leq N$.

In ISDB-T, one pilot subcarrier is inserted every 12 subcarriers. Only the pilot subcarriers, which have equidistant positions, are used for channel estimation. The problem of the equidistant positions is bad recovery performance in CS due to the downsampling effect. In downsamling, the sampling rate of a signal is reduced by an integer factor M. The downsampled signal is obtained by selecting one out of M samples and this is repeated every M samples for the rest of the signal. The problem of downsampling is that in frequency domain the signal would suffer an aliasing effect. Figure 4.12 is presented to explain the effects of downsampling. An $f(t)$ signal consisting of 256 samples is considered. This figure shows the frequency domain equivalent obtained using the FFT for: **a)** the original signal $f(t)$, **b)** a downsampled version of $f(t)$ with M=4 (64 equidistant samples), and **c)** $f(t)$ sampled at random positions (64 samples). The aliasing effect due to the downsampling can be observed in **b)**, and it consists of the

signal having four aliases in different frequencies. It is interesting to observe that the aliasing effect is mitigated using random sampling, presented in **c)**. In this case, 64 samples are obtained from the original signal at positions selected from a uniform random distribution.

According to [36], the pilot symbol positions $\boldsymbol{\rho}$ should be chosen randomly from a uniform distribution. However, this is not applicable in ISDB-T due to the equidistant pilot positions generated by the comb-type pilot pattern. The equidistant pilot distribution gives a bad recovery performance in CS due to the aliasing effect explained in Fig. 4.12. Usually, the parameter L would be chosen to be equal to the GI length N_{GI}; however, this does not consider the aliasing effect. Considering that there is a pilot subcarrier every 12 subcarriers, the parameter L can be determined by

$$L = \left\lfloor \frac{N}{12} \right\rfloor, \tag{4.41}$$

where $\lfloor \cdot \rfloor$ is the floor operation. In this way the effect of the equidistant sampling is minimized and the recovery performance is not affected. However, this would reduce the maximum delay of the CIR that the CS-based channel estimation can recover.

The unknown sparse vector $\boldsymbol{\theta}$ is defined by

$$\boldsymbol{\theta} = [\mathbf{c}_0, \mathbf{c}_1, \mathbf{c}_2, \mathbf{c}_3]^T, \tag{4.42}$$

where $\mathbf{c}_k$ is a L-size row vector with the impulse response of the $\#k$-th antenna element. Finally, the vector of received pilot symbols $\mathbf{a}$ can be expressed as

$$\mathbf{a} = \boldsymbol{\Psi}\boldsymbol{\theta}. \tag{4.43}$$

Recovery Algorithm

The sparse unknown vector $\boldsymbol{\theta}$ is composed of the CIR of each element of the 4-element ESPAR antenna. Due to the closeness of the antenna elements, the positions of the non-zero components of each $\mathbf{c}_k$ vector can be considered the same. As an example, let us imagine that the first element of the subvector $\mathbf{c}_0$ has a non-zero value. Consequently, we can consider that the first element of $\mathbf{c}_1$, $\mathbf{c}_2$, and $\mathbf{c}_3$ also have a non-zero value in that position. This assumption was used in chapter 3 to reduce the computational cost and improve the performance

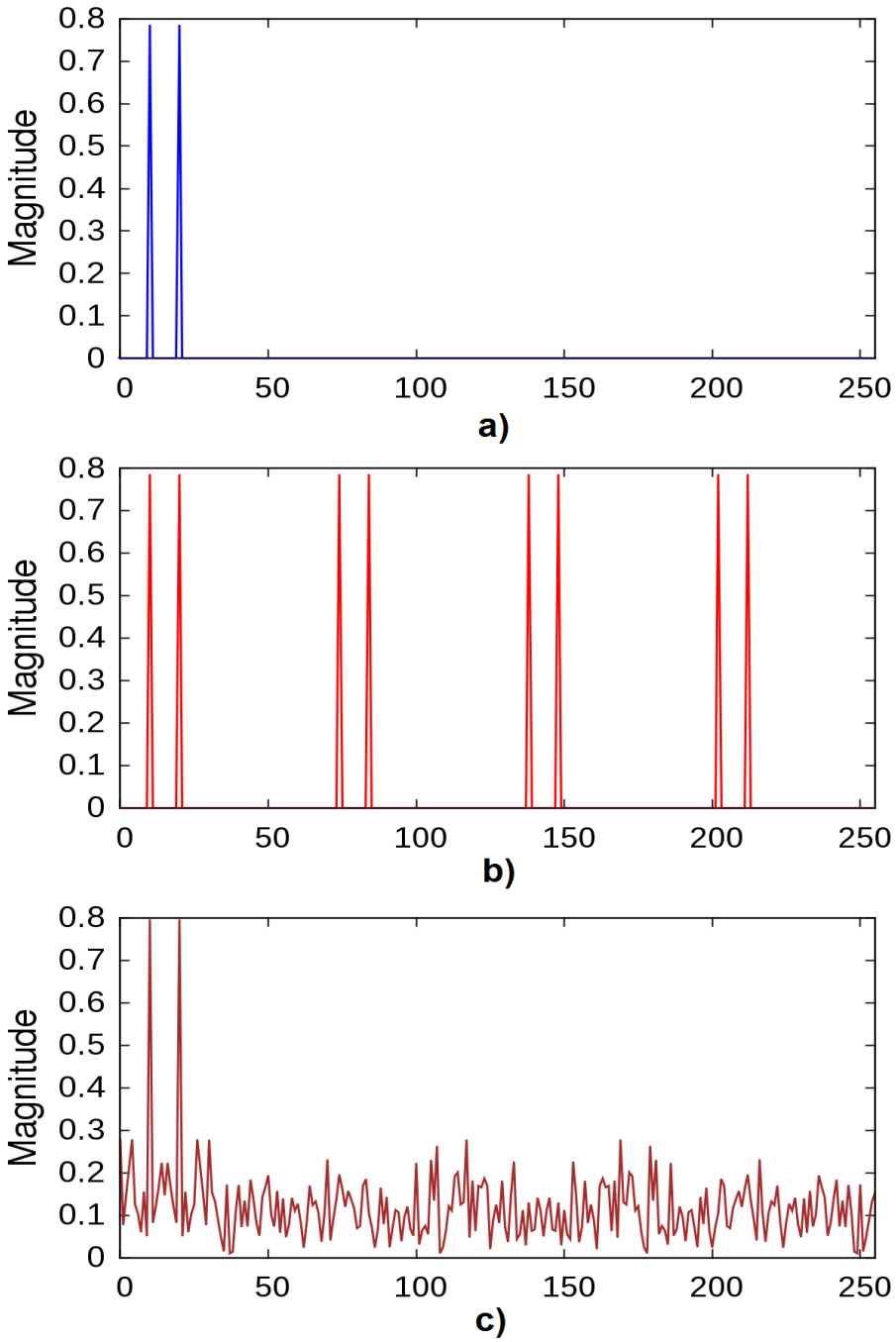

Figure 4.12: Frequency domain equivalent obtained using the FFT for: **a)** the original signal $f(t)$, **b)** a downsampled version of $f(t)$ with M=4 (64 equidistant samples), and **c)** $f(t)$ sampled at random positions (64 samples).

of the CS-based channel estimation. Using a similar approach for the proposed ISDB-T receiver, an algorithm called 4C-OMP was designed. This algorithm is based on OMP and selects four columns in each iteration.

The pseudocode of 4C-OMP is presented in Algorithm 4.1. The index of the most correlated column with the residual is obtained in line (7). Then, using the modulo operation the relative position of his column is obtained in line (8). The *for* loop in lines (10-14) replicate the index ω into the other four subvectors and build an index set Ω with these indices. Additionally, a matrix $\mathbf{E}$ is built with the columns of $\mathbf{\Psi}$ corresponding to these indices. The set Ω is added to the index set Λ_t and also $\mathbf{E}$ is added to $\mathbf{\Phi}_t$. Then, like in OMP, the new estimated signal is obtained by solving the least squares problem of line (17). The next step is to calculate the next residual and the procedure continues for the next iteration.

Algorithm 4.1 4C-OMP

1: Input: $\mathbf{a}$ (n-size observation vector)
2: Input: $\mathbf{\Psi}$ ($n \times m$ measurement matrix)
3: Input: S (sparsity level)
4: Input: L
5: $\mathbf{r}_0 := \mathbf{a}$, $\Lambda_0 := \emptyset$, $\mathbf{\Phi}_0 := [\ ]$
6: **for** $t = 1, \ldots, (S/4)$ **do**
7: $\quad \lambda_t :=$arg $\max_{j=1,\ldots,m} |\psi_j^T \mathbf{r}_{t-1}|$
8: $\quad \omega := \lambda_t \bmod L$
9: $\quad \Omega := \emptyset, \mathbf{E} := [\ ]$
10: $\quad$ **for** $i = 0, \ldots, 3$ **do**
11: $\quad\quad tmp := \omega + i * L$
12: $\quad\quad \Omega := \Omega \cup \{tmp\}$
13: $\quad\quad \mathbf{E} := [\mathbf{E}\ \ \psi_{tmp}]$
14: $\quad$ **end for**
15: $\quad \Lambda_t := \Lambda_{t-1} \cup \Omega$
16: $\quad \mathbf{\Phi}_t := [\mathbf{\Phi}_{t-1}\ \ \mathbf{E}]$
17: $\quad \mathbf{y}_t :=$arg $\min_y \|\mathbf{a} - \mathbf{\Phi}_t \mathbf{y}\|_2^2$
18: $\quad \mathbf{r}_t := \mathbf{a} - \mathbf{\Phi}_t \mathbf{y}_t$
19: **end for**
20: Output: $\tilde{\theta}$ (composed of $\mathbf{y}_t$ values at Λ_t positions)

Compared to OMP, 4C-OMP adds four columns to $\mathbf{\Phi}$ and four indices to Λ in each iteration. It also reduces the number of required iterations to $S/4$, which means that 4C-OMP requires only about one forth of the computational cost of OMP. According to [45], the computational cost of OMP is in the order of $O(Snm)$ for an $n \times m$ measurement matrix. Considering that we use an $N_p \times 4L$ measurement matrix, the computational cost of the 4C-OMP algorithm is in the order of $O(SN_pL)$.

In a doubly-selective fading channel, the CIR of the OFDM symbols in a frame has a small variation; thus, the positions of the non-zero elements can be considered to be the same for all symbols in the frame. Structured CS [52] can exploit this property to improve the recovery efficiency. The idea used in 4C-OMP can be combined with the SOMP algorithm, which implements structured CS. The resulting algorithm is called 4C-SOMP, and it improves the recovery accuracy while having low computational complexity.

The pseudocode of 4C-SOMP is presented in Algorithm 4.2. While in 4C-OMP the input is a vector of observations, in 4C-SOMP the input is an $n \times N_t$ matrix where each column is the vector of observations for every OFDM symbol in the frame. Another difference is obtaining the most correlated column with the residual, presented in line (7). Every column of the measurement matrix ψ_j^T is multiplied with the residual matrix and the norm of the resulting vector is obtained. The most correlated column is the one having the maximum norm. Then, lines (8-16) are the same as in 4C-OMP. Other differences are in solving the least squares problem and calculating the residual in lines (17) and (18), respectively. In 4C-SOMP, the result of the least squares and residual are matrices. Finally, the output $\tilde{\mathbf{Y}}$ is also a matrix that has non-zero rows in the positions given by the index set Λ_t.

4.3.4 Equalizer

The ISDB-T receiver with ESPAR antenna requires a special frequency equalization. All subcarriers in the channel matrix $\mathbf{H}$ have to be equalized simultaneously, thus a block equalizer is required. The channel matrix, which was previously shown in Fig. 4.10, has a sparse structure. Therefore, the MMSE sparse-SQRD algorithm can be used as block equalizer. However, due to the big number of sub-

Algorithm 4.2 4C-SOMP

Input: $\mathbf{X}$ ($n \times q$ matrix of observation vectors)
Input: $\mathbf{\Psi}$ ($n \times m$ measurement matrix)
Input: S (sparsity level)
Input: L
$\mathbf{R}_0 := \mathbf{X}$, $\Lambda_0 := \emptyset$, $\mathbf{\Phi}_0 := [\ ]$
for $t = 1, \ldots, (S/4)$ **do**
    $\lambda_t :=$arg $\max_{j=1,\ldots,m} \|\boldsymbol{\psi}_j^T \mathbf{R}_{t-1}\|$
    $\omega := \lambda_t \bmod L$
    $\Omega := \emptyset, \mathbf{E} := [\ ]$
    for $i = 0, \ldots, 3$ **do**
        $tmp := \omega + i * L$
        $\Omega := \Omega \cup \{tmp\}$
        $\mathbf{E} := [\mathbf{E}\ \ \psi_{tmp}]$
    end for
    $\Lambda_t := \Lambda_{t-1} \cup \Omega$
    $\mathbf{\Phi}_t := [\mathbf{\Phi}_{t-1}\ \ \mathbf{E}]$
    $\mathbf{W}_t :=$arg $\min_W \|\mathbf{X} - \mathbf{\Phi}_t \mathbf{W}\|_2^2$
    $\mathbf{R}_t := \mathbf{X} - \mathbf{\Phi}_t \mathbf{W}_t$
end for
Output: $\tilde{\mathbf{Y}}$ (composed of rows of $\mathbf{W}_t$ at indices Λ_t)

carriers, the block MMSE sparse-SQRD equalizer requires a high computational cost. For this reason, a submatrix equalization scheme is presented to reduce the computational cost required in the equalization.

The proposed submatrix equalization scheme, which is composed of eight MMSE sparse-SQRD equalizers, is presented in Fig. 4.13. The submatrix builder block divides the channel matrix $\mathbf{H}$ into eight smaller submatrices $(\mathbf{Q}_1, \ldots, \mathbf{Q}_8)$. It also divides the vector of received symbols $\mathbf{u}$ into eight smaller subvectors $(\mathbf{y}_1, \ldots, \mathbf{y}_8)$. Then, the k-th equalizer is fed with a subvector $\mathbf{y}_k$ of received symbols and the channel submatrix $\mathbf{Q}_k$. The output of the k-th equalizer is fed to the input of the $(k+1)$-th equalizer. This feedback is one of the strategies that are used to minimize the degradation in the BER caused by this proposed scheme. Another strategy to reduce the degradation is an overlapping between

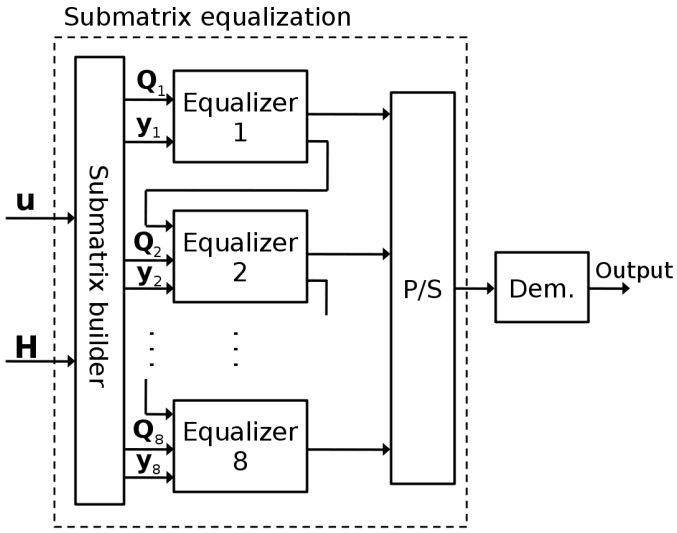

Figure 4.13: Submatrix equalization scheme for the ISDB-T receiver with 4-element ESPAR.

the subvectors and submatrices.

Figure 4.14 presents an example of how the submatrices and subvectors are obtained. In this figure, for illustration purposes it is assumed that the channel matrix is divided into three submatrices and subvectors, but the same procedure is applied for dividing the channel matrix into eight submatrices. The channel matrix $\mathbf{H}$ is composed of only the seven strongest frequency components of the antenna weights; thus, limiting the number of non-zero diagonals in $\mathbf{H}$ to seven. The channel matrix $\mathbf{H}$ is divided into the submatrices $\mathbf{Q}_1$ (yellow), $\mathbf{Q}_2$ (brown), and $\mathbf{Q}_3$ (green). Similarly, the vector of received symbols $\mathbf{u}$ is divided into $\mathbf{y}_1$, $\mathbf{y}_2$, and $\mathbf{y}_3$. The zones in blue represent overlapping areas in the submatrices and subvectors. For example, the overlapping area between $\mathbf{Q}_1$ and $\mathbf{Q}_2$ means that both submatrices have the same elements in that area. The same overlapping is present in the subvectors. It is important to note that the overlapping covers an area of 60×60 elements in the submatrices and 60×1 in the subvectors. The reason of this big overlapping is the separation of 12 positions between the non-zero diagonals of $\mathbf{H}$. To avoid a big degradation in the BER, at least five diagonals have to be overlapped resulting in the 60×60 section.

In the k-th equalizer (for $K<8$), the output symbols corresponding to the lower

overlapping zone are discarded due to its higher probability of having an error. This is not a problem because the overlapped zones guarantee that these symbols are recovered in the next equalizer. The elements in the upper overlapped section of the subvector $\mathbf{y}_k$ are compensated using the output symbols of the $(k-1)$-th equalizer (for k>1). This feedback is required to compensate that a part of the diagonals elements are not included in the submatrices. Although these strategies increase the computational cost of the equalization, they offer a good trade-off between computational cost and small degradation in the BER.

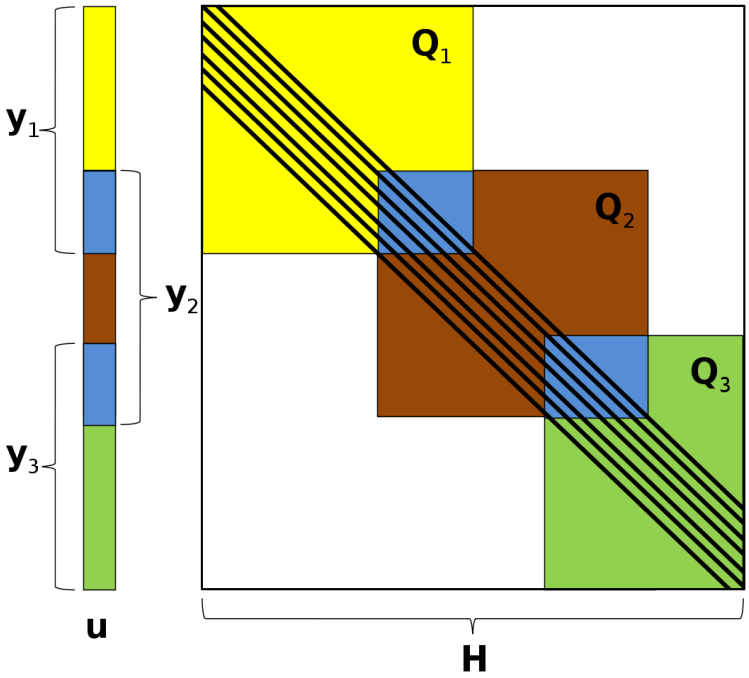

Figure 4.14: Example of dividing **H** into three submatrices.

4.3.5 Simulation Results

Impedance Matrix and Antenna Weights

To obtain the impedance matrix of the 4-elements ESPAR antenna, the 4NEC2 [69] simulator was used. The antenna is composed of four monopoles of length ($L_m = 0.24\lambda$) over a perfect ground plane. The frequency of 500 MHz is also considered. The self-impedance Z_{00}, Z_{11}, Z_{22}, and Z_{33} are obtained by simulating

each antenna element separately. To obtain the mutual-impedance elements of the impedance matrix, we have to solve the system given by

$$\begin{aligned} V_0 &= I_0 Z_{00} + I_1 Z_{01} + I_2 Z_{02} + I_3 Z_{03} \\ 0 &= I_0 Z_{10} + I_1 Z_{11} + I_2 Z_{12} + I_3 Z_{13} \\ 0 &= I_0 Z_{20} + I_1 Z_{21} + I_2 Z_{22} + I_3 Z_{23} \\ 0 &= I_0 Z_{30} + I_1 Z_{31} + I_2 Z_{32} + I_3 Z_{23} \end{aligned} \tag{4.44}$$

where V_0 is the voltage in the terminals of the radiator element (#0) and I_k is the current in the #k-th antenna element. The values of V_0, I_0, I_1, I_2, and I_3 are also obtained from the simulation. The rest of the parameters can be calculated replacing the equivalences shown in Eq. (4.25) into Eq. (4.44). Finally, the resulting impedance matrix is

$$\mathbf{Z} = \begin{bmatrix} 39.3 + j10.3 & 35.85 + j1.29 & 35.85 + j1.29 & 35.85 + j1.29 \\ 35.85 + j1.29 & 39.3 + j10.3 & 36.02 + j2.52 & 36.02 + j2.52 \\ 35.85 + j1.29 & 36.02 + j2.52 & 39.3 + j10.3 & 29.88 - j7.59 \\ 35.85 + j1.29 & 36.02 + j2.52 & 29.88 - j7.59 & 39.3 + j10.3 \end{bmatrix}. \tag{4.45}$$

After finding the impedance matrix, an exhaustive search approach was used to select the rest of the antenna parameters. The objective was to find the parameters that can provide a good frequency response of the antenna weights. It is required that the antenna weights $(\mathbf{w}_1, \mathbf{w}_2, \mathbf{w}_3)$ have small DC component and high frequency shifted components, but at the same time minimizing the harmonics. The search approach considered the best trade-off of the discussed requirements and the resulting parameters are presented in Table 4.4.

Figure 4.15 presents the frequency spectrum of the antenna weights $\mathbf{w}_k$ that were described in Eq. (4.29). This figure shows the magnitude of the frequency spectrum using the FFT operation with a FFT window size of $N = 256$. For fair comparison, the antenna weights $\mathbf{w}_k$ were normalized and limited to a maximum power of 1. The result in this figure is similar to the frequency spectrum of the antenna wights using the 3-element ESPAR antenna. The antenna weight $\mathbf{w}_0$ has a strong DC component with very small fundamental and harmonic components. The other antenna weights $(\mathbf{w}_1, \mathbf{w}_2, \mathbf{w}_3)$ have fundamental components at +12 and -12, but they have a higher magnitude compared with the 3-element ESPAR

Table 4.4: Parameters of the 4-element ESPAR antenna

Frequency	500MHz
Wavelength (λ)	0.6m
Z_0	75Ω
Monopole length (L_m)	0.24λ=14.4cm
d	0.1λ=6cm
d_1	0.092λ=5.54cm
x_1	3Ω
x_2	11Ω
x_3	14Ω

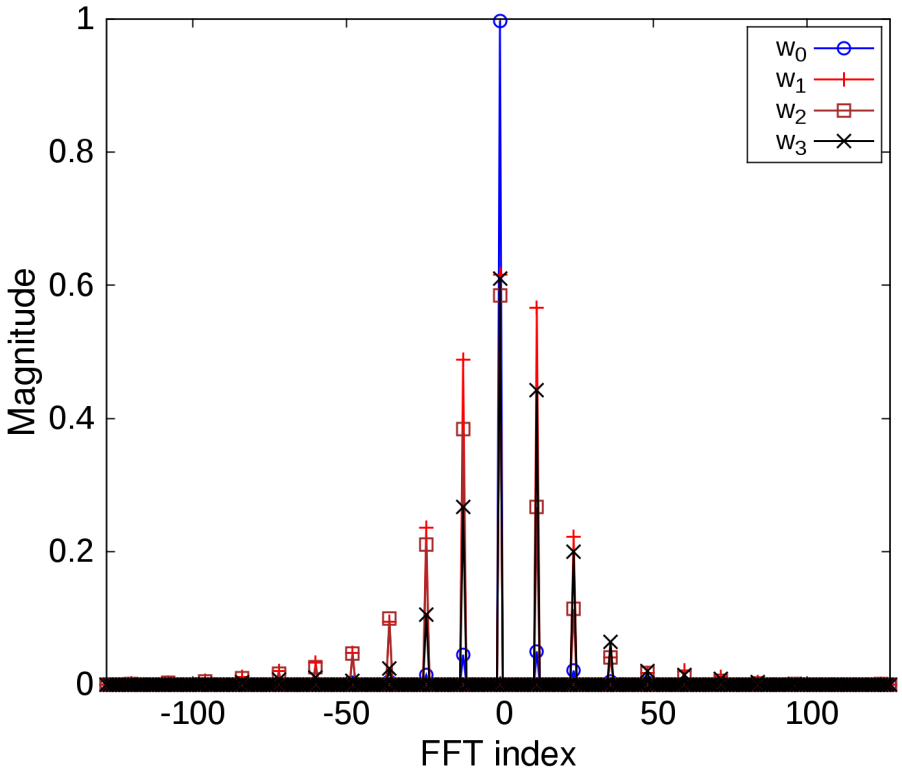

Figure 4.15: Frequency spectrum of $\mathbf{w}$ using the real model of the 4-element ESPAR antenna with $N = 256$.

antenna. It can be observed that in this case there are also harmonic components with decreasing value.

BER and NMSE

To determine the performance of the ISDB-T receiver with 4-element ESPAR antenna, a simulation model was implemented in c++ using the it++ [64] communications library. The simulation implemented the transmitter and receiver depicted in figures 4.3 and 4.9, respectively. The model can simulate the ISDB-T mode 1 and 2 that have FFT window size ($N = 2048$) and ($N = 4096$), respectively. The TU6 [70] channel model and Doubly-selective fading are used. For channel estimation, the proposed CS-based scheme is used with the 4C-OMP and 4C-SOMP recovery algorithms. A summary of the simulation parameters is presented in Table 4.5.

Table 4.5: Simulation settings of the ISDB-T reciver with 4-element ESPAR antenna

Parameter	Mode 1	Mode 2
Data subcarriers	1254	2508
Pilot subcarriers	114	228
FFT window size	2048	4096
Modulation	QPSK	
Pilot type	Comb-type	
GI	1/8	
Noise type	AWGN	
Channel model	TU6	
Fading	Doubly selective	
Doppler shift	Jakes model	
Channel estimation	CS with 4C-OMP and 4C-SOMP	
L	170	341
Equalization	Block and submatrix scheme	

The Jakes model [73, 74] is utilized for the Doppler shift. The normalized maximum Doppler shift is given by

$$f_d T_s = \frac{f_d}{f_s}, \tag{4.46}$$

where f_d is the maximum Doppler shift frequency and f_s is the OFDM subcarrier frequency spacing. Then, the relative speed in (m/s) between the transmitter and receiver is given by

$$v = f_d \frac{3 \times 10^8}{f}, \tag{4.47}$$

where f is the frequency of the signal. Considering mode 1 (f_s=4kHz) and a frequency band of 500 MHz, a normalized maximum Doppler shift of 0.025 is equal to a speed of 216 km/h.

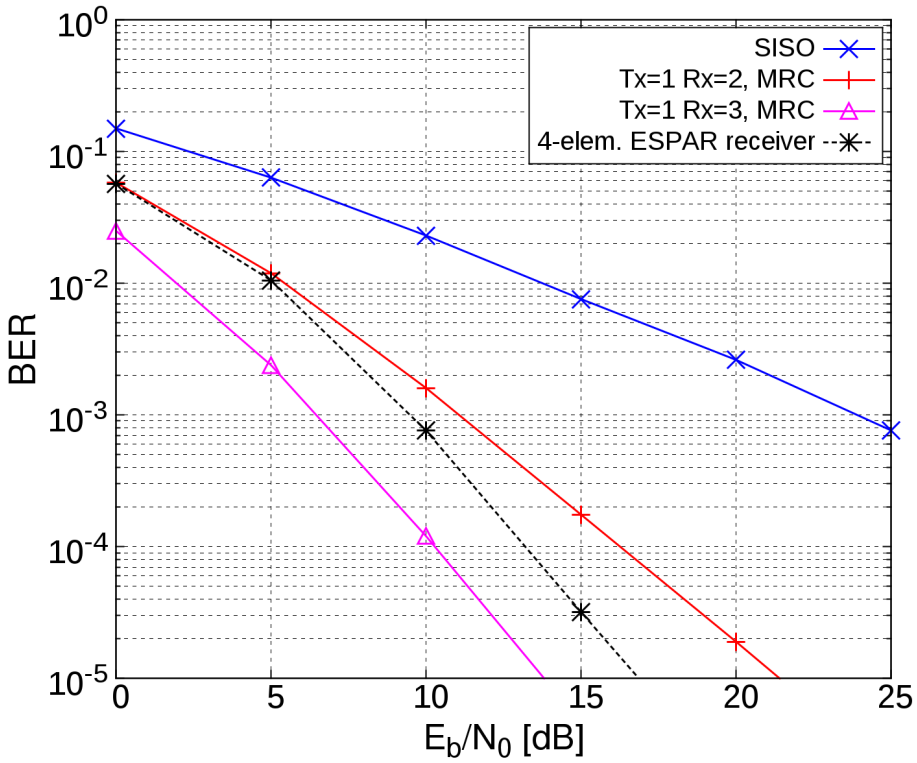

Figure 4.16: BER comparison of the proposed ISDB-T receiver versus conventional receivers without ESPAR antenna. Perfect CSI and without Doppler shift.

Figure 4.16 presents the BER performance of the proposed receiver considering perfect CSI and without Doppler shift. For comparison, it includes the BER of other conventional systems: SISO, an antenna diversity scheme with one transmitter and two receivers (Tx=1, Rx=2) using MRC, and another antenna diversity scheme with (Tx=1, Rx=3) using MRC. This figure shows that the proposed receiver obtains a BER performance that is better than a conventional diversity scheme with two receivers. The proposed receiver, which requires only one RF chain, is able to achieve diversity gain of around 15 dB compared to the SISO system for a BER of 10^{-3}.

Figure 4.17 presents the average recovery percentage of the delay positions of the estimated CIR for the CS-based channel estimation. It presents the recovery percentage of the 4C-OMP and 4C-SOMP algorithms using the TU6 channel, which has six paths. In the case of 4C-OMP, the recovery accuracy is higher using mode 2 because it has more pilot subcarriers compared with mode 1. Compared to 4C-OMP, the 4C-SOMP algorithm obtained the best recovery accuracy that is close to 100% for all E_b/N_0.

Figure 4.18 presents the NMSE of the CS-based channel estimation for different normalized maximum Doppler shift and using mode 1. It shows the NMSE using the 4C-OMP and 4C-SOMP recovery algorithms. The 4C-SOMP algorithm offers the smallest error with and without Doppler shift. However, the NMSE has a error floor for E_b/N_0>20 dB. The error floor is result of the harmonic components of the frequency response of the antenna weights. The harmonic components cause a small interference in the pilot subcarriers from the data subcarriers and this is the cause of the error in the estimation. On the other hand, when E_b/N_0<15 dB, the CS-based channel estimation obtains a good result. The figures of the average recovery % and NMSE showed that the 4C-SOMP algorithm gives the best results so it is chosen to obtain the BER performance of the proposed receiver.

The BER performance of the proposed receiver using CS-based channel estimation with 4C-SOMP is presented in Fig. 4.19. It shows the BER with different normalized maximum Doppler shift using mode 1 and 2. For comparison, the BER of the proposed system with perfect CSI is also included. In the case when the normalized maximum Doppler shift is zero ($F_dT_s = 0$) and E_b/N_0<10 dB, the

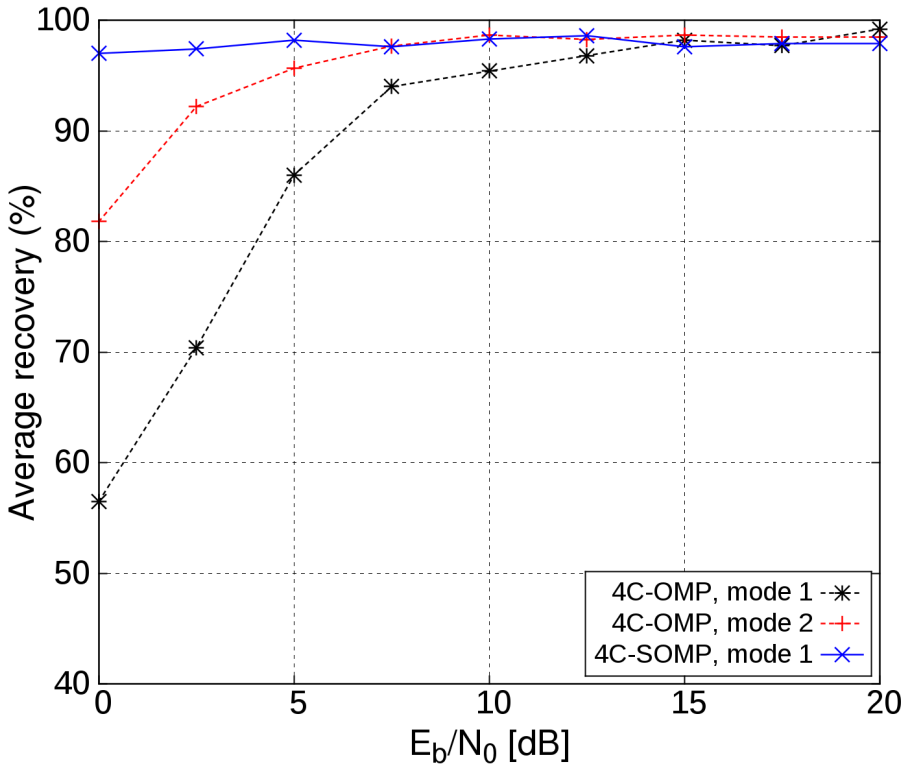

Figure 4.17: Average recovery percentage of the CS-based channel estimation using 4C-OMP (dashed line) and 4C-SOMP (solid line).

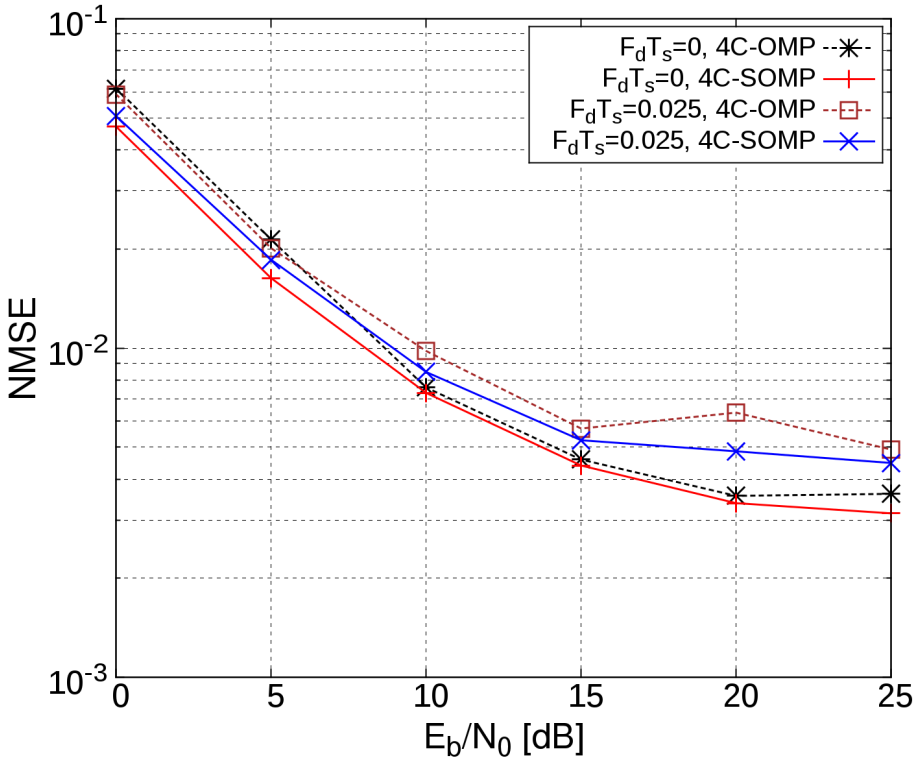

Figure 4.18: NMSE of the CS-based channel estimation using 4C-OMP (dashed line) and 4C-SOMP (solid line). Mode 1 (N = 2048) and different normalized maximum Doppler shift.

BER using CS-based channel estimation has a small degradation compared with the perfect CSI case. When E_b/N_0>10 dB, the estimation accuracy is reduced and there is also a error floor due to the limitation of the number of diagonals of **H**. The BER in the mode 2 is better than mode 1 due to the increased number of pilot subcarriers in mode 2. When there is Doppler shift due to the movement of the receiver, the BER is degraded due to the lost of orthogonality between the subcarriers. In the case when the normalized maximum Doppler shift is 0.025 ($F_dT_s = 0.025$), the BER has a error floor for E_b/N_0>20 dB. The same happens when ($F_dT_s = 0.05$), but with a slightly higher error floor.

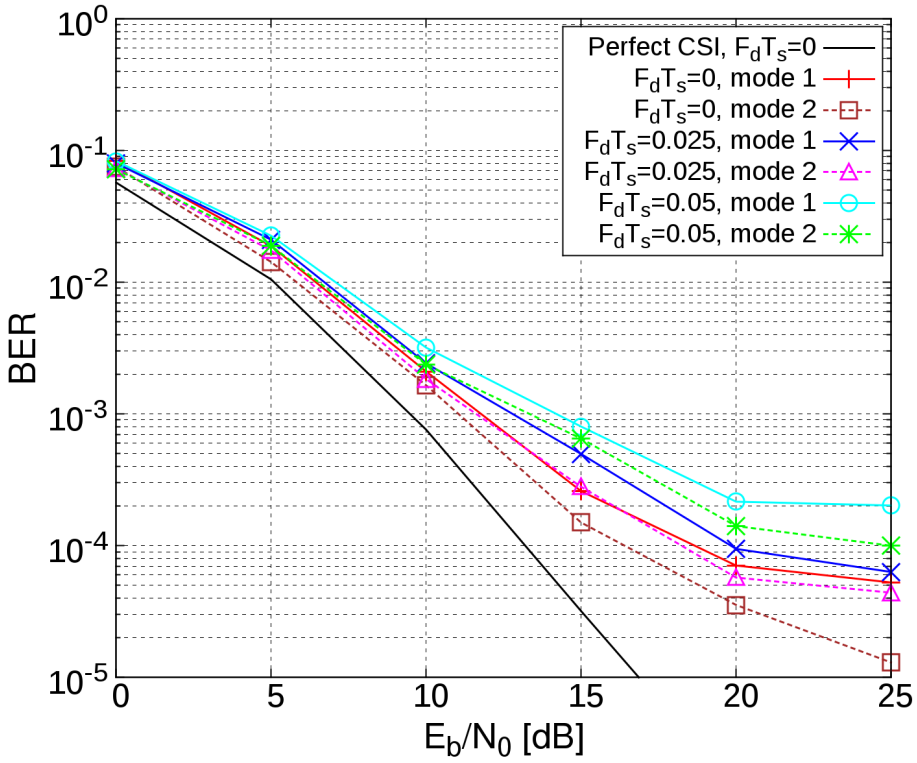

Figure 4.19: BER of mode 1 (N = 2048) and mode 2 (N = 4096) for different normalized maximum Doppler shift. Submatrix equalization and CS channel estimation with 4C-SOMP.

Submatrix Equalization Performance

The BER performance and average computational cost of the submatrix equalization are compared with the block equalization. Figure 4.20 presents a comparison of the BER performance between the block equalization (dashed line) and submatrix equalization (solid line) for mode 1 and different normalized maximum Doppler shift. This figure shows that the submatrix equalization degrades the BER performance. In the case when the normalized maximum Doppler shift is zero ($F_dT_s = 0$), the degradation is small for E_b/N_0<15 dB. When (F_dT_s>0), the BER of both equalization schemes is very similar. Therefore, the submatrix equalization is a good alternative because it introduces only a small degradation in the BER.

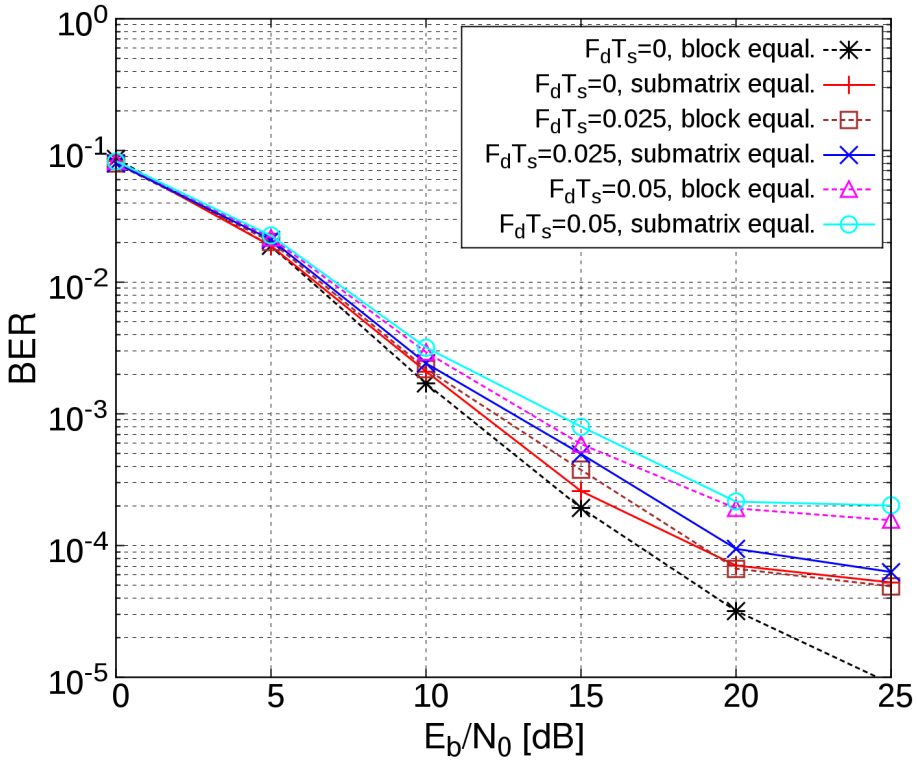

Figure 4.20: BER comparison of block and submatrix equalization for different normalized Doppler shift. Mode 1 (N = 2048), CS channel estimation with 4C-SOMP.

The computational cost required in the equalization was obtained from the simulation and it is given as the number of average complex flop required. Table 4.6 and Fig. 4.21 present the average number of flop per subcarrier required in the equalization. For mode 1, the submatrix equalization scheme reduces the required computational cost by around 90% compared with block equalization. An even bigger reduction of 92% is obtained in mode 2. Consequently, the submatrix equalization scheme achieves an important reduction in the computational cost while the degradation in the BER is small. The proposed submatrix equalization scheme offers a good trade-off between reduced computational cost and small BER degradation.

Table 4.6: Average number of flop per subcarrier required for the equalization in the ISDB-T receiver with ESPAR antenna

Detection scheme	Mode 1	Mode 2
Block	38251	90430
Submatrix	3648	7509

4.4 Summary

This chapter presented ESPAR antenna-based ISDB-T receivers. In the first part of the chapter, an ISDB-T receiver using a 3-element ESPAR antenna with periodically alternating directivity was presented. The performance of this receiver was analyzed considering the ideal and real models of the ESPAR antenna. When the ideal model is considered, the receiver obtains a good diversity gain. However, the gain is significantly reduced when the real model is considered. For that reason, in the second part of the chapter, an ISDB-T receiver with 4-element ESPAR antenna with periodically alternating directivity was presented. This receiver considers the real model of the 4-element ESPAR antenna, which is a more realistic scenario. Considering perfect CSI, the proposed receiver can achieve diversity gain of about 15 dB for a BER of 10^{-3}. The proposed receiver, which requires only a single RF chain, obtains a BER better than the antenna diversity scheme with two receivers. For channel estimation, a CS-based scheme with two recovery algorithms was presented. The 4C-OMP and 4C-SOMP algorithms can recover the CIR of the four antenna elements with good accuracy; moreover, it has been shown that the 4C-SOMP algorithm achieves the best performance. The performance of the system was also analyzed when Doppler shift is present; thus, the receiver is moving. The BER and channel estimation accuracy is reduced when Doppler shift is present.

A submatrix equalization scheme was also presented to reduce the computational cost of the equalization. This scheme reduces the required computational cost by about 90% and 92% for mode 1 and mode 2, respectively.

As shown in this chapter, the receiver with 4-element ESPAR antenna obtained a better BER compared to the receiver with 3-element antenna. This

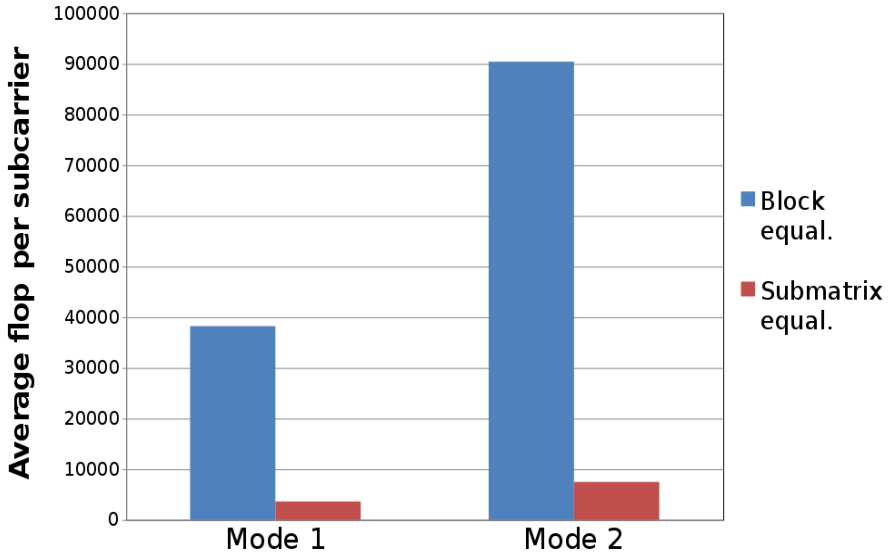

Figure 4.21: Comparison of the average flop per subcarrier required by block and submatrix equalization.

implies that increasing the number of elements in the ESPAR antenna would improve the BER. However, there are two main problems if we further increase the number of antenna elements. First, the physical structure of the antenna becomes more complicated and increases its cost. Second, the separation between the elements is decreased if there are more antenna elements. This smaller separation would increase the correlation between the elements and it would negatively impact in the performance of the receiver. Therefore, for designing the ESPAR antenna it is important to consider the trade-off between the complexity of the physical structure of the antenna, the separation between the antenna elements, and the BER performance that can be obtained.

Chapter 5

Conclusion

Nowadays, wireless communications have become a essential part of our lives. We connect everyday to Internet using the WLAN and cellular connection of our smartphones. People watch TV at home and even in their cars. Moreover, these technologies are using techniques based in OFDM modulation, thus the importance of new developments to increase its efficiency. This dissertation focuses in the design of diversity receivers to overcome the multipath fading that can severely affect the BER of a wireless link. Although antenna diversity is commonly used to achieve diversity and improve the BER, it has several limitations due to the additional RF chains that requires. The receivers presented in this dissertation use ESPAR antenna to improve the BER without requiring additional RF chains.

The first main contribution of this dissertation was presented in Chapter 3, where channel estimation and detection schemes for a MIMO-OFDM receiver with 3-element ESPAR antenna with periodic alternating directivity were proposed. The simulation results showed that considering perfect CSI and compared to the conventional 2×2 MIMO-OFDM system, the receiver can obtain a diversity gain of about 14 dB for a BER of 10^{-3}. This represents an important improvement in the BER performance and it is obtained without additional RF chains. For channel estimation, MMSE and CS-based estimators were presented. The CS-based channel estimation with modified-OMP obtained the best BER performance and required less computational complexity than the MMSE channel estimation. A submatrix detection scheme was proposed to reduce the

computational cost required by the detection. This detection scheme reduces the computational cost by about 92% compared to the block detection approach. However, the submatrix detection scheme causes a small degradation in the BER. For 16-QAM modulation, the degradation is about 1 dB for a BER of 10^{-3} and 3 dB for a BER of 10^{-4}.

The other main contribution was presented in Chapter 4, which included the design of two ESPAR antenna-based ISDB-T receivers. First, an ISDB-T receiver with 3-element ESPAR antenna was proposed. The performance of this receiver was analyzed considering the ideal and real models of the ESPAR antenna. In the real model, the frequency spectrum of the antenna weights depends on the physical structure of the ESPAR antenna and it can reduce the performance improvement. When the ideal model is considered, the receiver obtains a diversity gain of about 13 dB for a BER of 10^{-3}. However, this improvement is significantly reduced in about 6 dB when the real model is considered. For that reason, in the second part of the chapter, an ISDB-T receiver with 4-element ESPAR antenna with periodically alternating directivity was presented. This receiver considered the real model of the 4-element ESPAR antenna because it is a more realistic scenario. Considering perfect CSI, this receiver can achieve diversity gain of about 15 dB for a BER of 10^{-3}. For channel estimation, a CS-based estimator was designed considering the real model of the ESPAR antenna. The 4C-OMP and 4C-SOMP algorithms were designed to recover the CIR with good accuracy and reducing the computational complexity. These algorithms can recover the CIR of the four antenna elements with good accuracy and it was shown that the 4C-SOMP algorithm achieves the best performance. This receiver is designed to operate in a vehicle so the evaluation of the effects of the Doppler shift is important. The results showed that the BER and channel estimation accuracy are reduced when Doppler shift is present; however, the BER is better than 10^{-3} even for a normalized maximum Doppler shift of 0.05. A submatrix equalization scheme was also presented to reduce the computational cost of the equalization. In mode 1, this scheme reduces the computational cost by about 90% compared to block equalization. Additionally, it was shown that the submatrix scheme introduces only a small degradation in the BER.

5.1 Future Work

The results obtained using the real model of the ESPAR antenna highlighted the importance of its physical design to obtain a better improvement in the BER. The 4-element ESPAR antenna is only one of the possible solutions; therefore, the first future work is related to the design of the physical structure of the ESPAR antenna. Previously, we considered that all antenna elements are the same in terms of length and shape. However, it is also possible to use antenna elements with different shape and other parameters to improve the frequency response of the antenna weights. Depending on the required BER, it is also possible to design an ESPAR antenna with more than 4 elements; although, the increase in the antenna's cost and the impact in the final performance has to be considered.

Another important future work is to build the ESPAR antenna with periodically alternating directivity for experimentally determine the correlation of the channel response of the antenna elements. We assumed that a separation of around 0.09λ between the antenna elements is enough to have uncorrelated channel response between the elements. The experiments would show if this separation is enough or it has to be increased. This is important because it directly affects the maximum improvement that can be obtained in the BER.

Finally, the other required future work is a hardware implementation of the ISDB-T receiver with ESPAR antenna. The receiver has to be designed and implemented in a field-programmable gate array (FPGA) in order to experimentally obtain different parameters such as the BER, power consumption, and hardware size.

Acknowledgements

First of all I thank God for the life and strength that allowed me to achieve another of my dreams.

I would like to thank my supervisor Professor Minoru Okada for his valuable guidance, comments, and support for my research, Doctoral course, and this dissertation.

I would like to thank Associate Professor Takeshi Higashino and Assistant Professor Yafei Hou for the guidance, support, and comments they gave me and helped to improve my research.

I also thank my Thesis co-supervisor Professor Kenji Sugimoto for his comments and discussion to improve this dissertation.

My gratitude to The Ministry of Education, Culture, Sports, Science & Technology in Japan (MEXT) which granted me this scholarship and financially supported me to finish my Doctoral Course.

To my parents who have supported and helped me my whole life. Our weekly skype chat and messages gave me strength in the difficult times and always reminded me of their love. Thanks to my brothers and whole family that constantly supported me with messages and good wishes. Thank you all for giving me every day the strength and encourage to continue, without you this would not have been possible.

To the International students in NAIST who have shared their friendship and time with me. To my friends the Latin Naisters who made me feel like I was home regardless of our nationalities. Thank you for all the great moments we shared together. I would like to specially thank Gustavo and Nayra for their invaluable friendship and support. You became my second family here in Japan and I am forever thankful. I am sure our friendship will continue and hopefully we will

meet again in some place of Latin America or the world.

My acknowledgement to the present and past members of the Network Systems Laboratory for their help and enjoyable time that we spent together.

Thanks to you for being my companion during a great part of my Doctoral course. Thank you for your love, support, encouragement, and help proofreading my papers and journals. I learned a lot from you and I am forever thankful.

And finally, my deepest gratitude to all the people who have supported me in every step of my life.

Publications

Journal Articles

1. Diego Javier Reinoso Chisaguano and Minoru Okada, "Low Complexity Submatrix Divided MMSE Sparse-SQRD Detection for MIMO-OFDM with ESPAR Antenna Receiver," *VLSI Design*, vol. 2013, Article ID 206909, 11 pages, 2013. [Corresponds to Chapters 3 and 4]

2. Diego Javier Reinoso Chisaguano, Yafei Hou, Takeshi Higashino, and Minoru Okada, "ISDB-T Diversity Receiver using a 4-element ESPAR Antenna with Periodically Alternating Directivity," *ITE Transactions on Media Technology and Applications*, Vol. 3, No. 4, pp. 268-278, October 2015. [Corresponds to Chapter 4]

3. Diego Javier Reinoso Chisaguano, Yafei Hou, Takeshi Higashino, and Minoru Okada, "Low-Complexity Channel Estimation and Detection for MIMO-OFDM Receiver With ESPAR Antenna," *IEEE Transactions on Vehicular Technology*, doi: 10.1109/TVT.2015.2506782 (To appear). [Corresponds to Chapter 3]

International Conferences (Peer Review)

1. Diego Javier Reinoso Chisaguano and Minoru Okada, "MIMO-OFDM Receiver using a Modified ESPAR Antenna with Periodically Changed Directivity," in *Proc. of the 13th International Symposium on Communications and Information Technologies (ISCIT 2013)*, pp. 154-159, September 2013. [Corresponds to Chapter 3]

2. Diego Javier Reinoso Chisaguano, Takeshi Higashino, and Minoru Okada, "ISDB-T Receiver with Single-RF Diversity using a 3-element ESPAR Antenna," in *Proc. of the 14th International Symposium on Communications and Information Technologies (ISCIT 2014)*, pp. 462-465, September 2014. [Corresponds to Chapter 4]

Domestic Conference (Non Peer Review)

1. Diego Javier Reinoso Chisaguano, Takeshi Higashino, and Minoru Okada, "Compressed Sensing based channel estimation for MIMO-OFDM with ESPAR antenna," in *IEICE Technical Report, Smart Info-Media System Technical Meeting*, vol. 113, No. 343, pp. 99-104, Tottori, Japan, December 2013. [Corresponds to Chapter 3]

References

[1] International Telecommunication Union, "ICT Facts & Figures 2015", May 2015.

[2] International Telecommunication Union, "Measuring the Information Society 2013", Geneva, 2013.

[3] European Broadcasting Union, "Digital Video Broadcasting (DVB) framing structure, channel coding and modulation for digital terrestrial television", ETSI EN 300 744 V1.6.1, 2009.

[4] Advanced Television Systems Committee Inc., "A/53: ATSC Digital Television Standard, Parts 1 - 6, 2007", 2007.

[5] Association of Radio Industries and Businesses, "Transmission System for Digital Terrestrial Television Broadcasting", ARIB STD-B31 version 1.6-E2, 2005.

[6] Framing Structure, Channel Coding and Modulation for Digital Television Terrestrial Broadcasting System, Chinese National Standard GB 20600-2006.

[7] IEEE Computer Society, Part 11: Wireless LAN Medium Access Control (MAC) and Physical Layer (PHY) Specifications; High-speed Physical Layer in the 5 GHz Band, IEEE Std 802.11a-1999(R2003), 2003.

[8] IEEE Computer Society, Part 11: Wireless LAN Medium Access Control (MAC) and Physical Layer (PHY) Specifications; Further Higher Data Rate Extension in the 2.4 GHz Band, IEEE Std 802.11g-2003.

[9] IEEE Computer Society, Part 11: Wireless LAN Medium Access Control (MAC) and Physical Layer (PHY) Specifications; Amendment 5: Enhancements for Higher Throughput, IEEE Std 802.11n-2009, New York, October 2009.

[10] IEEE Computer Society, Part 11: Wireless LAN Medium Access Control (MAC) and Physical Layer (PHY) Specifications; Amendment 4: Enhancements for Very High Throughput for Operation in Bands below 6 GHz, IEEE Std 802.11ac-2013, New York, Dec. 2013.

[11] Long Term Evolution (LTE) physical layer, General description. 3GPP TS 36.201 version 8.1.0 Release 8.

[12] S. Tsukamoto and M. Okada, "Single-RF diversity for OFDM system using ESPAR antenna with periodically changing directivity", in *Proc. of Second International Symposium on Radio Systems and Space Plasma*, pp. 1-4, Bulgaria, Aug. 2010.

[13] I.G.P. Astawa and M. Okada, "An RF signal processing based diversity scheme for MIMO-OFDM Systems," *IEICE Transactions on Communications*, Vol. E95-A, No. 2, pp. 515-524, Feb. 2012.

[14] https://en.wikipedia.org/wiki/List_of_digital_television_deployments_by_country

[15] Samuel C. Yang, "OFDMA system analysis and design", Artech House, 2010.

[16] D. Gesbert, M. Shafi, D. Shiu, P.J. Smith, and A. Naguib, "From theory to practice: an overview of MIMO space-time coded wireless systems," *IEEE Journal on Selected Areas in Communications*, vol. 21, no. 3, pp. 281-302, Apr. 2003.

[17] H. Bolcskei, "MIMO-OFDM wireless systems: basics, perspectives, and challenges," *IEEE Wireless Communications*, vol. 13, no. 4, pp. 31-37, Aug. 2006.

[18] E. Telatar, "Capacity of multi-antenna Gaussian channels," *European Transactions on Telecommunications*, vol. 10, pp. 585-595, 1999.

[19] A. Goldsmith, "Wireless Communications", Cambridge University Press, 2005.

[20] Y. Li, L.J. Cimini, and N.R. Sollenberger: "Robust channel estimation for OFDM systems with rapid dispersive fading channels", *IEEE Transactions on Communications*, vol. 46, no. 7, pp. 902-915, July 1998.

[21] G.L. Stuber, J.R. Barry, S.W. McLaughlin, Ye Li, M.A. Ingram, and T.G. Pratt, "Broadband MIMO-OFDM wireless communications," in *Proceedings of the IEEE*, vol. 92, no. 2, pp. 271-294, Feb 2004.

[22] A. van Zelst, R. van Nee, and G.A. Awater, "Space division multiplexing (SDM) for OFDM systems," in *Proceedings of IEEE Vehicular Technology Conference*, vol. 2, pp. 1070-1074, May 2000.

[23] A. van Zelst and T.C.W Schenk, "Implementation of a MIMO OFDM-based wireless LAN system," *IEEE Transactions on Signal Processing*, vol. 52, no. 2, pp. 483-494, Feb. 2004.

[24] C.B. Dietrich, K. Dietze, J.R. Nealy, and W.L. Stutzman, "Spatial, polarization, and pattern diversity for wireless handheld terminals," *IEEE Transactions on Antennas and Propagation*, vol. 49, no. 9, pp. 1271-1281, Sep. 2001.

[25] T. Ohira and K. Iigusa, "Electronically steerable parasitic array radiator antenna," *Electronics and Communications in Japan (Part II:Electronics)*, vol. 87, no. 10, pp. 25-45, Oct. 2004.

[26] Ohira, T. and K. Gyoda, "Electronically steerable passive array radiator antennas for low-cost analog adaptive beamforming," in *Proceedings of Phased Array Systems and Technology*, Dana Point, CA, USA, May 2000.

[27] C. Sun, A. Hirata, T. Ohira and N.C. Karmakar, "Fast beamforming of electronically steerable parasitic array radiator antennas: theory and experiment," *IEEE Transactions on Antennas and Propagation*, vol. 52, no. 7, pp. 1819-1832, July 2004.

[28] T. Sawaya, K. Iigusa, M. Taromaru, and T. Ohira, "Reactance diversity: proof-of-concept experiments in an indoor multipath-fading environment with a 5-GHz prototype planar ESPAR antenna", in *Proc. of Consumer Communications and Networking Conference*, pp. 678-680, Jan. 2004.

[29] M. Yamamoto, M. Taromaru, H. Sadamichi, and A. Shimizu, "Performance of angle switch diversity using ESPAR antenna for mobile reception of terrestrial digital TV", in *Proc. of IEEE Conference on Vehicular Technology VTC-Spring*, pp. 1-5, 2006.

[30] A. Kalis, A.G. Kanatas, and C.B. Papadias, "A novel approach to MIMO transmission using a single RF front end", *IEEE Journal on Selected Areas in Communications*, vol. 26, no. 6, pp. 972-980, Aug. 2008.

[31] O.N. Alrabadi, C.B. Papadias, A. Kalis, N. Marchetti, and R. Prasad, "MIMO transmission and reception techniques using three-element ESPAR antennas," *IEEE Communications Letters*, vol. 13, no. 4, pp. 236-238, April 2009.

[32] NEC: http://www.nec2.org/

[33] G.J. Foschini, G. D. Golden, R. A. Valenzuela, and P.W. Wolniansky, "Simplified processing for high spectral efficiency wireless communication employing multi-element arrays," *IEEE Journal on Selected Areas in Communications*, vol. 17, no. 11, pp. 1841-1851, Nov. 1999.

[34] P .W. Wolniansky, G. J. Foschini, G. D. Golden, and R. A. Valenzuela, "V-BLAST: An architecture for realizing very high data rates over the rich-scattering wireless channel," in *Proc. of IEEE ISSSE-98*.

[35] E.J. Candes and M.B. Wakin, "An introduction to compressive sampling," *IEEE Signal Processing Magazine*, vol. 25, no. 2, pp. 21-30, March 2008.

[36] D.L. Donoho, "Compressed sensing," *IEEE Transactions on Information Theory*, vol. 52, no. 4, pp. 1289-1306, April 2006.

[37] C.R Berger, Z. Wang, J. Huang, and S. Zhou, "Application of compressive sensing to sparse channel estimation," *IEEE Communications Magazine*, vol. 48, no. 11, pp. 164-174, Nov. 2010.

[38] E. J. Candes, "The restricted isometry property and its implications for compressed sensing," in *C. R. Acad. Sci.*, Ser. I, Paris, 2008, vol. 346, pp. 589-592.

[39] E.J. Candes and T. Tao, "Decoding by linear programming," *IEEE Transactions on Information Theory*, vol. 51, no. 12, pp. 4203-4215, Dec. 2005.

[40] W.U. Bajwa, J. Haupt, A.M. Sayeed, and R. Nowak, "Compressed channel sensing: a new approach to estimating sparse multipath channels," *Proceedings of the IEEE* , vol. 98, no. 6, pp. 1058-1076, June 2010.

[41] R. Baraniuk, M. Davenport, R. DeVore, and M. Wakin, "A simple proof of the restricted isometry property for random matrices," *Constructive Approximation*, vol. 28, no. 3, pp. 253-263, 2008.

[42] E.J. Candes, J. Romberg, and T. Tao, "Robust uncertainty principles: exact signal reconstruction from highly incomplete frequency information," *IEEE Transactions on Information Theory*, vol. 52, no. 2, pp. 489-509, Feb. 2006.

[43] J. Haupt, L. Applebaum, and R. Nowak, "On the Restricted Isometry of deterministically subsampled Fourier matrices," in *Proc. of 2010 44th Annual Conference on Information Sciences and Systems (CISS)*, pp. 1-6, March 2010.

[44] E. Candes and T. Tao, "The Dantzig selector: statistical estimation when p is much larger than n," *The Annals of Statistics (2007)*, pp. 2313-2351.

[45] J.A. Tropp and A.C. Gilbert, "Signal recovery from random measurements via orthogonal matching pursuit," *IEEE Transactions on Information Theory*, vol. 53, no. 12, pp. 4655-4666, December 2007.

[46] D. Needell, R. Vershynin, "Signal recovery from incomplete and inaccurate measurements via regularized orthogonal matching pursuit," *IEEE Journal of Selected Topics in Signal Processing*, vol. 4, no. 2, pp. 310-316, April 2010.

[47] D. Needell and J.A Tropp, "Cosamp: iterative signal recovery from incomplete and inaccurate samples," *Communications of the ACM*, vol. 53, No. 12, pp. 93-100, Dec. 2010.

[48] Wei Dai and O. Milenkovic, "Subspace pursuit for compressive sensing signal reconstruction," *IEEE Transactions on Information Theory*, vol. 55, no. 5, pp. 2230-2249, May 2009.

[49] K. Hayashi, M. Nagahara, and T. Tanaka, "A user's guide to compressed sensing for communications systems," *IEICE Transactions on Communications*, vol. E96-B, No. 3, pp. 685-712, 2013.

[50] M.A. Davenport, M.B. Wakin, "Analysis of orthogonal matching pursuit using the restricted isometry property," *IEEE Transactions on Information Theory*, vol. 56, no. 9, pp. 4395-4401, Sept. 2010.

[51] S. Foucart and H. Rauhut, "A Mathematical introduction to compressive sensing", Applied and Numerical Harmonic Analysis, Springer, 2013.

[52] M.F. Duarte, and Y.C. Eldar, "Structured compressed sensing: from theory to applications," *IEEE Transactions on Signal Processing*, vol. 59, no. 9, pp. 4053-4085, Sept. 2011.

[53] J. A. Tropp, A. C. Gilbert, and M. J. Strauss, "Algorithms for simultaneous sparse approximation part I: greedy pursuit", *Signal Processing*, vol. 86, no. 3, pp. 572-588, March 2006.

[54] W.U. Bajwa, A. Sayeed, and R. Nowak, "Compressed sensing of wireless channels in time, frequency, and space," in *Proc. of the 42nd Asilomar Conference on Signals, Systems and Computers*, pp. 2048-2052, Oct. 2008.

[55] Yuexing Peng, Xiao Yang, Xiaofeng Zhang, Wenbo Wang, and Bin Wu, "Compressed MIMO-OFDM channel estimation," in *Proc. of the 12th IEEE International Conference on Communication Technology (ICCT)*, pp. 1291-1294, Nov. 2010.

[56] Ch. QI and L. WU, "A hybrid compressed sensing algorithm for sparse channel estimation in MIMO-OFDM systems," in *Proc. of the 2011 IEEE International Conference on Acoustics, Speech and Signal Processing (ICASSP)*, pp. 3488-3491, 2011.

[57] Linglong Dai, Jintao Wang, Zhaocheng Wang, P. Tsiaflakis, and M. Moonen, "Spectrum- and energy-efficient OFDM based on simultaneous multi-channel reconstruction," *IEEE Transactions on Signal Processing*, vol. 61, no. 23, pp. 6047-6059, Dec. 2013.

[58] D. Wübben, R. Böhnke, V. Kühn, and K. D. Kammeyer, "MMSE extension of V-BLAST based on sorted QR decomposition", in *Proc. of the 2003 58th Vehicular Technology Conference*, 2003.

[59] Won Gi Jeon, Kyung Hi Chang, and Yong Soo Cho, "An equalization technique for orthogonal frequency-division multiplexing systems in time-variant multipath channels," *IEEE Transactions on Communications*, vol. 47, no. 1, pp. 27-32, Jan. 1999.

[60] Xiaodong Cai and G.B. Giannakis, "Bounding performance and suppressing intercarrier interference in wireless mobile OFDM," *IEEE Transactions on Communications*, vol. 51, no. 12, pp. 2047-2056, Dec. 2003.

[61] J. van de Beek, M. Sandell, and P. Börjesson, "ML estimation of time and frequency offset in OFDM systems," *IEEE Transactions on Signal Processing*, Vol. 45, No. 7, July 1997.

[62] J. van de Beek, M. Sandell, M. Isaksson, and P. Börjesson, "Low-complex frame synchronization in OFDM systems," in *Proc. of the Fourth IEEE International Conference on Universal Personal Communications*, pp. 982-986, Nov. 1995.

[63] M. Speth, F. Classen, H. Meyr, "Frame synchronization of OFDM systems in frequency selective fading channels," in *Proc. of the IEEE 47th Vehicular Technology Conference*, vol. 3, pp. 1807-1811, May 1997.

[64] IT++, http://itpp.sourceforge.net/devel/index.html

[65] 3rd Generation Partnership Project, Spatial channel model for Multiple Input Multiple Output (MIMO) simulations. 3GPP TR 25.996 V9.0.0, 2009.

[66] R. Niazadeh, M. Babaie-Zadeh, and C. Jutten, "On the achievability of Cramér-Rao Bound in noisy compressed sensing," *IEEE Transactions on Signal Processing* vol. 60, no. 1, pp. 518-526, Jan. 2012.

[67] Y. S. Cho, J. Kim, W. Y. Yang, and C. Kang, "MIMO-OFDM wireless communications with Matlab," Wiley, 2010.

[68] J.-J. van de Beek, O. Edfors, M. Sandell, S.K. Wilson, and P. Ola Borjesson, "On channel estimation in OFDM systems", in *Proc. of the 45th IEEE Conference - VTC*, vol. 2, pp. 815-819, July 1995.

[69] 4NEC2, http://www.qsl.net/4nec2/

[70] 3rd Generation Partnership Project; Technical Specification Group GSM/EDGE Radio Access Network. 3GPP TS 05.05 V8.20.0

[71] S. R. Saunders and A. Aragon-Zavala, "Antennas and propagation for wireless communication systems", Wiley, 2007.

[72] G. Tauböck and F. Hlawatsch, "A compressed sensing technique for OFDM channel estimation in mobile environments: Exploiting channel sparsity for reducing pilots," in *Proc. of 2008 IEEE International Conference on Acoustics, Speech and Signal Processing (ICASSP)*, pp. 2885-2888, 2008.

[73] W. C. Jakes, "Microwave Mobile Communications", Wiley, New York, 1974.

[74] R. H. Clarke, "A statistical theory of mobile-radio reception", *Bell Labs Tech. J.*, vol. 47, pp. 957-1000, Jul.-Aug. 1968.

Appendix

A. List of Abbreviations and Acronyms

3GPP	3rd Generation Partnership Project
ADC	analog to digital converter
ATSC	Advanced Television System Committee
AWGN	additive white Gaussian noise
BER	bit error rate
bps	bit per second
CFO	carrier frequency offset
CIR	channel impulse response
CoSaMP	compressive sampling matching pursuit
CP	cyclic prefix
CS	compressed sensing
CSD	cyclic shift delay
CSI	channel state information
DFE	decision-feedback equalizer
DPSK	differential phase-shift keying
DTMB	Digital Terrestrial Multimedia Broadcasting
DAC	digital to analog converter
DFT	discrete Fourier transform
DS	Dantzig selector
DTV	digital television
DVB-T	Digital Video Broadcasting-Terrestrial
ESPAR	electronically steerable passive array radiator

FEC	forward error correction
FFT	fast Fourier transform
flop	floating point operation
FPGA	field-programmable gate array
GI	guard interval
HDTV	high-definition TV
HPA	high power amplifier
HT-LTF	high throughput-long training field
ICI	intercarrier interference
IFFT	inverse fast Fourier transform
ISDB-T	Integrated Services Digital Broadcasting-Terrestrial
ISI	intersymbol interference
ITU	International Telecommunication Union
LCD	liquid crystal display
LS	least squares
MIMO-OFDM	multiple input multiple output - orthogonal frequency-division multiplexing
MMSE	minimum mean square error
MMSE sparse-SQRD	MMSE sparse-sorted QR decomposition
MRC	maximal ratio combining
MRI	magnetic resonance imaging
NEC	Numerical Electromagnetics Code
NMSE	normalized mean square error
OFDM	orthogonal frequency-division multiplexing
OMP	orthogonal matching pursuit
QAM	quadrature amplitude modulation
QPSK	quadrature phase-shift keying
RF	radio frequency
RIP	restricted isometry property
ROMP	regularized OMP
Rx	receiver
SDTV	standard-definition TV

SISO	single-input single-output
SOMP	simultaneous OMP
SP	subspace pursuit
TS	transport stream
TU6	Typical Urban 6-path
TV	television
Tx	transmitter
VBLAST	Vertical-Bell Laboratories Layered Space-Time
WLAN	Wireless Local Area Network